REPORT NO. 66

CENTRIFUGAL EFFECT ON THE BOUNDARY LAYER ON A BLADE OF AN AXIAL TURBO-MACHINE

ERIK K. A. OLSSON

April 1962

GAS TURBINE LABORATORY
MASSACHUSETTS INSTITUTE OF TECHNOLOGY
CAMBRIDGE · 39 · MASSACHUSETTS

CENTRIFUGAL EFFECT ON THE BOUNDARY LAYER ON A BLADE OF AN AXIAL TURBO-MACHINE

by

Erik K. A. Olsson

Under the Sponsorship of:

General Electric Company
Allison Division of General Motors Corporation
Westinghouse Electric Corporation

Gas Turbine Laboratory
Report Number 66

April 1962

Massachusetts Institute of Technology

ABSTRACT

A study of the effect of centrifugal force acting on the turbulent boundary layer of a blade in a turbo-machine is presented. The study includes experimental work conducted in an apparatus featuring an annular cascade of compressor blades, designed to simulate the flow in a compressor.

This is a case of three-dimensional turbulent boundary layer flow and the objects of the study were to find the magnitude of the cross-flow and gain a better understanding of the skewed boundary layers.

It is found that the cross-flow which develops in the boundary layer is small with velocities of the order of 1/10 of the through-flow velocities.

The study further resulted in the development of a model of skewed, turbulent velocity-profiles, involving two "universal" analytical functions and four parameters. This model has been used with success to describe the measured velocity-profiles.

The use of the model and the general result that the cross-flow is small has made it possible to find solutions to the boundary layer integral equations written in a "streamline" coordinate system. Application of the calculation method for the experimental data has been made successfully.

A loss parameter is defined and an extension to include the cross-flow losses is suggested.

ACKNOWLEDGEMENTS

The author wishes to express his appreciation to the entire staff of the M. I. T. Gas Turbine Laboratory for their interest and advice during the course of this work. I am especially grateful to my thesis-supervisor, Professor Edward S. Taylor for his inspiration and suggestions and to the other members of my thesis committee, Professors E. L. Möllö-Christensen and J. L. Kerrebrock for their valuable contributions.

I also wish to express my sincere gratitude to Mr. D. L. Baugh, Sr. and his staff for building the test apparatus; Mrs. M. Euvrard for doing the typing; and several students for helping with recording and processing of the data.

Professor Y. Senoo introduced me to the problem and arranged my contact with the Gas Turbine Laboratory. Financial aid given by the "Bengt Ingestrom Stiftelsen", Sweden, made possible my study at M. I. T.

Finally, I want to thank my wife for her understanding and encouragement, which was of greatest help during this work.

Centrifugal Effect on the Boundary Layer on a Blade of an Axial Turbo-Machine

TABLE OF CONTENTS

1. GENERAL CONSIDERATIONS

1.1 Introduction

The effect of centrifugal force acting on the boundary layer of a blade in a turbomachine has not received very much attention in the literature. Some work has been done theoretically, assuming the boundary layer to be laminar (Refs. 1-4), but there seems to be a complete lack of experimental data. As we expect the boundary layer to be turbulent over the main portion of the blades, it was decided that an experimental and theoretical investigation of the turbulent case should be performed in the Gas Turbine Laboratory, with the main goal of finding the magnitude of the cross-flow on the blades. The need for such an experiment was also emphasized by several investigations of losses in annular cascades, where large amounts of radial flow seemed to have occurred (Ref. 5-6).

The effect we are looking for is naturally most pronounced on a rotating blade and in the initial period of the project such an experiment was discussed. As we, however, could expect great difficulty in making boundary layer traverses on a rotating blade we decided to make the measurements in a stationary annular cascade with a centrifugal pressure gradient along the radial direction, while the rotating case would be attacked theoretically. As the mechanism of the cross-flow is basically that of a pressure gradient acting perpendicular to the streamlines, it is expected that if the equations of motion give a satisfactory solution of the non-rotating case, they will also be satisfactory for the rotating case.

1.2 Restrictions on the Problem

The flow to be investigated will be:

a) typical of that in a compressor

b) turbulent

c) incompressible

d) over a surface with radius of curvature large compared with the boundary layer thickness

e) steady

The choice of a compressor cascade is dictated by the need for getting a reasonably thick turbulent boundary layer while still having the required centrifugal effect in such a configuration.

Due to the complexity of the turbulent flow it is not at present possible to perform an exact analysis of the turbulent boundary layer equations. Therefore, just as is done for the two-dimensional boundary layer, computational methods must be based on momentum integral methods and empirical knowledge of the boundary layer gained by experiment. Thus, we will treat the problem by momentum integral methods together with a model of the flow, based on experiment.

For the flow-model we naturally will use the information which already is available in the literature (Refs. 7-23) but due to the earlier mentioned lack of experimental work on the present particular configuration it is felt that the experiments presented in Part 2 of this paper will fill a significant gap in our present knowledge of three-dimensional boundary layers and will serve as a check on the adequacy of the mathematical model.

1.3 The Boundary Layer Integral Equations

In this section we will outline the derivation of the equations and give the resulting equations. The detailed derivation is shown in Appendix A.

Working with the Navier-Stokes equation in vector form we transform them to a coordinate system rotating with a constant angular velocity ω. This coordinate system is shown in Figure 1 as X, Y, Z. From here we transform the equations to a streamline coordinate system x - y - z, also shown in Figure 1, using the transformations shown in Figure 2. This coordinate

system has its x-axis along a streamline just outside the boundary layer, z-axis perpendicular to the surface and y-axis perpendicular to both x and z axes in order to comprise an orthogonal system. We now introduce the regular boundary layer assumptions in the equations plus the assumption that the radius of curvature of the surface is large compared to the boundary layer thickness. The streamline coordinate system is, however, not orthogonal unless we write the equations for the special case of $y = 0$, which means that we always make the calculations following one streamline at a time. This, however, is not a severe limitation and is certainly justified for use with the boundary layer equations.

The next thing we do is to integrate the momentum equations in stream-and-cross-directions, plus the momentum equation in stream-direction multiplied with u to get the momentum-and-energy-integral equations. The usual definitions of the integrated quantities of the boundary layer are used and are shown below in our notation.

$$\begin{aligned}
\delta_x &= \frac{1}{U}\int_0^\infty (U-u)\,dz & \delta_y &= \frac{1}{U}\int_0^\infty v\,dz \\
\theta_{xx} &= \frac{1}{U^2}\int_0^\infty u(U-u)\,dz & \theta_{yy} &= \frac{1}{U^2}\int_0^\infty v^2\,dz \\
\delta_x^{**} &= \frac{1}{U^3}\int_0^\infty u(U^2-u^2)\,dz & \delta_y^{**} &= \frac{1}{U^3}\int_0^\infty v(U^2-u^2)\,dz \\
\theta_{xy} &= \frac{1}{U^2}\int_0^\infty v(U-u)\,dz & \theta_{yx} &= \frac{1}{U^2}\int_0^\infty vu\,dz
\end{aligned} \qquad (1.3\text{-}1)$$

here z is the distance from the wall; U is the magnitude of the velocity vector in the main flow at the point in question; u and v are components of the velocity-vector in the boundary layer and are parallel and perpendicular to the main flow streamline. It should be noted that all of the integrated quantities are <u>not</u> independent, but it may be seen from the definitions (1.3-1) that

$$\delta_y^* - \theta_{xy} = \theta_{yx} \qquad (1.3\text{-}2)$$

With these definitions the integral equations become:

Momentum-integral equations

$$\frac{\partial \theta_{xx}}{\partial x}+\frac{\partial \theta_{xy}}{\partial y}+\frac{1}{U}\frac{\partial U}{\partial x}(\delta_x^*+2\theta_{xx})-\left(\frac{1}{U}\frac{\partial U}{\partial y}-m\right)(\delta_y^*+2\theta_{xy})+\frac{1}{U}\frac{\partial \bar{V}}{\partial y}\theta_{xx}+\frac{2\omega_\perp}{U}\delta_y^*=\frac{C_f}{2} \qquad (1.3\text{-}3a)$$

$$\frac{\partial \theta_{yx}}{\partial x}+2\theta_{yx}\left(\frac{1}{U}\frac{\partial U}{\partial x}+\frac{1}{U}\frac{\partial \bar{V}}{\partial y}\right)+\frac{\partial \theta_{yy}}{\partial y}+\theta_{yy}\left(\frac{2}{U}\frac{\partial U}{\partial y}-m\right)-m(\theta_{xx}+\delta_x^*)-\frac{2\omega_\perp}{U}\delta_x^*=\frac{C_f}{2}\tan\alpha \qquad (1.3\text{-}3b)$$

where $m=\frac{\partial K}{\partial x}$ is the streamline curvature as defined in Figure 2; $\omega_\perp$ is the component of the angular velocity ω perpendicular to the surface; $C_f=\frac{\tau_{ox}}{\frac{1}{2}\rho U^2}$ is the skin-friction coefficient; $\bar{V}$ is the component of the main flow velocity vector perpendicular to a main-flow streamline and parallel to the y-direction. From the choice of the coordinate system this velocity-component is zero, however, the derivative $\frac{\partial \bar{V}}{\partial y}$ is not zero, but is related to the streamline divergence or convergence as can be seen in the following figure.

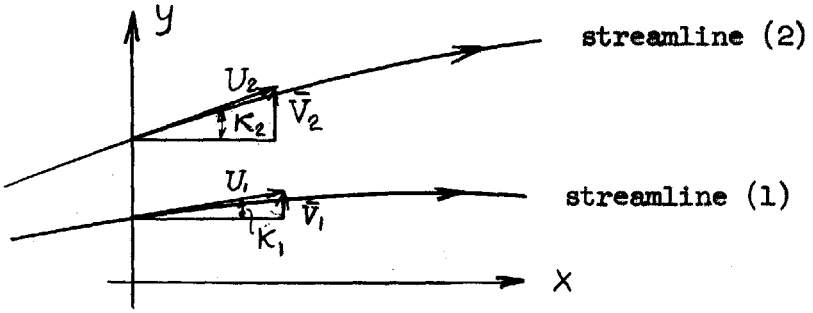

If we, for cimplicity, assume $U_1 = U_2$ we have

$$\frac{\bar{V}_1-\bar{V}_2}{y_1-y_2}\approx\frac{\Delta\bar{V}}{\Delta y}\approx U_1\frac{\Delta K}{\Delta y}$$

and if $\frac{\Delta K}{\Delta y}$ is positive the streamlines are diverging while they are converging for negative $\frac{\Delta K}{\Delta y}$.

The magnitude of the different terms in the momentum equations has been found from the experimental data presented in Part 2. The following table shows the typical magnitudes of the terms. The notation of the position is demonstrated in the following example:

50 - 70 - S

The first group, 50, gives the chord-position in percent of chord-length, starting at the leading edge.

The second group, 70, gives the span-position in percent of span-length, starting at the hub.

The third group is S or P standing for suction-side or pressure-side.

Momentum-integral equation - stream-direction

Position	$\frac{\partial \theta_{xx}}{\partial x}$;	$\frac{\partial \theta_{xy}}{\partial y}$;	$\frac{1}{U}\frac{\partial U}{\partial x}(\delta_x^* + 2\theta_{xx})$;	$-\left(\frac{1}{U}\frac{\partial U}{\partial y} - m\right)(\delta_y^* - 2\theta_{xy})$;	$\frac{1}{U}\frac{\partial \bar{V}}{\partial y}$;	$-\frac{C_f}{2}$;
50-10-P	.0032	.0006	-.0047	.0001	.0007	-.0026
50-50-P	.0043	.0002	-.0024	.00001	.0004	-.0031
90-50-P	-.0022	.0002	.0049	.0001	.0007	-.0035
70-10-S	.0101	.0003	-.0076	.00001	.0002	-.0022
70-50-S	.0132	-.0002	-.0089	-.00001	-.0009	-0024
90-50-S	.0319	-.0004	-.0262	-.00003	-.0023	-.0010

Momentum-integral Equation - cross-direction

Position	$\frac{\partial \theta_{yx}}{\partial x}$;	$2\theta_{yx}\left(\frac{1}{U}\frac{\partial U}{\partial x} + \frac{1}{U}\frac{\partial \bar{V}}{\partial y}\right)$;	$-m(\theta_{xx} + \delta_x^*)$;	$\frac{\partial \theta_{yy}}{\partial y}$;	$\theta_{yy}\left(\frac{2}{U}\frac{\partial U}{\partial y} - m\right)$;	$\frac{C_f}{2}\tan\alpha$;
50-10-P	-.0032	.0006	.0031	-00032	-.000004	-.0005
50-50-P	-.0011	.0001	.0011	-.00002	-.000003	-.00016
90-50-P	-.0011	.0001	.0011	-.00002	-.000001	-0024
70-10-S	-.0015	-.0006	.0001	-.00008	-.000001	-.00028
70-50-S	-.0015	-.0008	-.0004	-.00005	-.000002	-.00010
90-50-S	-.0049	-.0028	-.0008	-.00023	-.000012	-.00018

From the magnitude of the terms in the stream-direction we can see that the term $\left(\frac{1}{U}\frac{\partial U}{\partial y} - m\right)(\delta_y^* - 2\theta_{xy})$ is very much smaller than the rest of the terms. If we write the irrotationality condition in the streamline coordinate system we get

$$mU - \frac{\partial U}{\partial y} = -2\omega_\perp \qquad (1.3\text{-}4)$$

assuming the upstream flow to be irrotational in the stationary coordinate system.

Thus, for the experimental data where $\omega = 0$, we get

$$\frac{1}{U}\frac{\partial U}{\partial y} - m = 0$$

Thus, using the irrotationality condition (1.3-4) will intoduce a very small error in the equation.

In the cross-direction, terms involving θ_{yy} will be neglected. As can be seen from the table, the neglect of $\frac{\partial \theta_{yy}}{\partial y}$ compared with the skin-friction term can be somewhat in doubt. However, the term is small compared with the other terms which will justify the assumption.

From the tables we also can get some idea of the magnitude of the three-dimensionality in the flow. The terms $\frac{\partial \theta_{xy}}{\partial y}$ and $\frac{1}{U}\frac{\partial \bar{V}}{\partial y}\theta_{xx}$ in the streamwise equation are due to the cross-flow while $\frac{\partial \theta_{xx}}{\partial x}$, $\frac{1}{U}\frac{\partial U}{\partial x}(\delta_x^{**} + 2\theta_{xx})$ and $\frac{C_f}{2}$ also appear in the two-dimensional equation. As the three-dimensional terms are small, we expect the cross-flow to have only second order effects on the streamwise flow. Later on we theoretically will deal with the rotating case and, although the cross-flow here turns out to be two or three times that in the stationary case, we expect it only to have second order effects on the streamwise flow.

Now, using the irrotationality condition (1.3-4) and neglecting the θ_{yy}- terms, the momentum-integral equations become:

$$\frac{\partial \theta_{xx}}{\partial x} + \frac{\partial \theta_{xy}}{\partial y} + \frac{1}{U}\frac{\partial U}{\partial x}(\delta_x^* + 2\theta_{xx}) + \frac{1}{U}\frac{\partial \bar{V}}{\partial y}\theta_{xx} + \frac{4\omega_\perp}{U}\theta_{xy} = \frac{C_f}{2} \qquad (1.3\text{-}5a)$$

$$\frac{\partial \theta_{yx}}{\partial x} + 2\theta_{yx}\left(\frac{1}{U}\frac{\partial U}{\partial x} + \frac{1}{U}\frac{\partial \bar{V}}{\partial y}\right) - m(\theta_{xx} + \delta_x^*) - \frac{2\omega_\perp}{U}\delta_x^* = \frac{C_f}{2}\tan\alpha \qquad (13.\text{-}5b)$$

When integrating the energy equation we also use the irrotationality condition (1.3-4) and the result becomes:

$$\frac{1}{U^3}\frac{\partial}{\partial x}(U^3\delta_x^{**}) + \frac{\partial \delta_y^{**}}{\partial y} + \frac{1}{U}\frac{\partial \bar{V}}{\partial y}\delta_x^{**} + \frac{2\omega_\perp}{U}(3\delta_y^{**} - 2\theta_{xy}) = \frac{2(d+t)}{\rho U^3} \qquad (1.3\text{-}6)$$

where

$$\frac{d+t}{\rho} = \int_0^\delta \nu\left(\frac{\partial u}{\partial z}\right)^2 dz \qquad (1.3\text{-}7)$$

is the viscous term appearing in the equation.

2. EXPERIMENTAL PROGRAM

2.1 Introduction

Detailed measurements of the boundary layers on blades in turbomachinery has, to the author's knowledge, been restricted to essentially two-dimensional cases. A straight cascade placed in the measuring section of a windtunnel is the general approach to this problem In Reference 24, the effect of three-dimensional flow on the growth of the streamwise boundary layer was included, however, no measurements of the cross-flow were made and as a straight cascade was used the spanwise pressure gradient could be expected to be much smaller than in an actual case.

In order to get the desired pressure gradient we must use an annular cascade. This means that we cannot use a regular windtunnel but must build a special air supply.

2.2 Apparatus and Experimental Methods

Figure 3 shows a sketch of the apparatus. A blower is used to force air through the cascade, which is made up of typical compressor blades (details are given in Appendix B). In order to get the proper angle of attack and also the desired radial pressure gradient, we have chosen to generate a free vortex upstream of the cascade.

The flow, therefore, is taken out on a large radius where a set of vanes gives it a tangential velocity component. The free vortex then develops when passing through a carefully designed annular duct, which also gives constant axial velocity upstream of the cascade. It is possible to adjust the vanes to get the proper angle of attack to the blades.

The end-walls of the cascade and the duct-walls approximately two chord-lengths upstream of the cascade were made of perforated material to allow boundary layer suction. At an early stage of the experiments it was found that it was not possible to suck away all of the end-wall boundary layer,

but there was a critical value of the amount of suction to apply to the hub-end-wall. Below this critical value the hub section of the cascade was separated and the flow through the whole annulus was very unsteady while above the value the flow was steady and no sign of early separation was found. The suction was, therefore, fixed just above this critical value throughout the investigation.

There was some doubt during the construction period whether the fact that the exit plane of the cascade is exposed to atmospheric pressure would have any effect on the radial pressure gradient. In order to find out, we extended the hub end-wall about one chord-length downstream of the exit plane and made static pressure traverses in the exit plane in order to find the radial pressure gradient there, both with and without the extension. As it was not possible to detect any difference in gradient we used the cascade without the extension when taking the data. The fact is, that the pressure in the center core of the annulus is lower than the atmospheric pressure and the adjustment to atmospheric pressure occurs gradually further downstream. At the top region of the exit plane the pressure, of course, is atmospheric. Still a better check on this was obtained later when we put on a two-foot extension of both the inner and outer walls of the annulus, which was suggested by one of our sponsors. Also, in this case we got practically the same pressure gradient in the radial direction, as is shown in Figure 12. A photograph of the apparatus with this extension on is shown in Figure 4.

The measurements have been taken using three different probes. Two of them, shown in Figures 6 and 7, have been used to find free-stream data and the third, shown in Figure 8, was used to take measurements in the boundary layer. The probes were mounted on a traversing righ, shown in Figure 5. The rig allows the probes to be moved in the axial and tangential

directions and to be pivoted around a radial direction. The boundary layer measurements were taken on a blade which was mounted in slots so it could be slid radially. This blade had a row of static pressure-taps along one chord-line and, as it could be slid, the pressure distribution at any radial position could be measured. In addition to the free stream probe in Figure 7, we used a probe of the same shape which had static pressure taps to find the static pressure in the free stream. These probes, which give both yaw and pitch angles besides total and static pressure, could be used in a region extending from one chord-length upstream to one chord-length downstream of the cascade.

The other free-stream probe (Fig. 6) could be slid along the chord direction of a blade slightly outside the boundary layer so as to give an accurate measure of the free streamline curvature. This probe, as well as the boundary layer probe (Fig. 8), is a three-hole cobra probe giving total pressure and yaw angle. The boundary layer probe has a much thinner tip than the other probes and has provisions for traversing the probe across the boundary layer with the help of a micrometer. More details of the instrumentation are given in Appendix C.

2.3 General Results and Discussion

The Reynolds number based on upstream velocity and chord-length is 1.2×10^5, this is slightly low compared to an actual compressor and has the effect of keeping the boundary layer laminar over a larger portion of the blade than we expect in a compressor. This is particularly true on the suction side where transition was found to occur at 55% chord, We, therefore, chose to trip the boundary layer from laminar to turbulent motion at an earlier chord position. This is done with a tripping wire glued to the suction side at 30% chord position and the pressure side at 10% chord position.

The measurements can be split up into two groups. One group gives information on the flow outside the boundary layer, the so-called free stream conditions. This is the information we need to know in order to make the calculations of the boundary layer growth (Parts 4 and 5 of the report). The other group gives the detailed information of the boundary layer flow. This will first be used to check the assumptions of the velocity profile family for the three-dimensional boundary layer (Part 3 of the report). Secondly, it will be used to compare measured and calculated boundary layer development (Part 5 of the report).

Starting with the free-stream quantities we, in Figure 9, show the direction and magnitude of the velocities in the free stream one inch upstream from the cascade and at the exit plane. In the upstream flow there is no radial velocity component but, due to the turning of the flow through the cascade, a secondary flow has developed in the exit plane (dotted line shows the radial velocity component). It can be seen that this secondary flow is of the same kind as we find in all turning passages. In the sketch here we show this, as seen from behind the cascade.

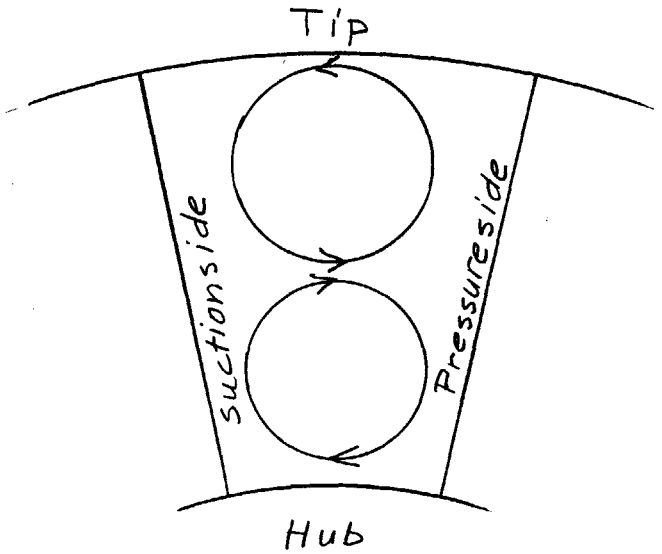

The velocity triangles for the average flow directions are also given in Figure 9.

Figure 10 shows the pressure distribution along the chord direction for different span positions and Figure 11 shows the pressure distribution along the span direction for different chord positions. On this plot, the upstream and downstream pressure distributions are also shown.

Using the total pressures recorded just outside of the boundary layer we can compute the velocity distribution on the blade. This is shown in Figure 13.

Using the yaw readings taken just outside of the boundary layer we get the angle K between the free-stream lines and the chord direction. This is shown in Figure 14.

The other group of readings are taken in the boundary layer. Combining the readings of total pressure and yaw-angle, given by the boundary layer probe with the static pressure as read on the blade surface, gives the velocities in stream and cross directions across the boundary layer. Traverses have been made at 10, 30, 40, 50, 60, 70 and 90 per cent span and 30, 50, 70 and 90 per cent chord on the pressure side and 50, 70, 85, 90 and 95 per cent span on the suction side. On the suction side an extra set of traverses have been made at 30, 50 and 70 per cent span and 50, 60, 70, 80 and 90 per cent chord. All these data are presented in Table I. The integrated quantities of the boundary layer, as defined in (1.3-1) are calculated and presented in Table II.

The data was taken mainly during August and September 1961 when the room temperature fluctuated. Due mainly to these fluctuations, the Reynolds number for the different runs varies $\pm$ 3%. This also influences the growth of the boundary layer and has to be remembered when comparing measured and calculated boundary layer quantities in Part 5 of the report. The calcul-

ations are based on the measured quantities in the free stream and, as these measurements could be done in a few hours, they do not involve any variations in Reynolds number.

Tracing of limiting streamlines on the blade surface was also done, using carbon-black dissolved in kerosene. The resulting pattern was photographed and is shown in Figure 15. The white lines are the free streamlines and the dotted lines calculated limiting streamlines, which will be considered in Part 3.

3. VELOCITY PROFILES

3.1 Introduction

In general, the velocity profiles in the streamline coordinate system look like the profiles sketched below.

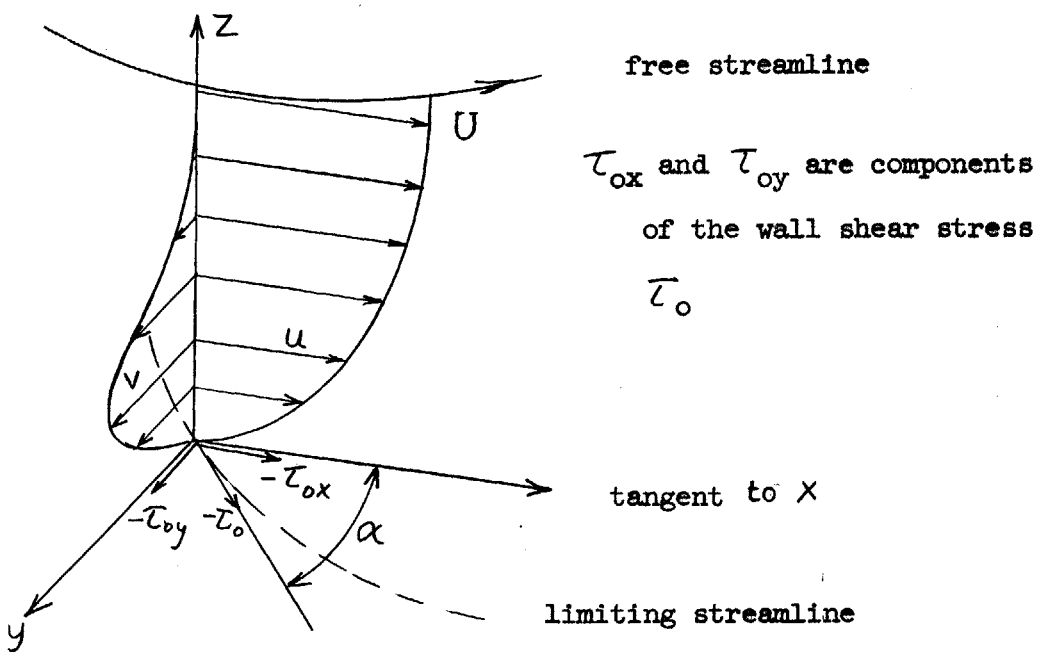

In the past, two general models of three-dimensional turbulent boundary layers have been proposed.

Prandtl (Ref. 17) suggested the assumption

$$\frac{u}{U} = G\left(\frac{z}{\delta}\right)$$

$$\frac{v}{U} = \sin\alpha\, G\left(\frac{z}{\delta}\right) g\left(\frac{z}{\delta}\right)$$

where G and g are universal functions of $\frac{z}{\delta}$ and are, in general, only restricted by the boundary layer conditions.

at $z = \delta$ $G = 1$ and $g = 0$

at $z = 0$ $G = 0$ and $g = 1$

This model is by now mostly of historical interest and work done by authors using it was nicely reviewed by Johnston (Ref. 12).

The other general model was proposed by Coles (Ref. 8). On the basis of his well-established correlation of two-dimensional turbulent velocity profiles, Coles generalized his results by proposing that the profile shape of a skewed boundary layer can be established by adding vectorially a universal wall-component of the profile to a universal wake-component.

These ideas were further extended by Nelson (Ref. 28) who also was able to derive mathematical expressions for the universal functions.

3.2 The Profile Assumption

If we look at a typical skewed velocity profile plotted in a hodograph plane

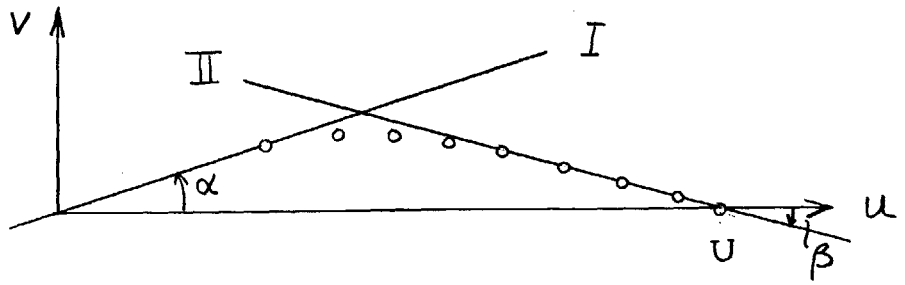

we can distinguish two directions, I and II, making angles α and β respectively with the u-axis. The angle α is the limiting streamline angle, also shown in the figure at the beginning of this paragraph. It should be noted that the point where the two directions cross each other corresponds to a point in the boundary layer very close to the wall. The main portion of the boundary layer, therefore, is described by the direction II. As the

development of the cross-flow is a direct result of the re-orientation of the vorticity in the boundary layer (Ref.29) which is mainly dependent on the turning of the free-stream, we expect the angle β to be closely related to the free stream turning.

It, therefore, seems natural that the universal wall component of the model should be directed along the I-direction and the universal wake component along the II-direction. Denoting the wall component with $F_1(\eta)$ and the wake-component $F_2(\eta)$ where $\eta = \frac{z}{\delta}$ we may write the velocity defect formulas

$$\frac{u-U}{u^*} = \frac{\cos\alpha}{k} F_1(\eta) + 2\pi \frac{\cos\beta}{k} F_2(\eta) \qquad (3.2\text{-}1a)$$

$$\frac{v}{u^*} = \frac{\sin\alpha}{k} F_1(\eta) + 2\pi \frac{\sin\beta}{k} F_2(\eta) \qquad (3.2\text{-}1b)$$

u^* is here the skin-friction velocity $u^* = \sqrt{\frac{\tau_o}{\rho}}$, k a constant and π a parameter depending on x.

Nelson (Ref. 28) calculated $F_1(\eta)$ and $F_2(\eta)$, using the measured values of u, v, U, u^*, α and β from the experiments by Johnston (Ref. 12) and Gardow (Ref. 11). From his results it appears that the wake function $F_2(\eta)$ is fairly universal, while the wall function $F_1(\eta)$ shows considerable scatter. This scatter, however, may be due to difficulties in finding α. This angle is determined from one or two of the measured points closest to the wall and considering the accuracy of yaw-measurements in a steep velocity gradient the scatter is not surprising.

Figure 16 shows a comparison of the wake function $F_2(\eta)$ as found in three-dimensional flow (Ref. 28), two-dimensional flow (Ref. 8) and regular wake flow (Refs. 19, 30, 31). The wake function

$$F_2(\eta) = \left[1 - \eta^{3/2}\right]^2 \qquad (3.2\text{-}2)$$

seems to give a good overall fit and has been chosen for this investigation.

The wall function $F_1(\eta)$ is plotted in Figure 17. The shaded area shows the data of References 11 and 12 as calculated by Nelson.

The data points were more dense towards the corner in the plot, however, it is felt that Nelson's choice of the function (dotted line) was too extreme. Coles' choice, on the other hand, is too extreme in the other direction. Our choice was, therefore, a function better fitting the average shown by the data points. The mathematical form of this function is:

$$\begin{aligned} F_1(\eta) &= \log\eta + 1.3 && 0 < \eta < 0.1 \\ &= -\, e^{(1-10\eta)} && 0.1 < \eta < \infty \end{aligned} \qquad (3.2\text{-}3)$$

In order to calculate the velocity profiles from equation (3.2-1) we need to know the angles α and β. The next step is, therefore, to express these angles in quantities we know, or are able to calculate. All free-stream quantities are assumed known and from the momentum and energy equations (1.3-5, 1.3-6) we will be able to find θ_{xx}, H and θ_{yx}.

The profile model we propose is primarily intended to be used for flow problems on blades in turbomachinery. Excluding regions close to separation, the experiments of Part 2 have shown the angles α and β to be small, so $\cos\alpha \approx \cos\beta$ should be a good assumption. Furthermore, we know from Coles' paper (Ref. 8) that $\pi \to \infty$ at separation, so $\cos\alpha\, F_1(\eta)$ will be much smaller than $2\pi\, F_2(\eta)\cos\beta$ in regions close to separation. Generally we, therefore, make a very small error writing $\cos\alpha = \cos\beta$. In this way the velocity defect formulas become

$$\frac{u-U}{u^*} = \frac{\cos\beta}{k}\left[F_1(\eta) + 2\pi\, F_2(\eta)\right] \qquad (3.2\text{-}4a)$$

$$\frac{v}{u^*} = \frac{\sin\alpha}{k} F_1(\eta) + 2\pi\, \frac{\sin\beta}{k} F_2(\eta) \qquad (3.2\text{-}4b)$$

$\cos\beta$ is also nearly one and we may find it from the inviscid theory presented in Appendix D.

In order to proceed we define the following integrated quantities

$$i_1 = -\int_0^\infty F_1\, d\eta \;;\quad i_2 = -\int_0^\infty F_2\, d\eta$$

$$i_{11} = \int_0^\infty F_1^2\, d\eta \;;\quad i_{12} = \int_0^\infty F_1 F_2\, d\eta \;;\quad i_{22} = \int_0^\infty F_2^2\, d\eta \qquad (3.2\text{-}5)$$

Using the proposed formulas for F_1 (equation 3.2-4) and F_2 (equation 3.2-3) we find

$$i_1 = 0.30;\ i_2 = 0.45;\ i_{11} = 0.552;\ i_{12} = 0.2794;\ i_{22} = 0.315 \quad (3.2\text{-}6)$$

From the definitions of the quantities δ_x^*, θ_{xx} and θ_{yx} (1.3-1) we find, using (3.2-4) and (3.2-5)

$$\frac{\delta_x^*}{\delta} = \gamma (i_1 + 2\pi i_2) \quad (3.2\text{-}7a)$$

$$\frac{\theta_{xx}}{\delta} = \gamma (i_1 + 2\pi i_2) - \gamma^2 (i_{11} + 4\pi\, i_{12} + 4\pi^2 i_{22}) \quad (3.2\text{-}7b)$$

$$\frac{\theta_{yx}}{\delta} = \gamma \left\{ \tan\alpha \left[\gamma (i_{11} + 2\pi i_{12}) - i_1 \right] + 2\pi \tan\beta \left[\gamma (i_{12} + 2\pi i_{22}) - i_2 \right] \right\} \quad (3.2\text{-}7c)$$

where $\gamma = \frac{\cos\beta}{k} \sqrt{\frac{C_f}{2}}$ (3.2-8)

Combining (3.2-7a) and (3.2-7b), using the definition of the shape-factor

$$H = \frac{\delta_x^*}{\theta_{xx}}$$

we get

$$\frac{H-1}{\gamma H} = \frac{i_{11} + 4\pi i_{12} + 4\pi^2 i_{22}}{i_1 + 2\pi i_2} \quad (3.2\text{-}9)$$

This equation is used to find π from the known values H and γ, and is plotted in Figure 18 with the i's from (3.2-6).

We now have all necessary information for the velocity profile in the stream direction. In the cross-direction we also need $\tan\alpha$ and $\tan\beta$. The inviscid solution of β together with equation (3.2-7c) could be used, however, both of these equations are mainly dependent on the outer portion of the boundary layer and can, therefore, not be expected to give a good description of the limiting streamline angle α. We, however, have one piece of information we have not used, namely, in the vicinity of the wall we expect our profile family to correspond to the "law of the wall".

Thus, for small η we have

$$F_1 = \log \eta + 1.3$$
$$F_2 \approx -1 \quad (3.2\text{-}10)$$

so equation (3.2-4)gives

$$\frac{u}{U} = 1 + \gamma(\log\eta + 1.3 - 2\pi) \tag{3.2-11a}$$

$$\frac{v}{U} = \gamma\left[\tan\alpha(\log\eta + 1.3 - 2\pi\tan\beta\right] \tag{3.2-11b}$$

Close to the wall we have a thin layer where the velocity vectors are collateral in the direction I of the hodograph plot. The "law of the wall" profile as found in two-dimensional boundary layers written along this direction give:

$$\frac{u}{U} = \frac{1}{k}\frac{C_f}{2}\cos\alpha\ (\log\frac{\delta u^*}{\nu} + \log\eta + kc) \tag{3.2-12a}$$

$$\frac{v}{U} = \frac{1}{k}\frac{C_f}{2}\sin\alpha\ (\log\frac{\delta u^*}{\nu} + \log\eta + kc) \tag{3.2-12b}$$

k and c are constants and their values for two-dimensional boundary layers were found by Coles (Ref. 8) to be $k = 0.40$; $c = 5.1$

By equating equations (3.2-11b) and 3.2-12b), using (3.2-11a) and (3.2-12a) we get

$$\tan\beta = \tan\alpha(1 - \frac{1}{2\pi\gamma}) \tag{3.2-13}$$

and combining this equation with (3.2-7c) gives us

$$\tan\alpha = \frac{\theta_{yx}/\theta_{xx}}{H(\frac{E}{\gamma} - G) - 1} \tag{3.2-14}$$

where $E = \dfrac{i_2}{i_1 + 2\pi i_2}$; and $G = \dfrac{i_{12} + 2\pi i_{e2}}{i_1 + 2\pi i_2}$

E and G are plotted in Figure 18 as functions of π.

3.3 Proposed Model

We now summarize the proposed model as follows:

Assuming the known quantities are θ_{xx}, H, θ_{yx} and the free stream conditions, we calculate $\cos\beta$ from the inviscid solution of β (Appendix D) and C_f from the skin-friction formula given in Appendix E.

The velocity distributions are then given by

$$\frac{u}{U} = 1 + \gamma\left[F_1(\eta) + 2\pi F_2(\eta)\right] \tag{3.3-1a}$$

$$\frac{v}{U} = \gamma \left[\tan\alpha \, F_1(\eta) + 2\pi \tan\beta \, F_2(\eta) \right] \qquad (3.3\text{-}1b)$$

where

$$\gamma = \frac{\cos\beta}{k} \sqrt{\frac{C_f}{2}} \qquad (3.2\text{-}2)$$

$$\tan\alpha = \frac{\theta_{yx}/\theta_{xx}}{H(\frac{E}{\gamma} - G) - 1} \qquad (3.3\text{-}3)$$

$$\tan\beta = \tan\alpha(1 - \frac{1}{2\pi\gamma}) \qquad (3.3\text{-}4)$$

$F_1(\eta)$ is plotted in Figure 17, $F_2(\eta)$ in Figure 16 and π, E and G are functions plotted in Figure 18.

3.4 Comparison of Measured and Calculated Velocity Profiles

The velocity profiles, as calculated by the model, are shown in Figure 19 and compared with the measurements. $\frac{u}{U}$ and $\frac{v}{U}$ are shown as functions of $\eta = \frac{z}{\delta}$ and also plotted against each other in the hodograph plots. The agreement is, in general, excellent, giving strong support for the usefulness of the model. Some discrepancies can, however, be noticed. The $\frac{u}{U}$ - profiles at 30% chord on the pressure side and 50% chord on the suction side do not agree as well as the rest of the profiles. This probably depends on the fact that we here are too close to the trip wire, where we do not expect the model to hold. At the 10% span-position on the suction side the calculation of the cross-flow is in poor agreement with experiment. This is due to corner effects. The cross-flow on the hub end-wall is pushing the inner part of the blade boundary layer away from the hub while the streamline curvature outside the boundary layer forces the outer part of the boundary layer to flow towards the hub.

Figure 20 shows the velocity profiles in a rotating duct. The data comes from a project investigating coriolis-generated instability in the turbulent boundary layer, currently under way in the Gas Turbine Laboratory. The profile A is taken on that side of the duct where we expect the instability to be increasing while profile B comes from the side where it is decreasing. The displacement and momentum-thicknesses have been calculated

from the measured data and the velocity profiles have then been calculated using the model. It is probably due to the increased instability that profile A has a bad fit to the measured values. However, in the case of boundary layer on blades we do not expect such instability to occur as the coriolis-force acts in the $\bar{\omega} \times \bar{U}$ direction, which is parallel to the surface.

4. BOUNDARY LAYER INTEGRAL EQUATIONS

4.1 A Simple Approximation of the Cross-flow

We now will make use of the velocity profile family in order to approximate the three-dimensional terms appearing in the streamwise equations.

In paragraph 3.2 we pointed out that the peak point in the hodograph plot of velocities u versus v corresponds to a point very close to the wall. Therefore, if we forget about the zero-velocity boundary condition at the wall we may extend the II-direction in the plot all the way to the wall and use that line to approximate the v-velocities, thus:

$$v = (u - U) \tan\beta \qquad (4.1\text{-}1)$$

The use of this equation in the integrated quantities (1.3-1) will somewhat overestimate the cross-flow. From the comparison of this simple method with the more exact one presented in paragraph 4.4, we will see that this overestimate will be less than 20% and thus justifies the use of equation (4.1-1) in the streamwise equations where the three-dimensional terms are, in any case, small compared to the two-dimensional terms.

The use of equation (4.1-1) allows us to write the following relationship between the integrated quantities (1.3-1)

$$\begin{aligned} \delta_y^* &= -H\Theta_{xx} \tan\beta \\ \Theta_{xy} &= -(H-1)\,\Theta_{xx} \tan\beta \\ \Theta_{yx} &= -\Theta_{xx} \tan\beta \\ \delta_y^{**} &= -\left[H+1-\bar{H}\right]\Theta_{xx} \tan\beta \end{aligned} \qquad (4.1\text{-}2)$$

For the streamwise momentum and energy equations we need the derivative $\frac{\partial \theta_{xy}}{\partial y}$ and $\frac{\partial \delta_y^{**}}{\partial y}$.

We expect θ_{xx} H and $\bar{H}$ to very slowly in the y-direction while β will have large variations. This also has been confirmed by the experiments, so when taking the y-derivatives of equations (4.1-2) we will assume θ_{xx}, H and $\bar{H}$ constants. Thus,

$$\begin{aligned} \frac{\partial \theta_{xy}}{\partial y} &= -(H-1)\,\theta_{xx}\left(\frac{1}{\cos\beta}\right)^2 \frac{\partial \beta}{\partial y} \approx -(H-1)\,\theta_{xx}\frac{\partial \beta}{\partial y} \\ \frac{\partial \delta_y^{**}}{\partial y} &= -(H+1-\bar{H})\;\theta_{xx}\left(\frac{1}{\cos\beta}\right)^2 \frac{\partial \beta}{\partial y} \approx -\left(H+1-\bar{H}\right)\theta_{xx}\frac{\partial \beta}{\partial y} \end{aligned} \qquad (4.1\text{-}3)$$

For this simple approximation of the cross-flow it is suggested that β be taken from the inviscid solution presented in Appendix D.

4.2 Momentum Integral Equation in the Stream Direction

Using equations (4.1-1) and (4.1-2) we can write the momentum integral equation in the stream direction (1.3-5a) as

$$\frac{\partial \theta_{xx}}{\partial x} + \theta_{xx}\left\{(H+2)\,\frac{1}{U}\frac{\partial U}{\partial x} + K(x)\right\} = \frac{C_f}{2} \qquad (4.2\text{-}1)$$

where
$$K(x) = \frac{1}{U}\frac{\partial \bar{V}}{\partial y} - (H-1)\frac{\partial \beta}{\partial y} - \frac{4(H-1)\omega_1}{U}\tan\beta \qquad (4.2\text{-}2)$$

with β from Appendix D

$$C_f = \frac{0.93\; e^{-1.56H}}{(R_\theta)^{0.47}} \qquad (4.2\text{-}3)$$

The skin-friction relation (4.2-3) is a modification of the Ludwig-Tillmann formula given in Appendix E.

In order to solve equation (4.2-1) we define an integrating factor

$$\Theta = \left(\frac{U}{U_\infty}\right)^{1.47H + 2.47}\theta_{xx}(R_\theta)^{0.47} \qquad (4.2\text{-}4)$$

then equation (4.2-1) becomes

$$\frac{\partial \Theta}{\partial x} + \Theta\, M(x) = N(x) \qquad (4.2\text{-}5)$$

where
$$M(x) = K(x) - \frac{\partial H}{\partial x}\log\frac{U}{U_\infty} \qquad (4.2\text{-}6a)$$

$$N(x) = 0.683\left(\frac{U}{U_\infty}\right)^{1.47H + 2.47} e^{-1.56H} \qquad (4.2\text{-}6b)$$

The total derivative can be substituted for the partial derivative of Θ as $\frac{d\Theta}{dx} = \frac{\partial\Theta}{\partial x} + \frac{\partial\Theta}{\partial y}\frac{dy}{dx}$, where $\frac{dy}{dx} = 0$ along a streamline.

Equation (4.2-5) is a linear first order differential equation and has the solution

$$\Theta = e^{-\int_{x_o}^{x} M dx} \left\{ \int_{x_o}^{x} Ne^{\int_{x_o}^{x} M dx} dx + \Theta_o \right\} \qquad (4.2\text{-}7)$$

Subscript o refers to initial condition while oo refers to an arbitrarily chosen position. It is suggested that a position slightly upstream of the expected separation point will be chosen $\frac{\partial H}{\partial x}$ is large here so such a choice minimizes the influence of the term $\frac{\partial H}{\partial x} \log \frac{U}{U_{oo}}$ in the equation. We, therefore, expect a rough guess of the H variation to be enough for the solution (4.2-7). Comparing with two-dimensional theory we know that a good description of the momentum thickness growth is obtained by assuming H constant.

4.3 Energy Integral Equation in the Stream Direction

Although we do not need to know the shape-factor H very accurately for calculating the growth of θ_{xx}, it is of interest for the overall boundary layer development and particularly for separation prediction. Naturally if the initial assumptions of the H distribution are too much off from the distribution calculated in this section, we should go back and recalculate the momentum thickness with the more correct distribution.

In two-dimensional theory there exist several methods to predict the shape-factor. Stewart (Ref. 32) compared the different methods and his comparison showed the Truckenbrodt method, using the energy equation for shape-factor calculations to give the best comparison with experiments. We, therefore, will use the three-dimensional energy equation in this case.

Using the relations (4.1-1) and (4.1-2), we can write the energy integral equation (1.3-6) as:

$$\frac{1}{U^3}\frac{\partial}{\partial x}\left(U^3 \bar{H}\, \theta_{xx}\right) - \theta_{xx}\, Q(x) = \frac{2(d+t)}{\rho U^3} \tag{4.3-1}$$

where: $\bar{H}$ is the second shape-factor

$$\bar{H} = \frac{\delta_x^{**}}{\theta_{xx}} \tag{4.3-2}$$

$$Q(x) = (H+1-\bar{H})\frac{\partial \beta}{\partial y} - \frac{1}{U}\frac{\partial \bar{V}}{\partial y} H + \frac{2\omega_\perp}{U}(H-3\bar{H}+5)\tan\beta \tag{4.3-3}$$

with β from Appendix D.

$$\frac{d+t}{U^3\rho} = \frac{KC_f}{2n(\frac{2}{n}+1)} \tag{4.3-4}$$

with

$$n = \frac{1}{0.54\,H - 0.58} \tag{4.3-5}$$

$$\bar{H} = \frac{H}{0.81\,H - 0.37} \tag{4.3-6}$$

These last three equations are derived in Appendix F.

Combining equations (4.3-1) with the momentum integral equation (4.2-1) multiplied by $\bar{H}$ gives

$$\frac{\partial \bar{H}}{\partial x} + \frac{1}{U}\frac{\partial U}{\partial x}\left[3\bar{H} - \bar{H}(H+2)\right] - Q(x) - \bar{H}K = \frac{1}{\theta_{xx}}\left[\frac{2(d+t)}{\rho U^3} - \bar{H}\,\frac{C_f}{2}\right]$$

This can be rewritten using equation (4.3-6) as

$$\frac{dH}{(2.18H - 1)(H-1)H} = -\frac{dU}{U} + \left\{\frac{C_{fP}}{2\theta_{xx}} + Q_2\frac{\partial \beta}{\partial y} + Q_3\frac{\omega_\perp}{U}\tan\beta\right\} dx$$

or in integrated form

$$\int_{H_o}^{H} \frac{dH}{(2.18H-1)(H-1)H} = \log\frac{U_o}{U} + \int_{x_o}^{x}\left\{\frac{C_{fP}}{2\theta_{xx}} + Q_2\frac{\partial \beta}{\partial y} + Q_3\frac{\omega_\perp}{U}\tan\beta\right\} dx \tag{4.3-7}$$

Here

$$P = \frac{1}{H-1} - \frac{6.4\,(1.625H - 0.745)(0.54H - 0.58)}{H(H-1)(0.54H - 0.08)}$$

$$Q_2 = 1 - \frac{(1.625H - 0.745)(1+H-\bar{H})}{2H(H-1)} \tag{4.3-8}$$

$$Q_3 = 4 - \frac{(1.625H - 0.745)(5+H-3\bar{H})}{H(H-1)}$$

P, Q_2 and Q_3 are functions of H shown in Figure 21. The total derivations can be substituted for the partial as we are following one streamline at a time.

The solution of equation (4.3-7) is done in steps as we must assume a value of H in order to get the increment of the integral on the right hand side of the equation. θ_{xx} is found from the solution (4.2-7), C_f from equation (4.2-3) and β from the inviscid solution (Appendix D).

The integral on the left hand side of the equation can be plotted once for all. This is also shown in Figure 21 with $H_o = 1.2$. A step-size of $\frac{x}{c} = .1$ was used in the calculations.

4.4 Momentum-Integral Equation in Cross-Direction

The momentum-integral equation in the cross-direction (1.3-5b) contains the limiting streamline angle α. Using equations (3.2-14) of the profile family to express α we get

$$\frac{\partial \theta_{yx}}{\partial x} + \theta_{yx}\left[\frac{2}{U}\frac{\partial U}{\partial x} + M_1(x)\right] = N_1(x) \tag{4.4-1}$$

where

$$M_1(x) = \frac{2}{U}\frac{\partial \bar{V}}{\partial y} + \frac{C_{f/2}}{\theta_{xx}\left\{H\left[\frac{E}{\gamma} - G\right] - 1\right\}} \tag{4.4-2a}$$

$$N_1(x) = \theta_{xx}\left[m(H+1) + \frac{2H\omega_1}{U}\right] \tag{4.4-2b}$$

The solution of equation (4.4-1) is

$$\theta_{yx} = \left(\frac{U_o}{U}\right)^2 e^{-\int_{x_o}^{x} M_1\,dx}\left\{\int_{x_o}^{x} N_1(x)\left(\frac{U}{U_o}\right)^2 e^{\int_{x_o}^{x} M_1\,dx}\,dx + (\theta_{yx})_o\right\} \tag{4.4-3}$$

4.5 Application of the Computation Scheme

The computation scheme presented in paragraphs 4.1 - 4.4 has been applied to three cases.

1) The three-dimensional case investigated in the experimental program

2) The corresponding two-dimensional case

3) The corresponding three-dimensional case with the blades rotating

For the first case all the necessary information about the free stream was measured. In the second case the same free-stream data was used, but all terms directly related to the three-dimensionality were dropped (that

means, $m = 0$; $\frac{\partial \beta}{\partial y} = 0$; $\frac{\partial \bar{v}}{\partial y} = 0$; $\omega = 0$). The third case is described in Appendix G. In order to get a corresponding case we have chosen the rotating stage symmetric to the stator at 50% span position. The calculations for this case were carried out for 30, 50 and 70% span. However, only the 50% span calculation is a truly corresponding case so the other two span-positions are merely calculated to show the trend in the changes of the cross-flow. The first two cases have been calculated for 10, 30, 50, 70 and 90% span. The results of the calculations are shown in Figure 22. The curves show the calculated quantities and the symbols the measured quantities. Suction side is indicated S and pressure side P.

The momentum thickness θ_{xx} is shown in the graph on top of each figure page. The agreement between theory and experiments is good. This, of course, partly depends on the fact that the starting values for the calculations were taken from measurements. In an actual case we do not have that information, but must calculate the starting value using laminar theory (Refs. 1-4). There was no point in doing so for our case as we have the tripping wires on the blades which certainly will change the momentum growth. The difference between the three and two-dimensional cases is mainly due to the streamline convergence or divergence. When the streamlines converge they will feed more fluid into the boundary layer. This is the case on the main portion of the suction side an will increase the momentum thickness as is shown by the calculation. The opposite is true for the pressure side. For the two end positions, 10 and 90% span, on the suction side, the free streamlines are diverging while the streamlines within the boundary layer still are converging. As a result these positions do not show any difference between two and three-dimensional theory.

The difference between the calculated values for the three cases is of the same order of magnitude as the error we can expect to have in the

calculations. The calculations show, however, the magnitude and direction of the difference and we have to remember that the case tested had a constant height of passage while, in general, an actual stage of a turbo-machinery has a changing passage-height. This will magnify the streamline convergence or divergence, and thus give a larger difference between two and three-dimensional theory.

The middle graphs on Figure 22 show the growth of the shape-factor H. The calculations here showed no difference between the different cases. This is the result of the fact that the streamline curvature has very little influence in the equation. The comparison between theory and experiments is extremely good for the 30, 50 and 70% span positions. The calculated values at 10 and 90% positions on the suction side are somewhat low, which may depend on corner effects. It is interesting to note that the initial value of H had very little effect on the growth. For example, on the suction side we have shown the initial value to be $H_o = 1.58$ at 40% chord. This was suggested by the experiments, however, calculations were also made with $H_o = 1.4$ and $H_o = 1.75$, giving practically the same curve from 60% chord and on.

The bottome graphs on Figure 22 show the crosswise momentum thickness θ_{yx}. Calculations have been done using both the inviscid theory of paragraph 4.1 and the viscous theory of paragraph 4.4. For the inviscid calculations the initial condition was zero cross-flow at the leading edge while the viscous theory used the measured initial condition. Considering this difference in initial condition it is surprising how well the inviscid theory predicts the cross-flow and due to its simplicity both in initial condition and actual calculation it might well be recommended for practical use.

The calculations compare reasonably well with the experiments. As could be anticipated from errors in the yaw-measurements, we have a larger spread of the data points in the cross-flow than in the streamwise flow. This is particularly observed at 30 and 50% span, where three points seem to be off compared with the rest of the points. These three points correspond to a different run and may have slightly different free-stream conditions.

The influence of the rotation is the next thing we will discuss. First, we can see that the direction of the cross-flow will be reversed. Secondly, the magnitude of the cross-flow is two to three times as large in the rotating as in the stationary case. On the suction side the cross-flow is fairly constant at different span-positions, but increases sharply with the radius on the pressure side. Thus, secondary losses generated by the cross-flow will be larger in a rotating than in a stationary cascade.

The boundary layer equations used in part 4, as well as the velocity-profile family have been restricted to small cross-flow. The experiements have shown us that this is a reasonably assumption in the stationary case. One reason for doing the calculations of the rotating case was to find if the same assumption holds. We, therefore, have plotted the velocity-profiles of the rotating case in the hodograph plots of Figure 19 for the 50% span-position. It is seen that although the cross-flow may be two or three times as large in this case, we still have cross-flow velocities of the order 1/10 of the streamwise velocities and thus the assumption of small cross-flow is valid.

4.6 Loss Parameter m_1

The overall influence of the three-dimensionality on the losses in the cascade can best be seen from the loss-parameter m_1, defined by Stewart (Ref. 33) as:

$$m_1 = \frac{(\theta_{xx})_t}{s\cos\beta_2 - t - (\delta_x^*)_t}$$

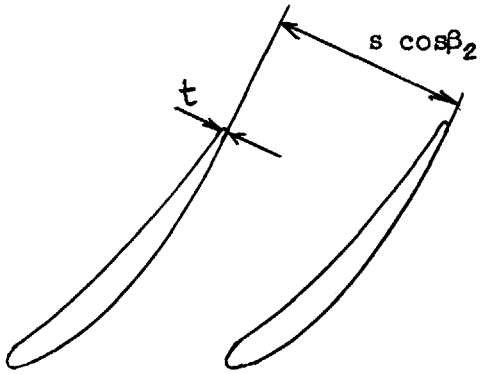

where subscript t means the sum of the thicknesses from suction and pressure sides at the trailing edge $(\frac{x}{c} = 1)$. This is the loss expressed as a fraction of the momentum of the free-stream flow, and was shown by Stewart to be proportional to the two-dimensional losses of a cascade.

m_1 has been found for the three cases of our calculation and is presented in Figure 23. It is seen that the three-dimensional case in average has about 10% higher loss than the two-dimensional case and that the rotating case shows another 10% higher loss than the stationary three-dimensional case. In an actual turbo-machine where we do not have a constant height of the passage we may get still larger differences.

In the same plot is shown a parameter m_2 based on the cross-flow and defined as:

$$m_2 = \frac{(\theta_{yx})_t}{s\cos\beta_2 - t - (\delta_x^*)_t}$$

No attempt has been made in this investigation to study the mechanism of loss generation by the cross-flow. It might be the generation of a corner vortex or too early separation of the flow in the corners, but whatever the mechanism is, we can strongly expect that it will be influenced by the cross-flow. The cascade loss generated in the boundary layer of the blade walls can, therefore, be expected to be proportional to

$$m_1 + km_2$$

where k is a constant awaiting further investigation.

5. SUMMARY

1) The boundary layer integral equations for three-dimensional boundary layers are developed for the streamline coordinate system. Terms related to skewing effects are compared to the other terms in the equations.

2) Experiments conducted on an annular cascade of compressor blades provided a significant amount of useful information on the nature of three-dimensional turbulent boundary layers. The qualitative observations have forwarded the present-day empirical knowledge of the turbulent boundary layer with cross-flow.

3) A model, based on experimental information, was developed to calculate the velocity-profiles in stream and cross-directions. Basically it was assumed that the velocity-profiles can be described by two universal functions and four parameters depending on the "input" quantities, which were the free-stream conditions, the momentum thicknesses Θ_{xx} in stream direction and Θ_{yx} in cross-direction and the shape-factor H.

The universal profiles were chosen so as to fit the two-dimensional data presented by Coles (Ref. 8) and the three-dimensional data presented by Nelson (Ref. 28). The relations between the four parameters and the "input" quantities were then found purely mathematically.

4) The model was applied to the data of the conducted experiment. The "input" quantities were found from the measurements.

5) An approximation of the cross-flow was found from using inviscid theory together with the model's description of the cross-flow velocities in the outer part of the boundary layer.

6) The boundary layer integral equations were simplified and solved using the empirical knowledge gained from the experiments and the velocity-profile model.

7) A loss parameter expressing the loss as a function of the momentum of the free-stream flow was defined and an extension to include the cross-flow was suggested.

8) Summary of formulas

Momentum thickness in stream direction

$$\frac{\theta_{xx}}{c} = \left\{ \frac{\Theta/c}{(U/U_{oo})^{1.47H + 2.47}\,(R_c)^{0.47}} \right\}^{0.68}$$

where Θ is given by equation (4.2-4)

$$R_c = \frac{Uc}{\nu}$$

Shape-factor equation

$$\int_{H_o}^{H} \frac{dH}{(2.18H-1)(H-1)H} = \log \frac{U_o}{U} + \int_{x_o}^{x} \left\{ \frac{C_f P}{2\theta_{xx}} + Q_2 \frac{\partial \beta}{\partial y} + Q_3 \frac{\omega_1}{U} \tan\beta \right\} dx$$

where P, Q_2 and Q_3 are functions of H shown in Figure 21.

Momentum thickness in cross-direction

$$\theta_{yx} = \left(\frac{U_o}{U}\right)^2 e^{-\int_{x_o}^{x} M_1 dx} \left\{ \int_{x_o}^{x} N_1 \left(\frac{U}{U_o}\right)^2 e^{\int_{x_o}^{x} M_1 dx}\, dx + (\theta_{yx})_o \right\}$$

where M_1 and N_1 are functions of x given by equations (4.4-2a) and (4.4-2b).

The velocity-profile distribution and the relations among integ-quantities, model parameters and skin-friction

$$\frac{u}{U} = 1 + \gamma \left[F_1(\eta) + 2\pi F_2(\eta) \right]$$

$$\frac{v}{U} = \gamma \left[\tan\alpha\, F_1(\eta) + 2\pi \tan F_2(\eta) \right]$$

The universal functions:

$$F_1 = \log \eta + 1.3 \qquad 0 < \eta < 0.1$$

$$= -e^{(1-10\eta)} \qquad 0.1 < \eta < \infty$$

$$F_2 = -\left[1 - \eta^{3/2}\right]^2 \qquad 0 < \eta < 1$$

$$= 0 \qquad 1 < \eta < \infty$$

$$\gamma = \frac{\cos\beta}{k}\sqrt{\frac{C_f}{2}}$$

$$\frac{H-1}{\gamma H} = \frac{i_{11} + 4\pi\, i_{12} + 4\pi^2\, i_{22}}{i_1 + 2\pi\, i_2}$$

$$\tan\alpha = \frac{\theta_{yx}/\theta_{xx}}{H\left(\frac{E}{\gamma} - G\right) - 1}$$

$$\tan\beta = \tan\alpha\left(1 - \frac{1}{2\pi\gamma}\right)$$

i_1, i_2, i_{11}, i_{12} and i_{22} are integrated quantities given by equation (3.2-6). E and G are functions of π shown in Figure 18.

6. CONCLUSIONS AND SUGGESTIONS FOR FURTHER WORK

An annular cascade, rotating or stationary, in general, has a pressure gradient along its radial direction. This gradient is dependent on the centrifugal force generated by the tangential component of the absolute velocity vector. The effect of this force on the turbulent boundary layer of the blades has been studied.

It is found that the cross-flow which developes in the boundary layer is small with velocities of the order 1/10 of the through-flow velocities.

A theoretical velocity distribution involving two "universal" analytical functions, originally suggested by Coles (Ref. 8), has been suggested. This method of profile description has been used with success in the turbulent part of the boundary layer, however, in the corners where the flow is very complex the method proved to be inadequate.

Solutions to the boundary layer integral equations have been found for the case of small cross-flow. The calculated and measured boundary layer quantities agreed within the accuracy of the measurements. A simple inviscid theory gave surprisingly good results in describing the cross-flow.

The cascade investigated was typical for a compressor and showed the average loss to be of the order 10% higher when the boundary layer was three-dimensional instead of two-dimensional. The rotating cascade, as compared with the stationary, also showed an average loss of the order 10% higher.

For further research it is believed that the main effort should be directed towards the flow outside the boundary layer. The main difficulty in calculating the boundary layer growth lies in finding the free-stream data. It has not been possible to calculate the proper pressure distribution on the blades used in the experiments by available potential flow methods, so this is a field for further investigation.

REFERENCES

1) Olsson, E. K. A. - "Boundary Layer on a Rotating Blade" - M. S. Thesis Massachusetts Institute of Technology - Cambridge, Mass. - 1960

2) Graham, M. E. - "Calculation of Laminar Boundary Layer Flow on Rotating Blades" - Ph. D. Thesis - Cornell University - Ithaca, N. Y. - 1954

3) Smith, W. E. - "Some Examples of Laminar Boundary Layer Flow on Rotating Blades" - M. Aero. E. Thesis - Cornell University - Ithaca, N. Y. - 1952

4) Fogarty, L. E. - "The Laminar Boundary Layer on a Rotating Blade" - J. of Aero. Scienc., Vol. 18, pp. 247-285 - 1951

5) NACA RM E56 B03b - "Aerodynamic Design of Axial-Flow Compressors" - Vol. III, Chaps. XIV and XV - 1956

6) Dettmering, W. - "Experimental Untersuchungen an einer Axialen Turbinenstufe" - Forchungsberichte des Landes Nordrhen-Westfalen - No. 908 - 1960

7) Clauser, F. H. - "The Turbulent Boundary Layer" - Adv. in App. Mech. - Vol. IV, pp. 1-51 - 1956

8) Coles, D. - "The Law of the Wake in the Turbulent Boundary Layer" - J. of Fl. Mech. - Vol. 1, Part 2, pp. 191-226 - 1956

9) Coles, D. - "Remarks on the Equilibrium Turbulent Boundary Layer" - J. of Aero. Scien. - Vol. 24, No. 7, pp. 495-506 - 1957

10) Cooke, J. C. - "A Calculation Method for Three-Dimensional Turbulent Boundary Layers" - RAE TN Aero 2576 - 1958

11) Gardow, E. B. - "The Three-Dimensional Turbulent Boundary Layer in a Free Vortex Diffuser" - M. I. T. - Gas Turbine Laboratory Report No. 47 - 1958

12) Johnston, J. P. - "Three-Dimensional Turbulent Boundary Layer" - M. I. T. Gas Turbine Laboratory Report No. 39 - 1957 Also: Trans. ASME - Vol. 82, Ser. D., pp. 233-250 and pp. 622-628 - 1960

13) Kuethe, A. M., P. B. McKee and W. H. Curry - "Measurements in the Boundary Layer of a Yawed Wing" - NACA TN No. 1946 - 1949

14) Mayer, A. - "Generalization of Boundary Layer Momentum-Integral Equations to Three-Dimensional Flows Including those of Rotating System" NACA Report 1067 - 1952

15) Moore, F. K. - "Three-Dimensional Boundary Layer Theory" - Adv. in App. Mech. - Vol. IV, pp. 159-228 - 1956

16) Moore, R. W. Jr. and D. L. Richardson - "Skewed Boundary Layer Flow near the End-Walls of a Compressor Cascade" - Trans. ASME - Vol. 79, No. 8 - 1957

17) Prandtl, L. - "On Boundary Layers in Three-Dimensional Flow" - Reps. and Trans. No. 64 - British M. A. P.

18) Spence, D. A. - "The Development of Turbulent Boundary Layer" - J. Aero. Scien. - Vol. 23, pp. 3-15 - 1956

19) Schlichting, H. - "Boundary Layer Theory" - McGraw-Hill Book Co., Inc. New York, N. Y. - 1960

20) Proceedings of a Symposium held at the National Physical Laboratory entitled: "Boundary Layer Effects in Aerodynamics" - Her Majesty's Stationery Office - London - 1955

21) Blackman, D. R. and P. N. Joubert - "The Three-Dimensional Turbulent Boundary Layer" - J. Roy. Aero. Soc. - Vol. 64, pp. 692-694 - Nov. 1960

22) von Doenhoff, A. F. and N. Tetervin - "Determination of General Relations for the Behavior of Turbulent Boundary Layers" - NACA Report No. 772 - 1943

23) Taylor, E. S. - "The Skewed Boundary Layer" - Trans. ASME - Ser. D, Vol. 81, pp. 297-304 - 1959

24) Peterson, C. R. - "Boundary Layer on an Airfoil in a Cascade" - M. I. T. Gas Turbine Laboratory Report No. 49 - 1958

25) Flow Corporation Direction Insensitive Static Pressure Probe - Flow Corporation - Cambridge, Mass.

26) Dean, R. C., Jr. - "Aerodynamic Measurements" - M. I. T. - Gas Turbine Laboratory - 1953

27) Davies, P. O. A. L. - "The Behavior of a Pitot Tube in Transverse Shear" - J. of Fl. Mech. - Vol. 3, Part 5, pp. 453-454 - 1958

28) Nelson, W. G. - "Skewed Turbulent Boundary Layer" - M. I. T. - Gas Turbine Laboratory Report No. 55 - 1959

29) Squire, H. B. and K. G. Winter - "The Secondary Flow in a Cascade of Airfoils in a Non-Uniform Stream" - J. Aero. Scien. - Vol. 18, pp. 271-273 - 1951

30) Schaub, Uwe, W. - "The Behavior of a Wake in an Adverse Pressure Gradient" - M. I. T. - Gas Turbine Laboratory Report No. 62 - 1961

31) Hill, P. G. - "Turbulent Wakes in Pressure Gradients" - M. I. T. - Gas Turbine Laboratory Report No. 65 - 1962

32) Stewart, C. C. - "A Comparison of Turbulent Boundary Layer Theories" M. I. T. - Gas Turbine Laboratory Report No. 57 - 1960

33) Stewart, L. W., W. T. Whitney and R. Y. Wong - "A Study of Boundary Layer Characteristics of Turbomachine Blade Rows and Their Relation to Overall Blade Loss" - Trans. ASME - Vol. 82, Ser. D, p. 588 - 1960

34) Ludwieg, H. and W. Tillmann - "Investigation of the Wall-Shearing Stress in Turbulent Boundary Layers" - NACA TM 1285 - 1952

35) Truckenbrodt, E. - " A Method of Quadrature for Calculation of the Laminar and Turbulent Boundary Layer in Case of Plane and Rotationally Symmetric Flow" - NACA TM 1379 - 1955

36) Rotta, J. - "Näherungsverfahren zur Berechnung Turbulenten Grenzschichten unter Benutzung des Energiesatzes" - Mitteilungen aus dem Max-Planck-Institute für Strömungsforschung, Nr. 8 - Göttingen - 1953

37) Pankhurst, R. C. and D. W. Holder - "Wind Tunnel Technique" - Sir Isaac Pitman and Sons, Ltd. - London - 1952

LIST OF SYMBOLS

$c = 2.8"$	
$C_f = \frac{\tau_{ox}}{\rho U^2}$	skin friction coefficient along main flow streamline
d	distance between Z-axis and axis of rotation
F_1	universal wall function equation (3.2-3)
F_2	universal wake function equation (3.2-2)
$h_1\ h_2\ h_3$	stretching factors (Appendix A)
$H = \frac{\delta^*_x}{\theta_{xx}}$	shape factor
$\bar{H} = \frac{\delta^{**}_{xx}}{\theta_{xx}}$	second shape factor
i	integrated quantities defined in equation (3.2-5)
$K(x)$	function defined in equation (4.2-2)
$k = 0.40$	constant in the "law of the wall"
$\ell = 5"$	span length
$m = \frac{\partial K}{\partial x}$	curvature of main flow streamline
$m_1\ m_2$	parameters of section 4.6
M, N	functions defined in equation (4.2-6)
M_1, N_1	functions defined in equation (4.4-2)
$P_o\ P_s\ P_{atm}$	stagnation, static and atmospheric pressure respectively
P	pressure side
$P\ Q_2\ Q_3$	functions defined in equation (4.3-8)
$\bar{Q}\ \bar{q}$	velocity vector in main stream and boundary layer respectively
$R_\theta = \frac{U\theta_{xx}}{\nu}$	Reynolds number based on momentum thickness
R	radius from center of rotation to stagnation point
S	suction side
s	distance

t	trailing edge thickness
U_j	upstream velocity at a fixed position
U	main stream velocity in streamline coordinate
$u\ v\ w$	components of boundary layer velocity in streamline coordinate system
$\bar{U}\ \bar{V}$	components of main stream velocity in curvilinear coordinate system
$\bar{u}\ \bar{v}\ \bar{w}$	components of boundary layer velocity in curvilinear coordinate system
$u^* = \sqrt{\frac{\tau_o}{\rho}}$	skin friction velocity
$X\ Y\ Z\ ;\ x\ y\ z$	cartesian, respectively streamline, coordinate systems
α	limiting streamline angle
β	velocity profile parameter
$\gamma = \frac{\cos\beta}{k}\frac{u^*}{U}$	
δ	boundary layer thickness
$\eta = z/\delta$	
$\theta\ \beta_1\ \beta_2$	angles defined in Figure 9
$\delta_x^*\ \theta_{xx}\ \delta_x^{**}\ \delta_y^*$ $\theta_{xy}\ \theta_{yx}\ \delta_y^{**}$	integrated quantities defined in equation (1.3-1)
$\ominus$	integrating factor defined in equation (4.2-4)
K	angle between main flow streamline and chord direction
$\sigma = \frac{c}{s}$	solidity
ψ	angle between z and Z directions
π	velocity profile parameter
ρ	density
ν	kinematic viscosity
τ_o	shear stress at wall

τ_{ox} τ_{oy} components of τ_o

ω angular velocity

$\omega_\perp = \omega \cos\beta$ component of angular velocity perpendicular blade surface

Subscripts

s stagnation point

o initial value

oo arbitrary value

j upstream value

TABLE I

Velocity-Profiles

z/δ	u/U	-v/U
	30 - 10 - P	
.055	.529	.0726
.091	.635	.0707
.182	.737	.0523
.273	.793	.0418
.364	.849	.0305
.455	.890	.0231
.545	.929	.0144
.637	.948	.0120
.728	.973	.0063
.818	.982	.0021
.909	.988	.0005
1.00	1.00	.00
	70 - 10 - P	
.038	.511	.0889
.063	.632	.0973
.125	.715	.0946
.219	.773	.0815
.313	.815	.0702
.407	.862	.0580
.500	.899	.0448
.594	.935	.0341
.688	.961	.0263
.782	.971	.0156
.875	.994	.0087
1.00	1.00	.00
	30 - 30 - P	
.092	.594	.0453
.154	.702	.0413
.184	.730	.0387
.231	.764	.0330
.308	.810	.0258
.462	.884	.0148
.615	.927	.0071
.769	.961	.0041
.847	.973	.0029
.923	.986	.0007
1.0	1.0	.000
	70 - 30 - P	
.057	.528	.0639
.095	.668	.0668
.238	.785	.0520
.381	.845	.0358
.523	.894	.0230
.667	.941	.0159
.809	.974	.0103
.904	.983	.0028
1.0	1.0	.000

z/δ	u/U	-v/U
	50 - 10 - P	
.046	.526	.0744
.077	.681	.0825
.154	.744	.0726
.231	.788	.0631
.308	.829	.0583
.385	.874	.0460
.462	.902	.0416
.539	.928	.0333
.615	.952	.0272
.693	.975	.0163
.769	.984	.0160
.846	.988	.0086
.923	.994	.0037
1.00	1.000	.00
	90 - 10 - P	
.035	.569	.0812
.059	.695	.0853
.177	.815	.0795
.994	.868	.0687
.412	.910	.0573
.529	.947	.0437
.642	.973	.0287
.765	.985	.0175
.883	.992	.0107
1.00	1.00	.00
	50 - 30 - P	
.071	.532	.0532
.118	.695	.0461
.235	.773	.0326
.353	.829	.0244
.471	.877	.0154
.588	.906	.0077
.765	.955	.0025
.883	.976	.0008
1.0	1.0	.000
	90 - 30 - P	
.050	.566	.0715
.083	.709	.0651
.250	.830	.0469
.471	.888	.0312
.583	.941	.0185
.750	.974	.0117
.916	.988	.0040
1.0	1.0	.000

Table I - cont.

z/δ	u/U	-v/U
	30 - 40 - P	
.100	.593	.0264
.167	.714	.0247
.250	.792	.0173
.417	.874	.0096
.584	.935	.0077
.750	.974	.0031
.917	.996	.0018
1.00	1.00	.0
	70 - 40 - P	
.054	.612	.0427
.098	.686	.0419
.179	.766	.0390
.312	.828	.0257
.447	.880	.0200
.580	.921	.0119
.714	.955	.0090
.848	.980	.0048
1.00	1.00	.0
	30 - 50 - P	
.10	.602	.0184
.167	.688	.0166
.250	.780	.0132
.400	.870	.0057
.583	.920	.0024
.750	.962	.0007
.917	.990	.0002
1.00	1.00	.0
	70 - 50 - P	
.057	.557	.0366
.095	.666	.0395
.190	.783	.0390
.333	.842	.0306
.476	.886	.0189
.619	.931	.0132
.762	.967	.0076
.904	.985	.0048
1.0	1.0	.0
	30 - 60 - P	
.092	.585	.0039
.154	.739	.0041
.308	.843	.0041
.462	.886	.0019
.616	.940	.0019
.770	.974	.0014
.923	.995	.0007
1.00	1.000	.000

z/δ	u/U	-v/U
	50 - 40 - P	
.069	.574	.0362
.115	.655	.0360
.230	.766	.0287
.345	.825	.0229
.460	.862	.0176
.575	.904	.0123
.690	.937	.0101
.805	.967	.0081
.920	.974	.0025
1.00	1.00	.0
	90 - 40 - P	
.044	.593	.0672
.074	.714	.0545
.185	.818	.0460
.296	.861	.0349
.482	.905	.0237
.592	.936	.0180
.703	.960	.0139
.925	.991	.0035
1.00	1.00	.0
	50 - 50 - P	
.075	.562	.0241
.125	.689	.0255
.250	.791	.0200
.375	.843	.0127
.500	.880	.0091
.625	.930	.0058
.750	.959	.0049
.875	.983	.0017
.938	.990	.0008
1.00	1.0	.0
	90 - 50 - P	
.048	.589	.0374
.080	.741	.0426
.240	.848	.0320
.400	.899	.0245
.560	.945	.0177
.720	.968	.0017
.880	.987	.0
1.00	1.00	.0

Table I - cont.

z/δ	u/U	-v/U
	50 - 60 - P	
.059	.548	.0167
.098	.622	.0158
.196	.756	.0169
.294	.802	.0109
.392	.846	.0102
.490	.884	.0077
.588	.917	.0056
.686	.947	.0046
.784	.967	.0020
.882	.981	.0010
.980	.994	.000
1.00	1.00	.000
	90 - 60 - P	
.043	.587	.0343
.071	.725	.0386
.179	.820	.0316
.286	.864	.0217
.393	.898	.0152
.500	.930	.0118
.607	.951	.0085
.786	.972	.0034
.893	.987	.0012
1.00	1.00	.000
	50 - 70 - P	
.071	.563	.0
.118	.697	.0
.235	.778	.0
.353	.826	.0
.471	.867	.0
.588	.905	.0
.706	.938	.0
.824	.958	.0
.942	.974	.0
1.00	1.0	.0
	90 - 70 - P	
.050	.582	.0284
.083	.712	.0258
.208	.814	.0225
.333	.863	.0152
.458	.901	.0095
.584	.932	.0048
.708	.959	.0036
.833	.982	.0014
.958	.996	.0003
1.00	1.0	.0

z/δ	u/U	-v/U
	70 - 60 - P	
.049	.535	.0246
.081	.644	.0290
.203	.781	.0214
.325	.831	.0164
.447	.884	.0145
.569	.922	.0063
.692	.958	.0062
.813	.980	.0024
.895	.993	.0003
1.00	1.00	.000
	30 - 70 - P	
.100	.557	.0047
.167	.709	.0051
.250	.765	.0048
.417	.849	.0036
.584	.902	.0022
.750	.945	.0013
.834	.959	.0007
.917	.988	.0004
1.0	1.00	.000
	70 - 70 - P	
.057	.556	.0202
.095	.702	.0195
.238	.802	.0161
.381	.871	.0088
.523	.907	.0058
.666	.944	.0044
.809	.969	.0020
.904	.985	.0010
1.00	1.00	.0
	30 - 90 - P	
.06	.417	.0219
.10	.537	.0217
.20	.698	.0160
.30	.772	.0166
.40	.830	.0109
.50	.881	.0084
.60	.920	.0071
.70	.957	.0048
.80	.978	.0019
.90	.990	.0013
1.00	1.000	.000

Table I - cont.

z/δ	u/U	-v/U
	50 - 90 - P	
.049	.468	.0109
.081	.618	.0132
.203	.723	.0101
.326	.798	.0069
.447	.857	.0030
.569	.908	.0015
.692	.952	.00
.813	.976	.00
.935	.995	.00
1.00	1.00	.00
	90 - 90 - P	
.037	.551	.0296
.063	.691	.0305
.188	.789	.0238
.313	.844	.0151
.438	.888	.0076
.563	.922	.0035
.688	.954	.000
.813	.980	.00
.938	.991	.00
1.000	1.00	.00
	70 - 10 - S	
.046	.537	.0268
.062	.565	.0251
.077	.581	.0226
.115	.640	.0235
.154	.702	.0301
.231	.780	.0317
.309	.847	.0303
.385	.886	.0282
.538	.945	.0195
.692	.981	.0117
.846	.996	.0038
1.0	1.0	.0
	90 - 10 - S	
.032	.342	-.0103
.042	.370	-.0023
.079	.437	.0007
.132	.515	.0080
.211	.615	.0149
.316	.742	.0202
.473	.876	.0231
.631	.956	.0157
.789	.985	.0065
.947	.995	.0007
1.0	1.0	.0

z/δ	u/U	-v/U
	70 - 90 - P	
.042	.508	.0292
.070	.613	.0335
.176	.737	.0289
.282	.795	.0223
.387	.837	.0106
.493	.875	.0033
.598	.918	.0022
.704	.951	.0018
.810	.970	.0012
.915	.991	.0005
1.00	1.00	.0
	50 - 10 - S	
.055	.649	.0392
.073	.667	.0371
.091	.685	.0292
.136	.759	.0263
.182	.802	.0206
.273	.859	.0156
.364	.899	.0091
.455	.938	.0069
.545	.967	.0030
.637	.988	.0017
.818	.993	.0008
1.0	1.0	.0
	85 - 10 - S	
.035	.398	.0045
.047	.419	.0054
.071	.435	.0092
.088	.469	.0094
.118	.525	.0128
.177	.618	.0218
.235	.703	.0281
.353	.822	.0333
.471	.903	.0274
.588	.952	.0185
.706	.977	.0113
.823	.995	.0049
1.0	1.0	.0
	95 - 10 - S	
.027	.29	-.0051
.036	.317	-.0004
.068	.359	+.0048
.114	.415	.0091
.182	.503	.0162
.318	.682	.0271
.455	.829	.0317
.637	.945	.0223
.818	.988	.0095
1.0	1.0	.0

Table I - cont.

z/δ	u/U	-v/U
	50 - 30 - S	
.05	.50	.0065
.10	.65	.0074
.20	.76	.0064
.40	.86	.0041
.60	.92	.0016
.80	.97	.0005
1.0	1.0	.0
	70 - 30 - S	
.05	.42	.0118
.10	.56	.0129
.20	.67	.0104
.40	.80	.0053
.60	.90	.0027
.80	.97	.0008
1.0	1.0	.0
	85 - 30 - S	
.035	.265	.0162
.059	.365	.0194
.118	.472	.0190
.235	.608	.0128
.353	.732	.0167
.471	.814	.0127
.588	.885	.0
.706	.937	.0
.824	.975	.0
.942	.994	.0
1.00	1.00	.0
	90 - 30 - S	
.05	.380	.0374
.10	.436	.0353
.20	.537	.0290
.40	.730	.0170
.60	.877	.0068
.80	.967	.0019
1.0	1.0	.0
	50 - 40 - S	
.067	.650	.0204
.111	.722	.0184
.222	.808	.0108
.333	.857	.0045
.444	.904	.0
.556	.940	.0
.667	.969	.0
.778	.987	.0
.889	.997	.0
1.00	1.00	.0

z/δ	u/U	-v/U
	60 - 30 - S	
.063	.560	.0146
.105	.650	.0146
.210	.752	.0113
.368	.827	.0058
.526	.887	.0031
.656	.944	.0016
.840	.984	.0005
1.0	1.0	.00
	80 - 30 - S	
.041	.329	.0235
.069	.439	.0289
.207	.596	.0210
.344	.710	.0117
.483	.812	.0093
.621	.895	.0047
.759	.954	.0016
.896	.99	.0005
1.0	1.0	.00
	90 - 30 - S	
.029	.205	.0287
.048	.323	.0397
.143	.441	.0348
.238	.551	.0242
.333	.657	.0164
.428	.752	.0068
.523	.822	.0049
.618	.889	.0018
.714	.940	.0
.809	.970	.0
.905	.987	.0
1.00	1.00	.0
	95 - 30 - S	
.046	.130	-
.136	.273	.0532
.227	.404	.0340
.318	.516	.0206
.409	.637	.0165
.500	.721	.0137
.591	.805	.0040
.682	.883	.0
.773	.926	.0
.863	.970	.0
.954	.992	.0
1.00	1.00	.0

Table I - cont.

z/δ	u/U	-v/U
	70 - 40 - S	
.050	.479	.0225
.083	.598	.0247
.208	.723	.0195
.333	.805	.0139
.458	.873	.0094
.584	.925	.0048
.708	.963	.0
.833	.987	.0
.958	.998	.0
1.00	1.00	.0
	90 - 40 - S	
.032	.223	.0304
.053	.318	.0404
.158	.462	.0417
.263	.584	.0382
.368	.663	.0279
.474	.779	.0206
.579	.852	.0159
.684	.913	.0059
.789	.958	.0034
.894	.989	.0010
1.00	1.00	.0
	50 - 50 - S	
.05	.521	.0229
.10	.675	.0243
.20	.772	.0182
.40	.876	.0069
.60	.950	.0022
.80	.980	.0004
1.00	1.0	.0
	70 - 50 - S	
.05	.520	.0406
.10	.637	.0421
.20	.733	.0330
.40	.850	.0162
.60	.932	.0065
.80	.982	.0014
1.0	1.0	.0
	85 - 50 - S	
.036	.328	.0515
.061	.422	.0498
.121	.512	.0482
.212	.614	.0422
.303	.705	.0330
.394	.774	.0256
.485	.838	.0171
.576	.893	.0106
.667	.940	.0070
.758	.970	.0030
.848	.987	.0007
1.0	1.0	.0

z/δ	u/U	-v/U
	85 - 40 - S	
.036	.304	.0249
.061	.411	.0319
.182	.566	.0288
.303	.671	.0247
.424	.775	.0194
.546	.851	.0129
.667	.915	.0078
.788	.959	.0029
.909	.988	.0009
1.00	1.00	.0
	95 - 40 - S	
.049	.230	.0830
.146	.368	.0730
.244	.482	.0627
.341	.604	.0453
.439	.701	.0364
.537	.793	.0281
.634	.862	.0216
.731	.921	.0114
.829	.960	.0061
.927	.987	.0033
1.00	1.00	.0
	60 - 50 - S	
.05	.550	.0330
.10	.670	.0336
.20	.760	.0251
.40	.868	.0122
.60	.935	.0041
.80	.980	.0009
1.0	1.0	.0
	80 - 50 - S	
.05	.415	.0469
.10	.495	.0461
.20	.605	.0387
.40	.773	.0224
.60	.900	.0108
.80	.970	.0030
1.0	1.0	.0
	90 - 50 - S	
.033	.286	.0474
.056	.353	.0537
.111	.433	.0520
.222	.508	.0543
.333	.663	.0397
.444	.753	.0340
.556	.845	.0190
.667	.910	.0128
.778	.953	.0094
.889	.982	.0027
1.0	1.0	.0

Table I - cont.

z/δ	u/U	-v/U
	90 - 50 - S	
.05	.312	.0658
.10	.387	.0674
.20	.485	.0592
.40	.672	.0410
.60	.822	.0206
.80	.937	.0057
1.0	1.0	.0
	50 - 60 - S	
.086	.658	.0268
.157	.756	.0244
.286	.831	.0174
.428	.890	.0110
.572	.935	.0079
.715	.974	.0046
.857	.990	.0024
1.00	1.00	.0
	85 - 60 - S	
.040	.302	.0525
.067	.434	.0632
.167	.572	.0528
.267	.664	.0453
.367	.750	.0310
.467	.825	.0255
.567	.890	.0148
.667	.930	.0117
.777	.965	.0056
.867	.985	.0035
.933	.992	.0019
1.000	1.000	.0
	95 - 60 - S	
.053	.230	.0912
.158	.404	.0870
.263	.523	.0696
.369	.644	.0518
.474	.752	.0384
.579	.836	.0236
.684	.905	.0178
.842	.974	.0034
.948	.993	.0014
1.00	1.00	.0
	60 - 70 - S	
.057	.606	.0370
.095	.666	.0360
.238	.775	.0279
.334	.824	.0178
.428	.87	.0161
.524	.905	.0108
.619	.940	.0057
.714	.962	.0029
1.0	1.0	.00

z/δ	u/U	-v/U
	95 - 50 - S	
.030	.220	.0662
.050	.308	.0683
.150	.414	.0683
.250	.517	.0577
.350	.628	.0427
.450	.715	.0350
.550	.813	.0241
.650	.870	.0182
.750	.932	.0106
.850	.971	.0027
.950	.991	.0014
1.0	1.0	.0
	70 - 60 - S	
.055	.505	.0440
.091	.607	.0446
.227	.738	.0354
.364	.824	.0227
.500	.884	.0147
.637	.934	.0114
.772	.966	.0044
.909	.988	.0017
1.00	1.00	.0
	90 - 60 - S	
.036	.154	.0655
.060	.287	.0841
.180	.504	.0715
.299	.645	.0542
.419	.760	.0370
.539	.854	.0247
.658	.921	.0173
.778	.967	.0073
.904	.991	.0023
1.00	1.00	.0
	50 - 70 - S	
.05	.515	.0284
.10	.660	.0310
.20	.760	.0254
.40	.866	.0133
.60	.930	.0052
.80	.974	.0009
1.0	1.0	.00
	70 - 70 - S	
.05	.490	.0338
.10	.620	.0357
.20	.727	.0311
.40	.860	.0172
.60	.935	.0072
.80	.984	.0017
1.00	1.0	.00

Table I - cont.

z/δ	u/U	-v/U
	80 - 70 - S	
.045	.386	.0444
.074	.438	.0456
.185	.614	.0462
.296	.670	.0349
.407	.786	.0260
.518	.850	.0173
.630	.895	.0093
.740	.940	.0041
.85	.975	.0010
1.0	1.0	.00
	90 - 70 - S	
.035	.274	.0444
.059	.351	.0548
.177	.516	.0570
.294	.642	.0470
.412	.753	.0391
.529	.848	.0272
.647	.913	.0170
.765	.963	.0074
.882	.987	.0026
1.00	1.00	.00
	50 - 90 - S	
.075	.652	.0342
.137	.775	.0318
.250	.847	.0225
.375	.895	.0155
.500	.937	.0093
.625	.962	.0054
.750	.988	.0026
.875	.995	.0002
1.00	1.00	.00
	85 - 90 - S	
.048	.388	.0420
.080	.477	.0457
.240	.704	.0425
.400	.836	.0318
.600	.920	.0188
.761	.969	.0098
.921	.994	.0038
1.00	1.000	.00
	90 - 90 - S	
.045	.316	.0386
.076	.389	.0408
.227	.640	.0397
.379	.784	.0338
.531	.884	.0224
.682	.948	.0107
.834	.987	.0048
1.00	1.000	.00

z/δ	u/U	-v/U
	85 - 70 - S	
.040	.322	.0425
.067	.440	.0538
.200	.653	.0480
.333	.775	.0350
.467	.870	.0213
.600	.933	.0129
.733	.975	.0039
.867	.993	.0010
1.00	1.00	.00
	90 - 70 - S	
.05	.312	.0563
.10	.422	.0677
.20	.536	.0662
.40	.725	.0481
.60	.865	.0227
.80	.961	.0072
1.0	1.0	.00
	95 - 70 - S	
.032	.129	.0330
.053	.281	.0670
.158	.424	.0718
.263	.542	.0618
.369	.665	.0480
.474	.780	.0353
.579	.860	.0239
.684	.924	.0164
.789	.961	.0079
.895	.985	.0033
1.00	1.00	.00
	70 - 90 - S	
.055	.506	.0397
.091	.645	.0428
.227	.800	.0350
.364	.878	.0259
.500	.932	.0168
.637	.962	.0115
.773	.985	.0060
.909	.997	.0019
1.00	1.00	.00
	95 - 90 - S	
.043	.289	.0364
.071	.367	.0324
.214	.545	.0329
.357	.679	.0315
.500	.799	.0277
.643	.886	.0168
.786	.948	.0113
.928	.986	.0046
1.00	1.00	.00

TABLE II

Measured Main Flow, Boundary Layer and Model Quantities

Trav. Pos.	U_j ft/sec	U ft/sec	δ in.	β Inviscid degree	β Model degree	α Model degree	C_f Law of the wall
30-10-P	84.9	80.7	.110	11.7	13.2	-7.5	.0052
50-10-P	"	74.2	.130	17.7	16.4	-6.5	.0053
70-10-P	"	70.9	.160	23.3	42.4	-12.9	.0054
90-10-P	"	73.0	.170	28.5	50.2	-6.1	.0062
30-30-P	86.8	76.0	.065	8.4	8.3	-3.9	.0062
50-30-P	"	70.7	.085	12.3	8.8	-3.9	.0061
70-30-P	"	69.0	.105	15.6	17.1	-7.0	.0060
90-30-P	"	71.5	.120	18.6	19.6	-4.1	.0064
30-40-P	84.9	76.2	.060	5.2	5.7	-3.7	.0065
50-40-P	"	72.1	.087	8.2	8.6	-4.1	.0060
70-40-P	"	71.2	.112	11.5	11.4	-4.8	.0058
90-40-P	"	73.2	.135	14.3	17.7	-6.5	.0065
30-50-P	85.5	73.8	.060	3.1	3.2	-1.6	.0060
50-50-P	"	69.1	.080	5.4	6.1	-2.7	.0062
70-50-P	"	68.0	.105	7.8	13.0	-3.6	.0058
90-50-P	"	71.4	.125	10.4	17.3	-4.3	.0069
30-60-P	84.9	72.4	.065	1.3	1.6	-0.8	.0070
50-60-P	"	68.8	.102	3.0	4.3	-1.8	.0058
70-60-P	"	67.5	.123	5.1	8.5	-3.5	.0057
90-60-P	"	69.8	.140	7.5	14.4	-2.4	.0068
30-70-P	85.5	70.4	.060	-0.2	-1.5	1.2	.0064
50-70-P	"	66.7	.085	1.4	0.0	0.0	.0064
70-70-P	"	66.2	.105	3.2	6.5	-2.4	.0064
90-70-P	"	68.8	.120	5.4	6.2	-2.7	.0055
30-90-P	84.9	65.8	.100	-3.7	-4.4	2.8	.0068
50-90-P	"	61.8	.123	-2.6	2.1	-1.1	.0046
70-90-P	"	61.3	.142	-.8	5.7	-2.4	.0054
90-90-P	"	64.3	.160	1.1	6.8	-1.5	.0064
50-10-S	83.0	100.3	.110	-2.8	7.5	-4.1	.0055
70-10-S	"	93.5	.130	-1.1	11.9	-7.3	.0043
85-10-S	"	82.3	.170	0.9	9.2	-9.4	.0028
90-10-S	"	78.6	.190	1.7	6.5	-9.3	.0024
95-10-S	"	74.8	.220	2.5	7.5	-11.9	.0018
50-30-S	86.8	107.9	.067	1.6	1.9	0.4	.0054
60-30-S	"	101.0	.095	2.3	2.5	-1.2	.0050
70-30-S	"	96.4	.110	3.1	1.8	-1.2	.0036
80-30-S	"	87.0	.145	3.8	3.5	-3.6	.0028
85-30-S	86.3	82.8	.170	4.1	1.4	-1.5	.0023
90-30-S	"	79.2	.210	4.4	2.5	-3.5	.0018
90-30-S	86.8	83.4	.200	4.4	3.6	-3.7	.0021
95-30-S	86.3	75.6	.220	4.6	2.6	-8.6	.0008

Table II -cont.

Trav. Pos.	U_j ft/sec	U ft/sec	in.	β Inviscid degree	β Model degree	α Model degree	C_f Law of the wall
50-40-S	86.4	104.0	.090	3.3	1.5	-.7	.0058
70-40-S	"	94.9	.120	4.9	4.7	-2.7	.0042
85-40-S	"	84.5	.165	5.8	4.9	-4.5	.0025
90-40-S	"	81.0	.190	6.0	4.2	-5.3	.0019
95-40-S	"	78.2	.205	6.1	7.4	-14.2	.0014
50-50-S	86.8	105.1	.075	5.3	4.6	-1.5	.0056
60-50-S	"	100.8	.100	6.1	4.9	-1.8	.0052
70-50-S	"	95.4	.115	6.8	5.0	-2.3	.0047
80-50-S	"	89.2	.150	7.2	6.1	-3.3	.0030
85-50-S	84.8	83.3	.165	7.3	7.1	-6.5	.0028
90-50-S	"	80.5	.180	7.4	8.6	-10.4	.0022
90-50-S	86.8	82.5	.180	7.4	5.1	-6.9	.0020
95-50-S	84.8	77.6	.200	7.4	7.9	-12.0	.0018
50-60-S	84.1	100.3	.070	6.3	7.6	-3.1	.0061
70-60-S	"	92.0	.110	7.8	8.3	-3.8	.0045
85-60-S	"	82.5	.150	8.3	5.4	-4.4	.0028
90-60-S	"	79.4	.167	8.3	9.1	-13.0	.0018
95-60-S	"	76.0	.190	8.2	10.2	-18.6	.0014
50-70-S	86.8	101.2	.075	7.2	7.1	-1.9	.0054
60-70-S	"	97.2	.105	8.1	5.3	-2.3	.0053
70-70-S	"	92.5	.115	8.8	7.5	-2.9	.0042
80-70-S	"	84.5	.135	9.2	6.6	-4.6	.0032
85-70-S	84.2	80.4	.150	9.2	9.2	-7.2	.0028
90-70-S	"	76.7	.170	9.1	9.0	-10.8	.0022
90-70-S	86.8	81.1	.165	9.1	9.0	-11.7	.0022
95-70-S	84.2	73.6	.190	8.9	8.6	-13.1	.0018
50-90-S	84.2	93.1	.080	9.3	9.7	-4.6	.0061
70-90-S	"	86.8	.110	11.1	12.5	-6.3	.0050
85-90-S	"	77.4	.125	11.2	10.6	-8.2	.0033
90-90-S	"	74.0	.132	10.9	8.6	-10.4	.0025
95-90-S	"	70.3	.140	10.4	8.0	-9.9	.0023

Table II -cont.

Trav. Pos.	δ_x	θ_{xx}	δ_x^{**}	$-\delta_y^{*}$	$-\theta_{yx}$	θ_{yy}	R_θ
	in.	in.	in.	in.	in.	in.	
30-10-P	.0176	.0108	.0187	.00276	.00204	.00012	412
50-10-P	.0175	.0117	.0208	.00484	.00387	.00026	413
70-10-P	.0239	.0152	.0276	.00764	.00626	.00049	510
90-10-P	.0177	.0130	.0231	.00760	.00646	.00046	451
30-30-P	.0108	.0068	.0118	.00106	.00076	.00003	252
50-30-P	.0140	.0091	.0160	.00148	.00107	.00005	309
70-30-P	.0165	.0107	.0193	.00320	.00249	.00013	357
90-30-P	.0151	.0106	.0186	.00330	.00256	.00013	366
30-40-P	.0098	.0057	.0100	.00062	.00046	.00001	206
50-40-P	.0151	.0095	.0166	.00144	.00109	.00003	327
70-40-P	.0173	.0112	.0196	.00205	.00160	.00005	378
90-40-P	.0171	.0117	.0207	.00328	.00271	.00011	405
30-50-P	.0099	.0059	.0093	.00036	.00025	.00001	211
50-50-P	.0130	.0083	.0145	.00084	.00064	.00002	272
70-50-P	.0150	.0105	.0187	.00209	.00169	.00006	337
90-50-P	.0144	.0100	.0184	.00245	.00203	.00007	339
30-60-P	.0100	.0061	.0104	.00016	.00013	.00000	207
50-60-P	.0163	.0107	.0188	.00080	.00061	.00001	343
70-60-P	.0182	.0120	.0208	.00164	.00134	.00001	379
90-60-P	.0160	.0114	.0203	.00204	.00168	.00005	371
30-70-P	.0111	.0068	.0115	-.00016	-.00013	.00001	230
50-70-P	.0141	.0093	.0161	.00000	.00000	.00000	300
70-70-P	.0143	.0095	.0182	.00084	.00065	.00001	304
90-70-P	.0159	.0103	.0192	.00121	.00084	.00002	343
30-90-P	.0188	.0109	.0185	-.00095	-.00067	.00001	338
50-90-P	.0209	.0133	.0236	.00050	.00039	.00001	386
70-90-P	.0229	.0152	.0274	.00157	.00115	.00003	436
90-90-P	.0208	.0148	.0263	.00156	.00119	.00003	446
50-10-S	.0127	.0079	.0138	.00106	.00081	.00002	400
70-10-S	.0182	.0113	.0194	.00234	.00191	.00006	534
85-10-S	.0302	.0171	.0282	.00282	.00231	.00007	712
80-10-S	.0374	.0192	.0345	.00225	.00190	.00004	765
95-10-S	.0518	.0263	.0424	.00379	.00304	.00009	997
50-30-S	.0099	.0072	.0125	.00020	.00016	.00000	378
60-30-S	.0156	.0101	.0176	.00047	.00035	.00001	499
70-30-S	.0220	.0137	.0226	.00055	.00032	.00001	642
80-30-S	.0330	.0193	.0315	.00149	.00099	.00002	821
85-30-S	.0398	.0224	.0367	.00095	.00047	.00002	902
90-30-S	.0547	.0288	.0460	.00242	.00125	.00006	1111
90-30-S	.0525	.0302	.0440	.00294	.00171	.00008	1229
95-30-S	.0759	.0319	.0428	.00367	.00130	.00014	1174

Table II - cont.

Trav. Pos.	δ_x	θ_{xx}	δ_x^{**}	$-\delta_x^{*}$	$-\theta_{yx}$	θ_{yy}	R_θ
	in.	in.	in.	in.	in.		
50-40-S	.0115	.0075	.0134	.00041	.00029	.00001	380
70-40-S	.0198	.0125	.0216	.00109	.00081	.00002	577
85-40-S	.0381	.0222	.0365	.00250	.00162	.00006	917
90-40-S	.0502	.0268	.0432	.00333	.00177	.00013	1060
95-40-S	.0627	.0301	.0472	.00697	.00361	.00037	1150
50-50-S	.0107	.0073	.0121	.00056	,00043	.00001	377
60-50-S	.0144	.0101	.0168	.00113	.00085	.00002	496
70-50-S	.0188	.0124	.0205	.00182	.00133	.00004	612
80-50-S	.0314	.0193	.0316	.00287	.00184	.00008	842
85-50-S	.0353	.0203	.0342	.00346	.00222	.00011	824
90-50-S	.0453	.0251	.0408	.00500	.00317	.00025	985
90-50-S	.0507	.0268	.0448	.00467	.00222	.00025	1080
95-50-S	.0572	.0294	.0471	.00650	.00367	.00045	1110
50-60-S	.0095	.0062	.0109	.00077	.00062	.00002	306
70-60-S	.0179	.0117	.0205	.00187	.00133	.00006	526
85-60-S	.0320	.0188	.0316	.00377	.00244	.00015	756
90-60-S	.0423	.0218	.0354	.00563	.00329	.00031	847
95-50-S	.0551	.0269	.0424	.00743	.00387	.00048	1000
50-70-S	.0103	.0073	.0134	.00085	.00064	.00002	362
60-70-S	.0158	.0106	.0184	.00138	.00109	.00004	504
70-70-S	.0171	.0113	.0200	.00166	.00120	.00007	508
80-70-S	.0289	.0178	.0300	.00272	.00175	.00012	736
85-70-S	.0276	.0164	.0272	.00334	,00226	.00015	641
90-70-S	.0414	.0223	.0361	.00486	.00306	.00030	833
90-70-S	.0419	.0230	.0397	.00556	.00340	.00030	912
95-70-S	.0513	.0259	.0414	.00648	.00375	.00039	927
50-90-S	.0096	.0061	.0110	.00098	.00078	.00002	272
70-90-S	.0149	.0094	.0168	.00207	.00163	.00006	395
85-90-S	.0232	.0138	.0233	.00301	.00219	.00010	515
90-90-S	.0285	.0151	.0257	.00294	.00204	.00010	540
95-90-S	.0368	.0197	.0323	.00360	.00247	.00009	668

APPENDIX A

Description of Boundary Layer Integral Equations

The Navier-Stokes equation and the continuity equation for a viscous incompressible fluid are:

$$\frac{D\bar{Q}}{Dt} = \frac{1}{\rho}\nabla p + \nu \nabla^2 \bar{Q} \tag{A-1}$$

$$\nabla \cdot \bar{Q} = 0 \tag{A-2}$$

where $\bar{Q}$ is the absolute velocity and $\frac{D}{Dt}$ denotes the substantial derivative. In a system steadily rotating with a constant angular velocity ω, the equations of motion become:

$$\bar{q}\cdot\nabla\bar{q} + (\bar{\omega}\cdot\bar{r})\bar{\omega} + 2(\bar{\omega}\times\bar{q}) - \omega^2\bar{r} = -\frac{1}{\rho}\nabla p - \nu\nabla^2\bar{q} \tag{A-3}$$

$$\nabla\cdot\bar{q} = 0 \tag{A-4}$$

where $\bar{q} = \bar{Q} - \bar{\omega} \times \bar{r}$ is the velocity relative to the blade surface. We now transform these equations into the curvilinear coordinate system x, y, z shown in Fig. 2. The transformation formulas are:

$$\begin{aligned} X &= \int_o^x \cos K \cos\psi \, dx - z \sin\psi - y \sin K \cos\psi + X_s \\ Y &= \int_o^x \sin K \, dx + y \cos K + Y_s \\ Z &= \int_o^x \cos K \sin\psi \, dx + z \cos\psi - y \sin K \sin\psi + Z_s \end{aligned} \tag{A-5}$$

where K and ψ are functions of x and subscript s indicates coordinate at stagnation point. The components of $\bar{r}$, $\bar{\omega}$ and $\bar{q}$ are:

$$\begin{aligned} \bar{r} &= (x - d',\ y + R,\ z) \\ \bar{\omega} &= (\omega \sin\psi \cos K,\ \omega \sin\psi \sin K,\ \omega \cos\psi) \\ \bar{q} &= (u,\ v,\ w) \end{aligned} \tag{A-6}$$

where R is the radius to the stagnation point of the streamline we are considering and d' is the distance along the x-coordinate corresponding to the distance d along the X-coordinate.

The square of the element of arc ds in cartesian coordinates has the form

$$ds^2 = dX^2 + dY^2 + dZ^2 \tag{A-7}$$

and in orthogonal curvilinear coordinates

$$ds^2 = h_1^2\, dx^2 + h_2^2\, dy^2 + h_3^2\, dz^2 \qquad \text{(A-8)}$$

Equating gives

$$h_1 = 1 - ym;\ h_2 = 1;\ h_3 = 1 \qquad \text{(A-9)}$$

where $m = \frac{dK}{dx}$ and terms of order (δ^2) have been neglected in h_1. When finding the square of the elements in equation (A-7) we also get terms with dxdy, dxdz and dydz. However, if the coordinate system x, y, z is orthogonal the coefficients for these terms will be zero. This is only true for the dydz term in our coordinate system, but the term for dxdz is $-ye\sin K$ and for dxdy is $ez\sin K$, where $e = \frac{d\psi}{dx}$. If we now use the equations going along one streamline at a time we can put $y = 0$ which makes the coefficient for dxdz zero. The coefficient for dxdy, however, can not be made zero, but z is small of order (δ) and restricting the equations to cases where the radius of curvature of the surface is large compared to the boundary layer thickness we have e of order $(\frac{\delta}{c^2})$. Thus $ez\sin K$ is of order $(\frac{\delta^2}{c^2})$ so the coordinate system will be very nearly orthogonal and is certainly justified to use with the boundary layer equations.

In curvelinear coordinates the various derivative operators appearing in the equations of motion have the following form:

$$(\bar{q}\cdot\nabla\bar{q})_x = \frac{1}{h_1}\left[u\frac{\partial u}{\partial x} + v\frac{\partial v}{\partial x} + w\frac{\partial w}{\partial x}\right] - \frac{v}{h_1 h_2}\left[\frac{\partial (h_2 v)}{\partial x} - \frac{\partial (h_1 u)}{\partial y}\right] + \frac{w}{h_3 h_1}\left[\frac{\partial (h_1 u)}{\partial z} - \frac{\partial (h_3 w)}{\partial x}\right]$$

$$(\nabla p)_x = \frac{1}{h_1}\frac{\partial p}{\partial x}$$

$$(\nabla^2 \bar{q})_x = (\nabla\nabla\cdot\bar{q})_x - [\nabla\times(\nabla\times\bar{q})]_x$$

where

$$(\nabla\nabla\cdot\bar{q})_x = \frac{1}{h_1}\frac{\partial}{\partial x}(\nabla\cdot\bar{q})$$

$$[\nabla\times(\nabla\times\bar{q})]_x = \frac{1}{h_2 h_3}\left[\frac{\partial}{\partial y} h_3 (\nabla\times\bar{q})_z - \frac{\partial}{\partial z} h_2 (\nabla\times\bar{q})_y\right]$$

$$(\nabla \times \bar{q})_x = \frac{1}{h_2 h_3}\left[\frac{\partial}{\partial y}(h_3 w) - \frac{\partial}{\partial z}(h_2 v)\right]$$

$$\nabla \cdot \bar{q} = \frac{1}{h_1 h_2 h_3}\left[\frac{\partial}{\partial x}(h_2 h_3 u) + \frac{\partial}{\partial y}(h_3 h_1 v) + \frac{\partial}{\partial z}(h_2 h_1 w)\right]$$

where subscript x denotes x-component.

Denoting differentiation of u, v, w and p with respect to x, y, z, with subscripts x, y and z respectively, we get for the Navier-Stokes equation

x-component

$$\frac{uu_x}{1-ym} + vu_y + wu_z - \frac{vum}{1-ym} + \omega^2[(x-d')\sin^2\psi\cos^2\kappa + (R+y)\sin^2\psi\sin\kappa\cos\kappa + z\cos\psi\sin\psi\cos\kappa] + 2\omega(w\sin\psi\sin\kappa - v\cos\psi) - \omega^2(x-d') = -\frac{p_x}{\rho(1-ym)} + \nu\left[\frac{u_{xx}}{(1-ym)^2} + u_{yy} + u_{zz} + \frac{ym_x u_x}{(1-ym)^3} - \frac{mu_y}{1-ym} - \frac{um^2}{(1-ym)^2} - \frac{vm_x}{(1-ym)^3} - \frac{2mv_x}{(1-ym)^2}\right] \quad \text{(A-9)}$$

y-component

$$\frac{uv_x}{1-ym} + vv_y + wv_z + \frac{u^2 m}{1-ym} + \omega^2[(x-d')\sin^2\psi\sin\kappa\cos\kappa + (R+y)\sin^2\psi\sin^2\kappa + z\cos\psi\sin\psi\sin\kappa] + 2\omega(u\cos\psi - w\sin\psi\cos\kappa) - \omega^2(R+y) = -\frac{p_y}{\rho} + \nu\left[\frac{v_{xx}}{(1-ym)^2} + v_{yy} + v_{zz} + \frac{ym_x v_x}{(1-ym)^3} - \frac{mv_y}{(1-ym)} - \frac{vm^2}{(1-ym)^2} + \frac{um_x}{(1-ym)^3} + \frac{2mu_x}{(1-ym)^2}\right] \quad \text{(A-10)}$$

z-component

$$\frac{uw_x}{1-ym} + vw_y + ww_z + \omega^2[(x-d')\sin\psi\cos\psi\cos\kappa + (R+y)\sin\psi\cos\psi\sin\kappa + z\cos^2\psi] + 2\omega(v\sin\psi\cos\kappa - u\sin\psi\sin\kappa) - \omega^2 z = -\frac{p_z}{\rho} + \nu\left[\frac{w_{xx}}{(1-ym)^2} + w_{yy} + w_{zz} + \frac{ym_x w_x}{(1-ym)^3} - \frac{mw_y}{1-ym}\right] \quad \text{(A-11)}$$

continuity equation

$$\frac{u_x}{1-ym} + v_y + w_z - \frac{vm}{1-ym} = 0 \quad \text{(A-12)}$$

Now introducing the usual boundary layer assumption that $\frac{\delta}{c} = O\left(\sqrt{\frac{\nu}{cU}}\right)$; $\frac{z}{c} = O\left(\frac{\delta}{c}\right)$; $\frac{w}{U} = O\left(\frac{\delta}{c}\right)$ and also put $y = 0$, we get the boundary layer equationsvalid for Reynolds number of the order $\left[\frac{1}{(\delta/c)^2}\right]$

Momentum equation

x-component

$$uu_x+vu_y+wu_z-vum-2\omega v\cos\psi+\omega^2\left[(x-d')(\sin^2\psi\cos^2K-1)+R\sin^2\psi\sin K\cos K\right]=-\frac{P_x}{\rho}+\nu u_{zz} \tag{A-13}$$

y-component

$$uv_x+vv_y+wv_z+u^2m+2\omega u\cos\psi+\omega^2\left[(x-d')\sin^2\psi\sin K\cos K+R(\sin^2\psi\sin^2K-1)\right]=\frac{P_y}{\rho}+\nu v_{zz} \tag{A-14}$$

z-component

$$2\omega(v\sin\psi\cos K-u\sin\psi\sin K)+\omega^2\sin\psi\cos\psi\left[(x-d')\cos K+R\sin K\right]=-\frac{P_z}{\rho} \tag{A-15}$$

Continuity equation

$$u_x+v_y+w_z-vm=0 \tag{A-16}$$

Equation (A-15) shows that $\frac{P_z}{\rho U_\infty^2/c}$ may be of the order $[1]$, but that only indicates a change of pressure across the boundary layer of the order $\left[\frac{\delta}{c}\right]$. Hence, we can approximate the pressure at the surface with the free-stream pressure. Equation (A-15) can now be disregarded.

In order to obtain the boundary layer momentum-integral equations, equations (A-13) and (A-14) are integrated with respect to z through the boundary layer to some constant height h such that $h>\delta$.

As we have neglected the variation of p across the boundary layer, we can get expression for p_x and p_y from the flow outside of the boundary layer where we may neglect the viscous terms. Equations (A-13) and (A-14), written for this region, become:

$$Uu_x+\omega^2\left[(x-d')(\sin^2\psi\cos^2K-1)+R\sin^2\psi\sin K\cos K\right]=-\frac{P_x}{\rho} \tag{A-17}$$

$$U^2m+2\omega U\cos\psi+\omega^2\left[(x-d')\sin^2\psi\sin K\cos K+R(\sin^2\psi\sin^2K-1)\right]=-\frac{P_y}{\rho} \tag{A-18}$$

Substituting equations (A-17) and (A-18) in (A-13) and (A-14) and also using the continuity equation to express w, the integration gives us the momentum integral equations.

x-direction

$$\frac{\partial \bar{\theta}_{xx}}{\partial x} + \frac{\partial \bar{\theta}_{xy}}{\partial y} + \frac{1}{\bar{U}}\frac{\partial \bar{U}}{\partial x}(\bar{\delta}_x^* + 2\bar{\theta}_{xx}) - \left(\frac{1}{\bar{U}}\frac{\partial \bar{U}}{\partial y} - m\right)(\bar{\delta}_y^* - 2\bar{\theta}_{xy}) + \frac{2\omega_\perp}{\bar{U}}\bar{\delta}_y^* = \frac{C_f}{2} \qquad \text{(A-19)}$$

y-direction

$$\frac{\partial \bar{\theta}_{yx}}{\partial x} + \frac{2\bar{\theta}_{xy}}{\bar{U}}\frac{\partial \bar{U}}{\partial x} + \frac{\partial \bar{\theta}_{yy}}{\partial y} + \bar{\theta}_{yy}\left(\frac{2}{\bar{U}}\frac{\partial \bar{U}}{\partial y} - m\right) - m(\bar{\theta}_{xx} + \bar{\delta}_x^*) - \frac{2\omega_\perp}{\bar{U}}\bar{\delta}_x^* = \frac{C_f}{2}\tan\alpha \qquad \text{(A-20)}$$

where the integrated quantities of the boundary layer defined in equation (1.3-1) are used and $\omega_\perp = \omega\cos\psi$ is the component of the angular velocity perpendicular to the surface. The dashes over the quantities refer to the curvilinear coordinate system. We also form an energy integral equation by multiplying equations (A-13) by u and integrate through the boundary layer to get

$$\frac{1}{\bar{U}}\frac{\partial}{\partial x}(\bar{U}^3\bar{\delta}_x^{**}) + \frac{\partial \bar{\delta}_y^{**}}{\partial y} + \frac{2\omega_\perp}{\bar{U}}(3\bar{\delta}_y^{**} - 2\bar{\theta}_{xy}) = \frac{2(d+t)}{\rho\bar{U}^3} \qquad \text{(A-21)}$$

where

$$\frac{d+t}{\rho} = \int_0^\delta \nu\left(\frac{\partial u}{\partial z}\right)^2 dz$$

and the irrotationality condition equation (1.3-4) has been used.

The curvilinear coordinate system we have been using has the disadvantage of not being a "streamline" coordinate system more than on the base streamline. This means that the equations do not take care of streamline convergence or divergence in the main stream. We nowwill correct for this, following Johnston (Ref. 12)

We first must determine the relationships between velocity components and their derivatives for the curvilinear system and the "streamline" system.

Sketched below is a diagram showing the relationship between the various velocity components at a point P, a distance y from the base line.

$\bar{U} \perp \bar{V}$

$u \perp v$

$\bar{u} \perp \bar{v}$

$u \parallel U$

$\bar{u} \parallel \bar{U}$

$\bar{U} \perp y$

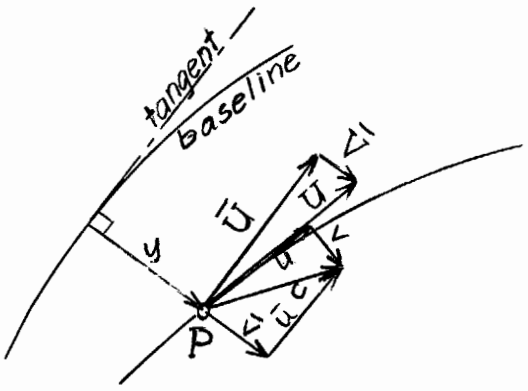

The arrow marked U represents the main flow total velocity vector, that marked c is the total velocity vector in the boundary layer.

From the sketch, the following relationships among the components are deduced.

$$U^2 = \bar{U}^2 + \bar{V}^2$$

$$vU = \bar{v}\,\bar{U} - \bar{u}\,\bar{V} \qquad \text{(A-22)}$$

$$uU = \bar{u}\bar{U} + \bar{v}\bar{V}$$

From the relations (A-22) and the fact that the base line (y = 0) corresponds to a main flow streamline, it can be demonstrated that <u>on the base line</u>:

$$\bar{V} = 0;\ \bar{U} = U;\ \bar{v} = v;\ \bar{u} = u;\ d\bar{U} = dU;\ \frac{\partial \bar{V}}{\partial x} = 0$$

$$\frac{\partial \bar{u}}{\partial x} = \frac{\partial u}{\partial x};\ \frac{\partial \bar{v}}{\partial x} = \frac{\partial v}{\partial x};\ \frac{\partial \bar{u}}{\partial y} = \frac{\partial u}{\partial y} - \frac{v}{\bar{U}}\frac{\partial \bar{V}}{\partial y};\ \frac{\partial \bar{v}}{\partial y} = \frac{\partial v}{\partial y} + \frac{u}{\bar{U}}\frac{\partial \bar{V}}{\partial y}; \qquad \text{(A-23)}$$

With the transformations (A-23) we may convert the integrated quantities of the boundary layer and their deviations from the definition in the curvelinear system to the definitions in the "streamline" system. For example, <u>on the base line</u>.

$$\bar{\theta}_{xy} = \frac{1}{\bar{U}^2}\int_0^\infty (\bar{U}-\bar{u})\bar{v}\,dz = \frac{1}{U^2}\int_0^\infty (U-u)v\,dz = \theta_{xy}$$

and

$$\frac{\partial \bar{\epsilon}_{xy}}{\partial y} = -\frac{2}{\bar{U}^3}\frac{\partial \bar{U}}{\partial y}\int_0^\infty (\bar{U}-\bar{u})\bar{v}\,dz + \frac{1}{\bar{U}^2}\int_0^\infty \bar{v}\left(\frac{\partial \bar{U}}{\partial y} - \frac{\partial \bar{u}}{\partial y}\right)dz + \frac{1}{\bar{U}^2}\int_0^\infty (\bar{U}-\bar{u})\frac{\partial \bar{V}}{\partial y}\,dz$$

using (A-23) this can be written

$$\frac{\partial \bar{\theta}_{xy}}{\partial y} = -\frac{2}{U^3}\frac{\partial U}{\partial y}\int_0^\infty (U-u)v\,dz + \frac{1}{U^2}\int_0^\infty v\left(\frac{\partial U}{\partial y} - \frac{\partial u}{\partial y} + \frac{v}{U}\frac{\partial \bar{V}}{\partial y}\right)dz + \frac{1}{U^2}\int_0^\infty (U-u)\left(\frac{\partial v}{\partial y} + \frac{u}{U}\frac{\partial \bar{V}}{\partial y}\right)dz$$

$$\frac{\partial \bar{\theta}_{xy}}{\partial y} = \frac{\partial \theta_{xy}}{\partial y} + \frac{1}{U}\frac{\partial \bar{V}}{\partial y}\left\{\frac{1}{U^2}\int_0^\infty v^2\,dz + \frac{1}{U^2}\int_0^\infty (U-u)u\,dz\right\}$$

Using the definition (1.3-1) we can write this

$$\frac{\partial \bar{\theta}_{xy}}{\partial y} = \frac{\partial \theta_{xy}}{\partial y} + \frac{1}{U}\frac{\partial \bar{V}}{\partial y}(\theta_{yy} + \theta_{xx})$$

By performing similar operations on all the integral terms, we obtain the following relations on the base line.

$$\left.\begin{array}{l} \bar{\delta}_x^* = \delta_x^*;\ \bar{\delta}_y^* = \delta_y^*;\ \bar{\theta}_{xx} = \theta_{xx};\ \bar{\theta}_{yy} = \theta_{yy};\ \bar{\delta}_x^{**} = \delta_x^{**};\ \bar{\delta}_y^{**} = \delta_y^{**}; \\ \bar{\theta}_{xy} = \theta_{xy};\ \bar{\theta}_{yx} = \theta_{yx};\ \dfrac{\partial \bar{\theta}_{xx}}{\partial x} = \dfrac{\partial \theta_{xx}}{\partial x};\ \dfrac{\partial \bar{\theta}_{yx}}{\partial x} = \dfrac{\partial \theta_{yx}}{\partial x};\ \dfrac{\partial \bar{\delta}_x^{**}}{\partial x} = \dfrac{\partial \delta_x^{**}}{\partial x}; \\ \dfrac{\partial \bar{\theta}_{xy}}{\partial y} = \dfrac{\partial \theta_{xy}}{\partial y} + \dfrac{1}{U}\dfrac{\partial \bar{V}}{\partial y}(\theta_{yy}+\theta_{xx});\ \dfrac{\partial \bar{\theta}_{yy}}{\partial y} = \dfrac{\partial \theta_{yy}}{\partial y} + \dfrac{2}{U}\dfrac{\partial \bar{V}}{\partial y}\theta_{yy};\ \dfrac{\partial \bar{\delta}_y^{**}}{\partial y} = \dfrac{\partial \delta_y^{**}}{\partial y} - \dfrac{1}{U}\dfrac{\partial \bar{V}}{\partial y}(\delta_x^{**} + 2\delta_{xy}^{**}) \end{array}\right\} \quad \text{(A-24)}$$

In the last quantity $\delta_{xy}^{**} + \frac{1}{U^3}\int_0^\infty uv^2\,dz$: As v in the cases we consider is a magnitude smaller than u, $\delta_{xy}^{**} \ll \delta_x^{**}$ and $\theta_{yy} \ll \theta_{xx}$.

Now, by using the transformations of relations (A-23) and (A-24) the momentum integral equations along the base line of the streamline coordinate system becomes:

x-direction

$$\frac{\partial \theta_{xx}}{\partial x} + \frac{\partial \theta_{xy}}{\partial y} + \frac{1}{U}\frac{\partial U}{\partial x}(\delta_x^* + 2\theta_{xx}) - \left(\frac{1}{U}\frac{\partial U}{\partial y} - m\right)(\delta_y^* + 2\theta_{xy}) + \frac{1}{U}\frac{\partial \bar{V}}{\partial y}\theta_{xx} + \frac{2\omega_1}{U}\delta_y^* = \frac{C_f}{2} \quad \text{(A-25)}$$

y-direction

$$\frac{\partial \theta_{yx}}{\partial x} + 2\theta_{yx}\left(\frac{1}{U}\frac{\partial U}{\partial x} + \frac{1}{U}\frac{\partial \bar{V}}{\partial y}\right) + \frac{\partial \theta_{yy}}{\partial y} + \theta_{yy}\left(\frac{2}{U}\frac{\partial U}{\partial y} - m\right) - m(\theta_{xx} + \delta_x^*) - \frac{2\omega_1}{U}\delta_x^* = \frac{C_f}{2}\tan\alpha \quad \text{(A-26)}$$

Similarly the energy equation

$$\frac{1}{U^3}\frac{\partial}{\partial x}(U^3\delta_x^{**}) + \frac{\partial \delta_y^{**}}{\partial y} + \frac{1}{U}\frac{\partial \bar{V}}{\partial y}\delta_x^{**} + \frac{2\omega_1}{U}(3\delta_y^{**} - 2\theta_{xy}) = \frac{2(d+t)}{\rho U^3} \quad \text{(A-27)}$$

APPENDIX B

Construction and Features of Test Apparatus and Air Supply

The blades in the annular cascade are of typical compressor design with:

Circular arc camber line

NACA Four Digit Series thickness distribution with 9% maximum thickness

Chord; $c = 2.8"$

Camber angle - 35°

Pitch-chord ratio at mid-span $\frac{s}{c} = 1.0$

Aspect ratio $\frac{\ell}{c} = 1.8$

Diameter ratio $\frac{D_i}{D_y} = 0.65$

The end walls of the cascade were made of perforated sheet metal having 40% opening covered with a thin nylon cloth.

The inlet section between the vanes and the blades was designed for potential flow. In order to keep the boundary layer on the walls thin, the flow was continuously accelerated. The inner piece of this section was made of wood while the outer wall consists of sheet metal cones joined by a truck tire inner tube having a cross-section radius of approximately 6 inches.

The vanes were made of sheet metal. The stationary part was 15 inches long and the variable outlet section 2.5 inches. Between the stationary and variable sections was a screen, which together with another one further upstream, improved the uniformness of the flow.

The ventilating fan used to blow the air was a single stage axial machine having a nominal rating of 8000 cfm at three inches of water pressure rise. The inside fan casing diameter was 27 inches.

The fan casing was continued with another cylindrical shell of 27 inches diameter, which on one end had holes taken up in the periphery to al-

low the flow to go out radially to the specially designed sheet metal housing, holding the vanes.

The inlet section of the fan was of the radial type, using a truck tire inner tube and having a screen around the circumferential opening.

For the suction, two centrifugal type fans were used (Make: Buffalo Forge Co. - Type "R" - size 34).

APPENDIX C

Instrumentation and Uncertainty

Five-hole Free-stream Direction Probe (Figure 7)

This probe measures total pressure, pitch angle, δ, and yaw angle, ψ. Diameter of probe tip D = .13". Diameter of holes d = .014. The probe was initially calibrated for pitch angle δ when the yaw angle ψ = 0. However, for the upstream stations it was not always possible to pivot the probe so that ψ = 0 or $(p_2 - p_4) = 0$. A set of calibration curves was, therefore, taken for $-10° < \psi < 10°$. The total pressure reading was also affected by the pitch and yaw angles and a calibration curve giving the error in total pressure as a function of yaw and pitch angles was found. This error is proportional to approximately the square of these angles. The calibration curves were reproducable to $\pm.4°$ in δ and ψ. However, taking into account errors introduced by the traversing rig, where part of the yaw angle has to be read on the protractor (Fig. 5), we have judged the error to be of the order $\pm1.0°$ for ψ and $\pm0.7°$ for δ. The five-hole direction probe is described on page 108 of Reference 26.

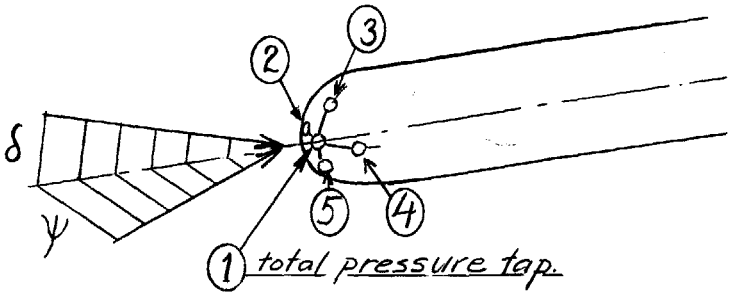

In order to get the static pressure in the free-stream, readings were taken from static pressure taps in the stem of a probe of the same configuration as just described. No correction was applied to the readings, but in the exit plane the pressures were also measured with a sphere-static probe (Ref. 25). The difference in readings were of the same order as the error of the later probe (±1%).

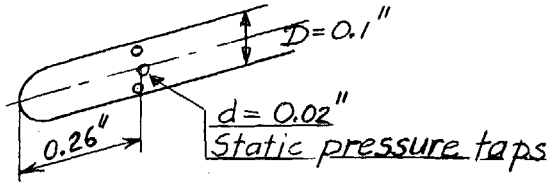

Three-hole Free-stream Cobra Probe

The five-hole probe just described was not accurate enough to find the streamline curvature outside of the boundary layer. Two probes were therefore constructed which could be slid along the chord direction of a blade, one for the suction side (shown in Fig. 6) and one for the pressure side. These probes give the angle between a free streamline and the chord direction as accurately as it was possible to calibrate the probe tip. The reproducability of the calibration was within ± 0.3 degrees.

The probe tip shown in the figure here had a standard tip made of three 0.025" stainless steel hypodermic tubing soldered together with the outer two cut off at a 60° included angle for measuring yaw.

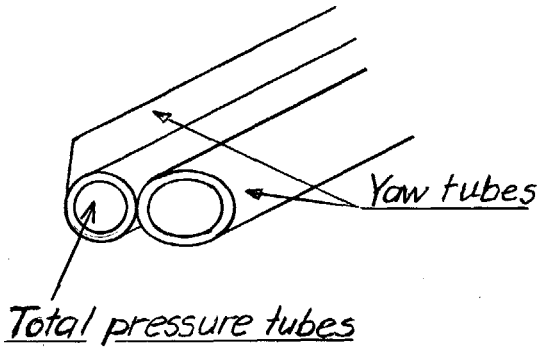

These probe tips were soldered to shoes which could be slid in 0.018" wide slots, milled along the chord direction of one blade. The shoes fit exactly in the slots and needed just to be pressed into the slots to hold the probes during the runs. When soldering the probe tips to the shoes, we were careful to line up the probes with the direction of the slots. The distance between the center of the tip and the wall was 0.23" on the suction side probe and 0.16" on the pressure side probe. These distances were chosen so that the tip always should be outside of the boundary layer.

Boundary Layer Traversing Probe

This probe was also of the cobra-type, but in order to get readings as close to the wall as possible, the probe tip had to be as small as possible. The requirements for this probe were:

1) Distance between center of probe tip to wall must be minimum.

2) Distance between centers of yaw holes must be minimum

3) The probe must give reasonable short response time.

4) Accurate traversing of the probe across the boundary layer must be possible.

We found that with an inside diameter of the hypodermic tubing of 0.008" we get a response time of 10-20 seconds which we considered reasonable. With this inside diameter, the outside one is given as 0.016", which was considered too large. We, therefore, tried to flatten the tubing in order to meet requirement (1). This naturally increased the distance between the yaw holes and pointed out the importance of requirement (2).

When using a probe in a shear flow, as shown in this figure, we have to worry about the errors introduced by the velocity gradient. One error depends on the difference between the effective and geometric center of the probe. This error has been considered in Reference (27) and was found to be negligible for turbulent flow. The other error we have to consider has to do with the yaw pressure difference and is dependent on misalignment of the probe. If the probe is not maintained exactly parallel to the surface, as shown in the figure , the two yaw holes will be exposed to differenct total pressure and this will show up as a yaw pressure difference. It was found that this error could be very large close to the wall where the velocity gradient is very steep. Thus, minimizing the distance between the yaw holes is necessary to keep this error small, so the flattened tubing could not be used. We further must have a traversing mechanism which keeps the probe parallel to the wall.

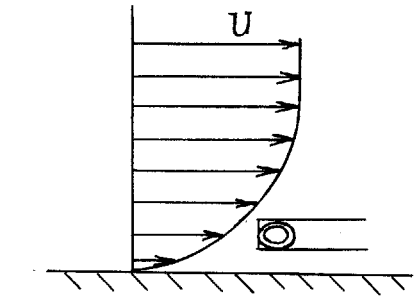

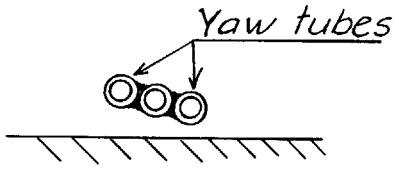

Several different configurations of the traversing mechanism were tried out and it was found that, besides the requirement of keeping the probe para-

llel to the wall, we had to support the probe as close to the tip as possible in order to minimize vibrations in the probe-tip. This resulted in the design shown on Figure 8. The probe in place on the blade is shown in Figure 5.

The probe tip, (1) in the figure here was made of three stainless steel hypodermic tubings with an inside diameter of 0.008" and the outside diameter ground down to 0.012". To the probe (1) was soldered two bent pieces of 0.042" stainless steel hypodermic tubing (2) through which two pieces of 0.020" piano wire (3) could be slid with the help of the micrometer shown in Figure 8. The ends of the piano wire rested against the blade surface and when sliding the piano wires back and forth the probe-tip was traversed across the boundary layer. The support points were in line with the probe-tip and 0.3" on each side of it. It is believed that this was not sufficiently close to cause appreciable error in the probe reading. Due to the supports on each side of the probe-tip it was possible to adjust the face of the tip under the microscope so it travelled parallel to the surface. The probe was calibrated in a uniform stream. In order to find the error in a shear flow we traversed the probe across the boundary layer several times at the same position and observed the reproducability of the readings. In the outer 80% of the boundary layer the yaw readings could be reproduced to within ±0.3 degrees while the readings closer to the wall might have errors up to ±1 degree.

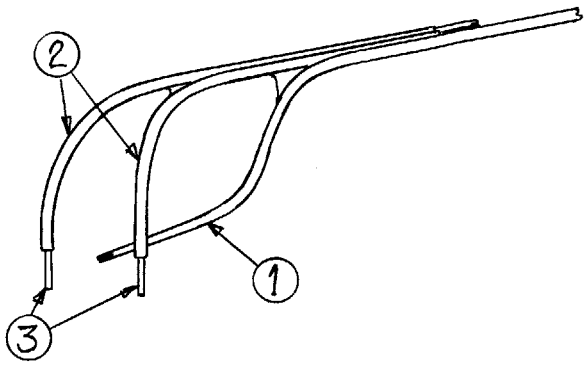

All traverses were made starting with the probe resting against the surface. As the gradient of total pressure was very steep here, it was easy to see when the probe left the surface and, thus, fix the starting value on the micrometer.

Static Pressure Readings

Two blades had eighteen 0.018" static pressure holes drilled perpendicular to the surface along a chord-direction. One had the holes on the pressure side, the other on the suction side. The pressure taps were connected with the measuring instruments through tubing inside the blades. By sliding the blades along the radial direction the pressure distribution at any span-position could be found.

Tripping Wires

Each blade in the cascade was fitted with tripping wires. The diameter of the wires were chosen from the criterion

$$\frac{U_o d}{\nu} > 600$$

taken from Reference 37, page 463. This gives a diameter of 0.014". The wires were glued to the surfaces at 10% chord on the pressure side and 30% chord on the suction side.

Traversing Rig to Hold the Probes

The rig shown in Figure 5 was fastened directly to the floor in order not to transfer any vibrations from the apparatus to the probes. Motion was provided in the axial and tangential directions and the probes could also be pivoted around a radial direction.

Pressure Measuring Equipment

All pressures were registered by Pressure Transducers manufactured by Statham Laboratories, Inc., Los Angeles, Calif. and were read on a Dynisco four-channel calibrator. The transducer-calibrator combination was calibrated against a regular micro-manometer having an uncertainty of approximately ± 0.001 inches of H_2O. From the reproducability of the calibration it was concluded that the uncertainty of the transducer-calibrator was well within ± 0.01 inches of H_2O.

Our principal measurements were $\frac{u}{U}$ and $\frac{v}{U}$. From the above we can figure the uncertainty in $\frac{u}{U}$ to be ± 1.5 percent while $\frac{v}{U}$ due to the lar-

ger uncertainty in the yaw-angle may have an error of ±10 percent.

These errors will also be present in the integrated quantities. Also, including the Reynolds number variation of ±3%, indicated in paragraph (2.3) we get ±4% error for integrated quantities in stream direction and ±10-15% in cross direction. In cases of very small cross-flow, the last error may be still larger.

APPENDIX D

Inviscid Theory

The purpose of this appendix is to show how the velocity parameter β can be related to the free-stream parameters.

In the outer portion of the turbulent boundary layer we expect the viscous terms to be small, so we may use the equations of motion with $\nu = 0$. Furthermore, due to our choice of coordinate system we know that the cross-flow velocities have to be small as they are zero just outside the boundary layer. Thus, we may assume the cross-flow velocity $\frac{V}{U}$ to be of the order $\left[\frac{\delta}{c}\right]$, which also gives the angle K to be of the order $\left[\frac{\delta}{c}\right]$.

Now, neglecting terms of the same order of magnitude as we did in deriving the boundary layer equations (A-13) and (A-14), we can rewrite those equations as

$$uu_x + wu_z + \omega^2(x-d')\cos^2\psi = -\frac{p_x}{\rho} \qquad \text{(D-1)}$$

$$uv_x + wv_z + u^2 m + 2\omega u\cos\psi + \omega^2\left[(x-d')\sin^2\psi \sin K - R\right] = -\frac{p_x}{\rho} \qquad \text{(D-2)}$$

where subscripts x, y z denote differentiation with respect to x, y, z respectively.

For the flow outside the boundary layer these equations become:

$$UU_x + \omega^2(x-d')\cos^2\psi = -\frac{p_y}{\rho} \qquad \text{(D-3)}$$

$$U^2 m + 2\omega U\cos\psi + \omega^2\left[(x-d')\sin^2\psi \sin K - R\right] = -\frac{p_y}{\rho} \qquad \text{(D-4)}$$

Substituting $\frac{p_x}{\rho}$ and $\frac{p_y}{\rho}$ from equations (D-3) and (D-4) into (D-1) and (D-2) gives

$$uu_x - UU_x + wu_z = 0 \qquad \text{(D-5)}$$

$$uv_x + wv_z + m(u^2 - U^2) + 2\omega_\perp(u-U) = 0 \qquad \text{(D-6)}$$

where $\omega_\perp = \omega\cos\psi$.

Eliminating w between these two equations gives

$$uv_x - m(U^2-u^2) + v_z\frac{UU_x - uu_x}{u_z} - 2\omega_\perp(U-u) = 0 \qquad \text{(D-7)}$$

Now using the relation for v given in section 4.1

$$v = (u-U)\tan\beta = f\tan\beta \cong f\beta$$

where $f = u-U$ is the velocity defect. We can rewrite equation (D-7) as

$$(u+f)\ (f\beta_x+f_x\beta) - m(U^2-U^2-f^2-2fU) + \beta f_z \frac{UU_x-(U+f)\ (U_x+f_x)}{f_x} + 2\omega_\perp f = 0$$

which reduces to

$$\beta_x - \beta\frac{U_x}{U+f} = -\ m\ \frac{2U+f}{U+f} - \frac{2\omega_\perp}{U+f}$$

The velocity defect f is small compared to U in the outer part of the boundary layer so we may neglect it. The equation then becomes

$$\beta_x - \beta\ \frac{U_x}{U} = -2m - \frac{2\omega_\perp}{U} \qquad \text{(D-8)}$$

The solution of (D-8) is

$$\beta = e^{\int_o^x \frac{U_x}{U}\,dx}\left\{ -\ 2\int_o^x \left(m+\frac{\omega_\perp}{U}\right) e^{-\int_o^x \frac{U_x}{U}\,dx}\,dx + c \right\} \qquad \text{(D-9)}$$

Assuming $\beta = 0$ at the leading edge $x = 0$ gives $c = 0$.

The integral

$$\int_o^x \frac{U_x}{U}\,dx = \int_{U_o}^{U} \frac{dU}{U} = \log\frac{U}{U_o}$$

so

$$e^{\int_o^x \frac{U_x}{U}\,dx} = e^{\log\frac{U}{U_o}} = \frac{U}{U_o}$$

Using this in equation (D-9) gives

$$\beta = -\ 2\ \frac{U}{U_o}\int_o^x \frac{U_o}{U}\left[m + \frac{\omega_\perp}{U}\right] dx$$

As U_o is independent of x this simplifies to

$$\beta = -2U\int_o^x \left[\frac{m}{U} + \frac{\omega_\perp}{U}\right] dx \qquad \text{(D-10)}$$

APPENDIX E

Skin Friction Formula

In order to find the skin-friction for our experimental data we have plotted the velocity profiles in "law of the wall" plot. This plot is shown in Figure 24. The straight portion of the curves correspond to the logarithmic law found in two-dimensional turbulent boundary layers and the dotted curves correspond to the linear velocity profiles which we expect will exist in the layer closest to the wall, the so-called "laminar sublayer". We expect a velocity profile drawn in this plot to have one portion parallel to the dotted lines and one parallel to the straight lines. The transition between the curved and straight portion will, of course, be a continuous curve over a finite distance and not a discontinuity in the slope as shown in the figure. The skin-friction has been read from that part of the velocity profile which was parallel to the straight lines in the plot. For profiles well away from the separation line it was easy to find the proper skin-friction value as several data points were in the logarithmic region. For profiles closer to separation the wake-profile dominates the profile-shape so the skin-friction here had to be read from one or two points found in the logarithmic region. The skin-friction, as read by this method, is the proper value in the limiting streamline direction. In order to get the values for the x and y direction we have to multiply with $\cos\alpha$, respectively $\sin\alpha$.

For the boundary layer equations we need to express the skin-friction coefficient in the x-direction C_f as a function of θ_{xx} and H. Such a function has been found by Ludwieg and Tillmann (Ref. 34).

$$C_f = \frac{0.246e^{-1.561H}}{(R_\theta)^{0.268}} \qquad \text{(E-1)}$$

It is generally known that this formula will underestimate C_f for high C_f-values and overestimate it for low values (Ref. 12). This is also the case with our data as shown in Figure 25 and we have made an attempt to correct for this by suggesting the formula

$$C_f = \frac{0.93e^{-1.56H}}{(R_\theta)^{0.47}} \qquad \text{(E-2)}$$

which, as seen in Figure 25, fits our data fairly well.

APPENDIX F

Auxiliary Equations for the Energy Equation

The energy equation contains both the regular shape factor $H = \frac{\delta_x^*}{\theta_{xx}}$ and the second shape-factor $\bar{H} = \frac{\delta_x^{**}}{\theta_{xx}}$. Using a velocity profile family it is possible to find a relation between H and $\bar{H}$. If we use the simple power law profile $\frac{u}{U} = \left(\frac{z}{\delta}\right)^{\frac{1}{n}}$ where from the definition of H, $n = \frac{2}{H-1}$ we get

$$\bar{H} = \frac{4H}{3H-1} \tag{F-1}$$

This was used by Truckenbrodt (Ref. 35) and is plotted in Figure 26 together with our data. If we use the profile family of Section 3, we get

$$\bar{H} = F(H, C_f \cos\beta) \tag{F-2}$$

which also is plotted in the same figure. Neither of the methods seem to give a good agreement with our data and as the points show a large scatter it is not possible to detect any specific trend for different $C_f \cos\beta$ values. Instead we have chosen to fit an empirical curve to our data. The function

$$\bar{H} = \frac{4H}{3.3H-1.5} \tag{F-3}$$

is also shown on Figure 26 and is suggested for use with three-dimensional boundary layer. Equation (F-3) was found using a power-law profile $\frac{u}{U} = \left(\frac{z}{\delta}\right)^{\frac{1}{n}}$ where

$$n = \frac{1}{0.54H-0.58} \tag{F-4}$$

The dissipation terms in the energy equation are given by equation (1.3-7) as

$$\frac{d\tau}{\rho} = \int_0^\delta \nu \left(\frac{\partial u}{\partial z}\right)^2 dz \tag{F-5}$$

Truckenbrodt used an empirical relation

$$\frac{d\tau}{\rho U^3} = \frac{0.56\ 10^{-2}}{(R_\theta)^{1/6}} \tag{F-6}$$

which was based on Rotta's experimental findings (Ref. 36).

In order to find the shape-factor equation we combine the energy and momentum equations. The dissipation term in the resulting equation is

$$\frac{2(d+t)}{\rho U^3} - \bar{H}\frac{C_f}{2} \tag{F-7}$$

When using the Truckenbrodt expression (F-6) for $d+t/\rho U^3$ we also must use the Ludwieg-Tillmann formula (E-1) for the skin-friction C_f. The resulting relation is a function of H and R_θ.

The main objection against using equation (F-6) is that it does not give the correct value of H for the case of a two-dimensional boundary layer over a flat plate. For this particular case we have $H = 1.4$ and $dH = dU = 0$ so the dissipative terms must also be zero.

$$\frac{2(d+t)}{\rho U^3} - \bar{H}\frac{C_f}{2} = 0$$

This gives us $H = 1.5\text{-}1.6$ depending on the R_θ-value, and not $H = 1.4$, as expected. A slight correction of the constant in equation (F-6) could, of course, take care of this. However, it would be more convenient if we could have the same R_θ dependence in $\frac{d+t}{\rho U^3}$ as in C_f.

It is possible to derive such a relation if we assume the shape of the velocity profile and eddy viscosity distribution across the boundary layer. For simplicity we assume the velocity profile to follow the power law $\frac{u}{U} = \left(\frac{z}{\delta}\right)^{\frac{1}{n}}$ with n from equation (F-4). From pipe and flat plate data we know that the eddy viscosity has an essentially parabolic distribution. We assume it to be

$$\frac{\nu}{U\delta} = C_f K\left[\frac{z}{\delta} - \left(\frac{z}{\delta}\right)^2\right]$$

where K is a constant. Using this in definition of $\frac{d+t}{\rho}$, (F-5), we get

$$\frac{d+t}{\rho U^3} = \frac{KC_f}{2n\left(\frac{2}{n}+1\right)} \tag{F-8}$$

with n from equation (F-4).

The dissipative terms in the shape-factor equation then become

$$\frac{2(d+t)}{\rho U^3} - \bar{H}\frac{C_f}{2} = \frac{C_f}{2}\left[\frac{K}{2n\left(\frac{2}{n}+1\right)} - \bar{H}\right] \tag{F-9}$$

with n from equation (F-4) and $\bar{H}$ from equation (F-3). K is then found so that the dissipation terms become zero for $H = 1.4$. The numerical value becomes $K = 12.8$.

APPENDIX G

Free-Stream Data for the Rotating Case

When applying the calculation-scheme to a case where the blades are rotating, we want a configuration which shows the typical magnitude of the cross-flow and can also be compared with the stationary case. Both of these requirements will automatically be satisfied if we choose a symmetric configuration having the same velocity distribution in a coordinate system fixed to the blades. Thus, we assume that the rotating stage is both preceded and followed by stator vanes of a symmetric configuration as shown in this figure.

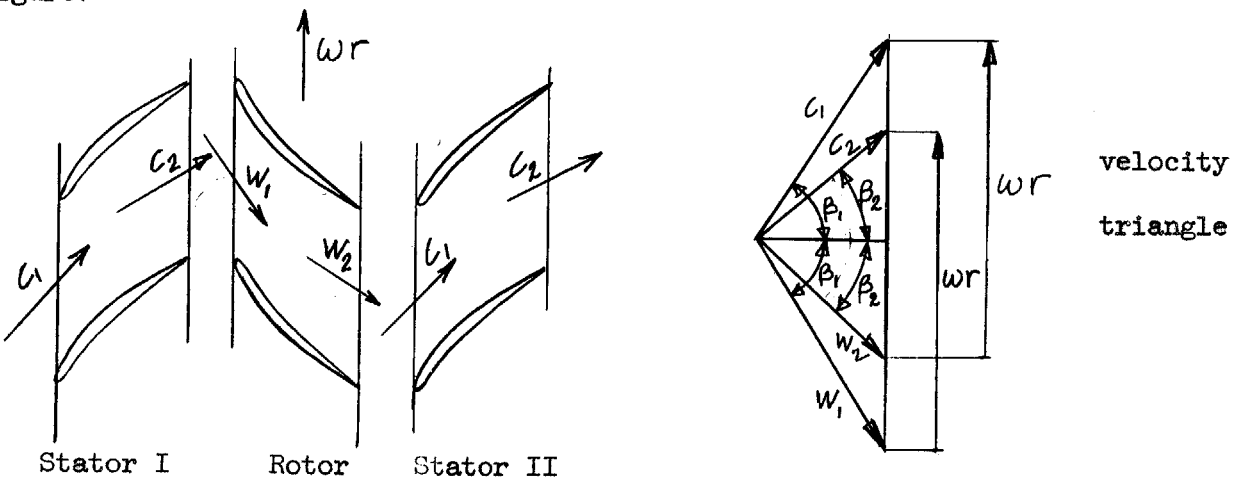

The axial velocity is assumed constant and that will fix the magnitude of ω from the velocity triangle also shown in the figure.

These requirements can only be satisfied at one span-position. The mid-span position was chosen so the calculations made for 30% and 70% span position merely show the trend in changes of the cross-flow. c_1, β_1 and β_2 were taken from the experiments (Fig. 9) and this gives $\omega = 123 \frac{1}{sec}$ for the mid-span position. The same ω was then used for the 30 and 70% span positions.

The radial or spanwise pressure gradient is known for the stators from the experiments. Thus, we know the gradient in both the inlet and exit of the rotor. A probable distribution within the rotor has then been assumed.

During the actual calculations it was found that terms involving the angular speed ω was two to five times as large as terms involving the radial pressure gradient. Therefore, an error in the assumed distribution of the radial pressure gradient will only affect the calculations slightly.

The streamline curvature m is found from the cross-wise equation of motion written for the flow outside of the boundary layer, equation (A-18). As, in general, $\sin K$ is small compared to unity and $(x-d')$ small compared to R we may write the equation

$$m = \frac{\frac{\partial p}{\partial y}}{\rho U^2} - \frac{2\omega_1}{U} + \frac{R\omega^2}{U^2} \qquad \text{(G-1)}$$

The spanwise velocity gradient $\frac{\partial U}{\partial y}$ is found from combining equation (G-1) with the irrotationality condition, equation (1.3-4). This gives

$$\frac{1}{U}\frac{\partial U}{\partial y} = -\frac{1}{\rho U^2}\frac{\partial p}{\partial y} + \frac{R\omega^2}{U^2} \qquad \text{(G-2)}$$

The free streamline divergence or convergence term $\frac{1}{U}\frac{\partial \bar{V}}{\partial y}$ was introduced on page 4 of Section 1.

$$\bar{V} = U \tan K$$

$$\frac{\partial \bar{V}}{\partial y} = \frac{\partial U}{\partial y}\tan K + \frac{U}{\cos^2 K}\frac{\partial K}{\partial y}$$

and $\cos^2 K \approx 1$

$$\frac{1}{U}\frac{\partial \bar{V}}{\partial y} = \frac{\partial K}{\partial y} + \frac{1}{U}\frac{\partial U}{\partial y}\tan K \qquad \text{(G-3)}$$

From definition $m = \frac{\partial K}{\partial x}$

but $$dK = \frac{\partial K}{\partial x}dx + \frac{\partial K}{\partial y}dy$$

so $$\frac{dK}{dx} = \frac{\partial K}{\partial x} + \frac{\partial K}{\partial y}\frac{dy}{dx}$$

Our calculations are always done by following one free streamline, so $y = 0$ and $\frac{dy}{dx} = 0$. Hence

$$\frac{dK}{dx} = \frac{\partial K}{\partial x} = m$$

or $$K = \int_0^x m\,dx + C\,(y)$$

then $$\frac{\partial K}{\partial y} = \int_0^x \frac{\partial m}{\partial y}\,dx + C_1(y)$$

Using this relation in equation (G-3) gives

$$\frac{1}{U}\frac{\partial \bar{V}}{\partial y} = \left[\frac{R\omega^2}{U^2} - \frac{1}{\rho U^2}\frac{\partial p}{\partial y}\right]\tan K + \int_0^x \frac{\partial m}{\partial y}\,dx + C_1(y) \qquad \text{(G-4)}$$

It was assumed that $C_1(y)$ has the same value in the rotating and stationary case.

The streamline divergence or convergence within the boundary layer is expressed by $\frac{\partial \beta}{\partial y}$ Where β is taken from the inviscid solution, equation (D-10)

$$\beta = -2U\int_0^x \left[\frac{m}{U} + \frac{\omega_1}{U}\right]dx$$

When taking the derivative of m with respect to y we have included the stretching factor $h_1 = 1 - ym$ in equation (G-1) and specialized to $y = 0$ after making the derivation. From equation (A-10) we may see that equation (G-1) should be modified to

$$\frac{m}{1-ym} = \frac{-\frac{\partial p}{\partial y}}{\rho U^2} - \frac{2\omega_1}{U} + \frac{(R+y)\omega^2}{U^2}$$

thus

$$m = \frac{\dfrac{-\frac{\partial p}{\partial y}}{\rho U^2} - \dfrac{2\omega_1}{U} + \dfrac{(R+y)\omega^2}{U^2}}{1+y\left[\dfrac{-\frac{\partial p}{\partial y}}{\rho U^2} - \dfrac{2\omega_1}{U} + \dfrac{(R+y)\omega^2}{U^2}\right]} \qquad \text{(G-5)}$$

taking the derivative before specializing to $y = 0$, we get

$$\frac{\partial m}{\partial y} = \frac{\partial}{\partial y}\left[-\frac{\frac{\partial p}{\partial y}}{\rho U^2} - \frac{2\omega_1}{U} + \frac{R\omega^2}{U^2}\right] + \frac{\omega^2}{U^2} - \left[-\frac{\frac{\partial p}{\partial y}}{\rho U^2} - \frac{2\omega_1}{U} + \frac{R\omega^2}{U^2}\right] \qquad \text{(G-6)}$$

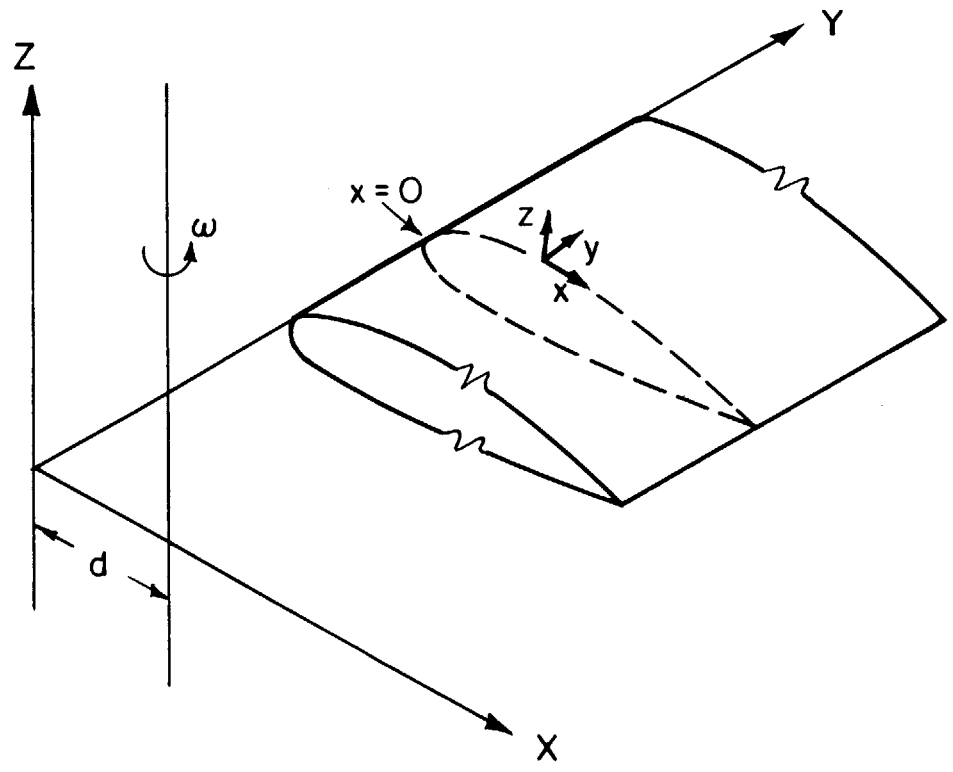

FIG. 1 COORDINATE SYSTEMS

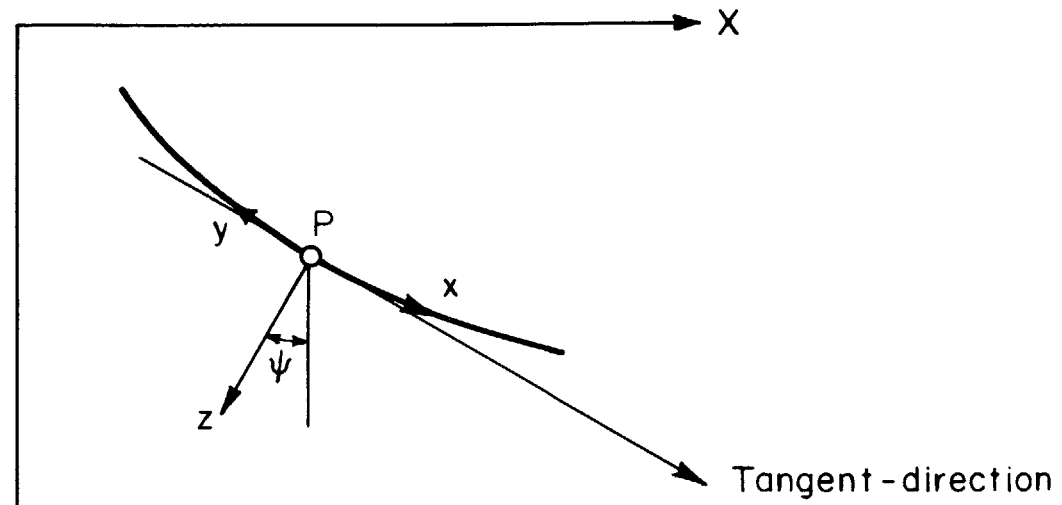

Transformations

$$X = \int_0^x \cos\kappa \cos\psi \, dx - z \sin\psi - y \sin\kappa \cos\psi + X_S$$

$$Y = \int_0^x \sin\kappa \, dx + y \cos\kappa + Y_S$$

$$Z = \int_0^x \cos\kappa \sin\psi \, dx + z \cos\psi - y \sin\kappa \sin\psi + Z_S$$

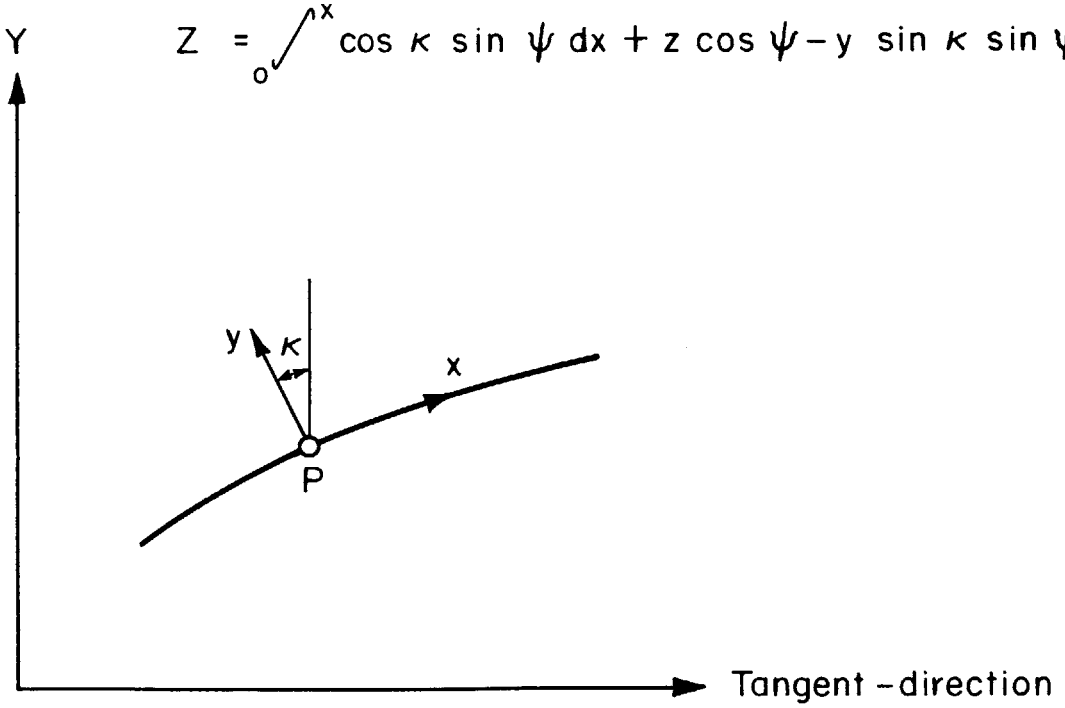

FIG. 2 TRANSFORMATION FROM CARTESIAN COORDINATES X Y Z TO CURVELINEAR COORDINATES x, y, z.

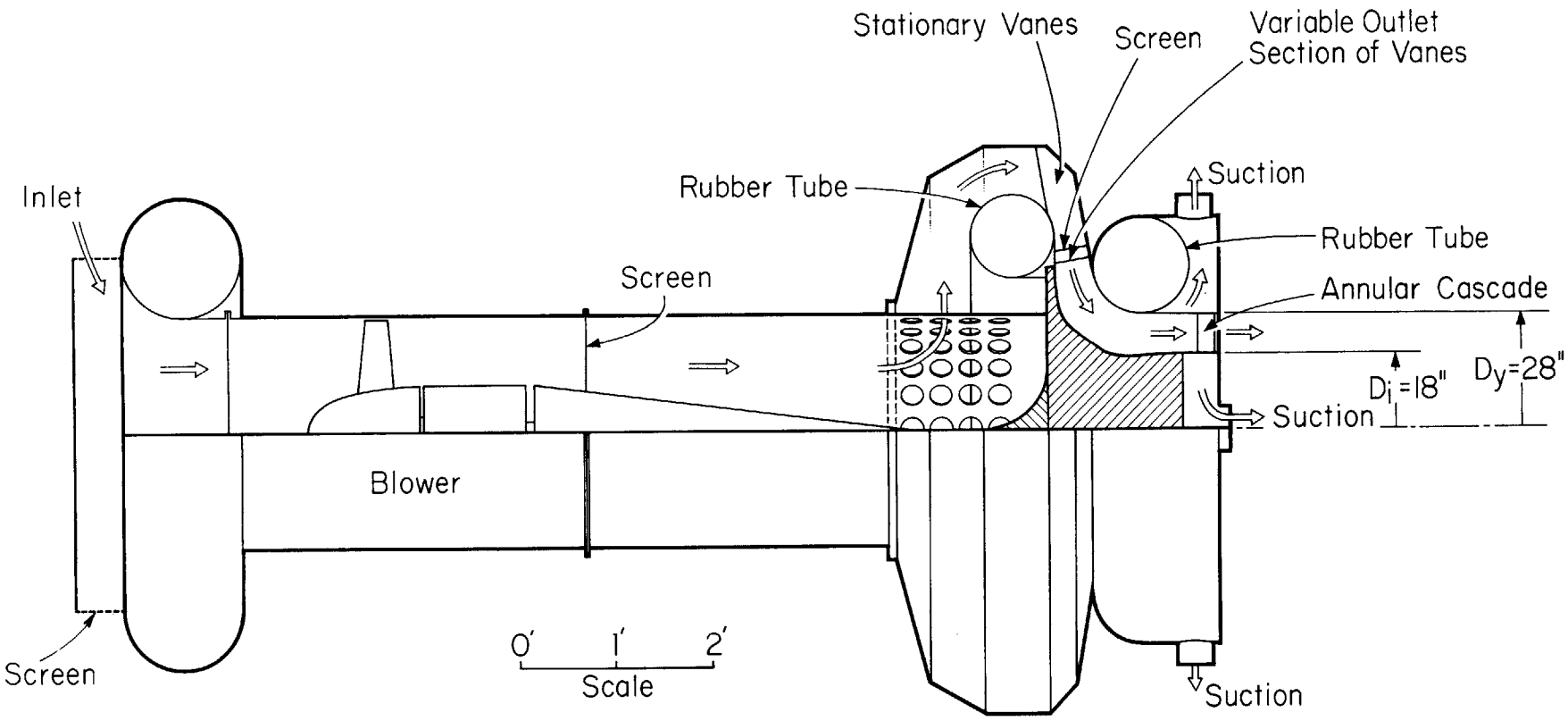

Fig. 3 TEST APPARATUS

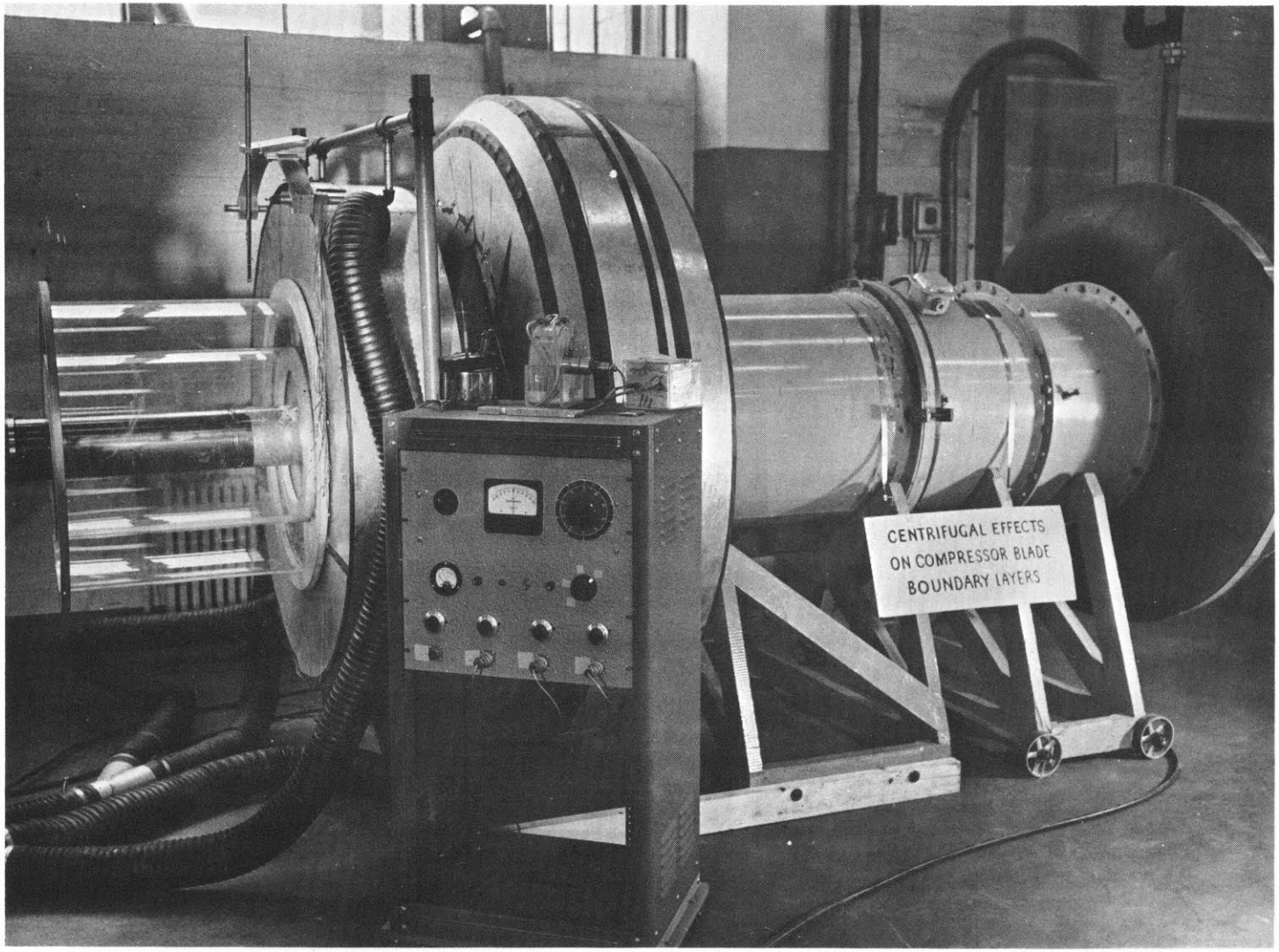

FIG. 4 TEST-APPARATUS WITH ANNULAR EXTENSION.

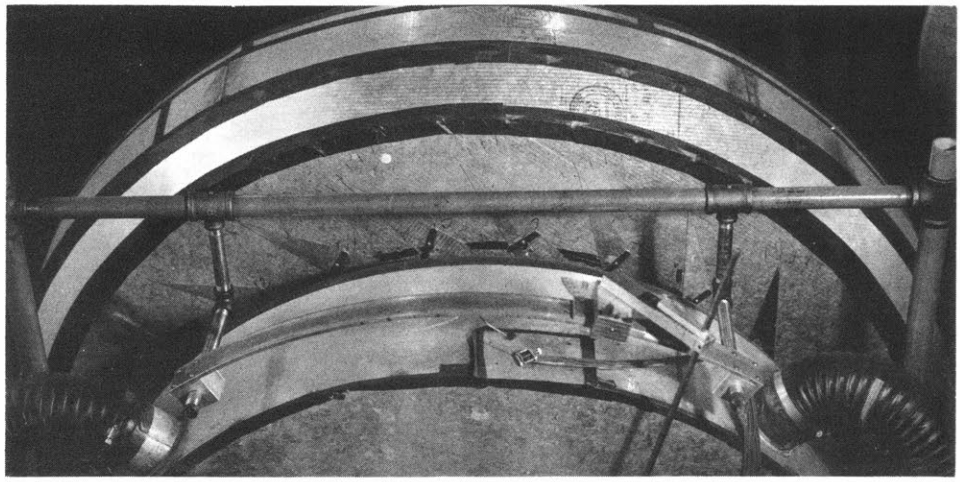

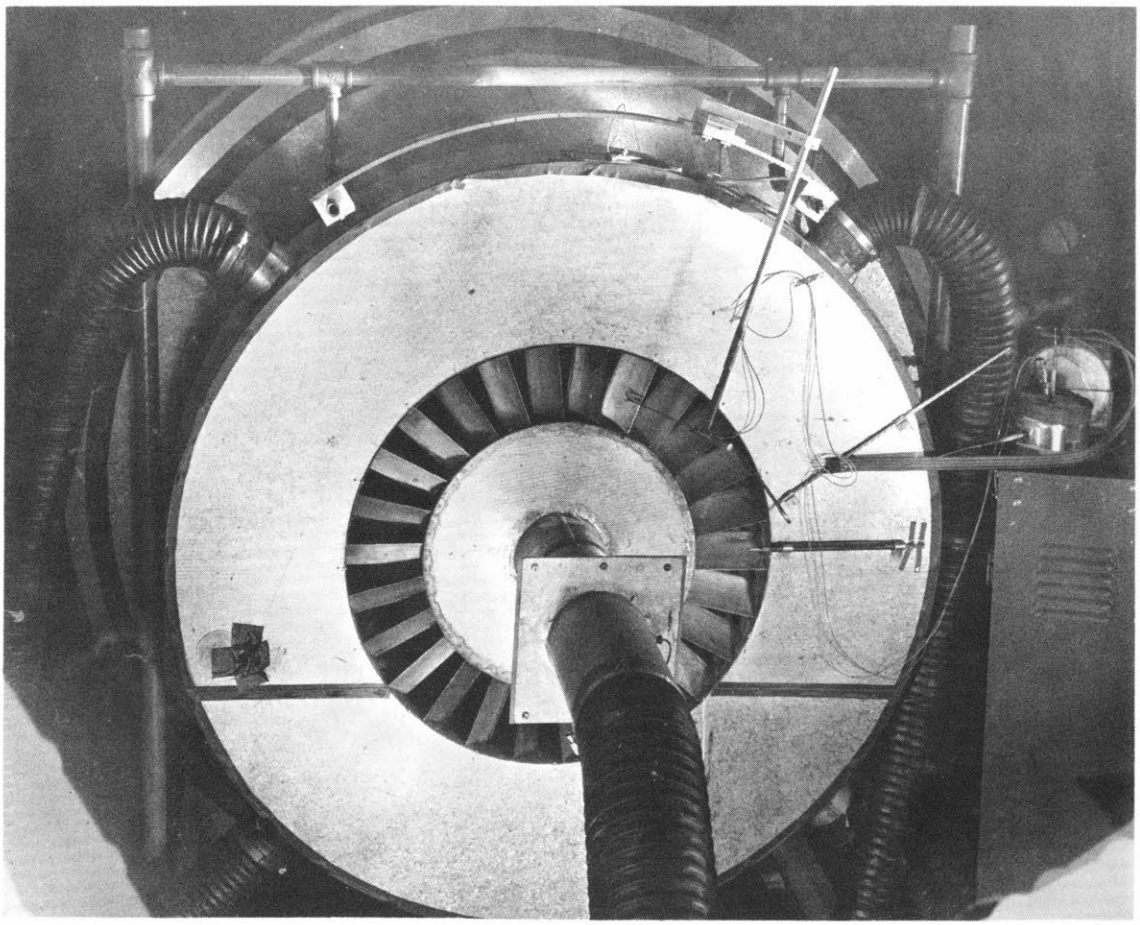

FIG. 5 TEST-APPARATUS.

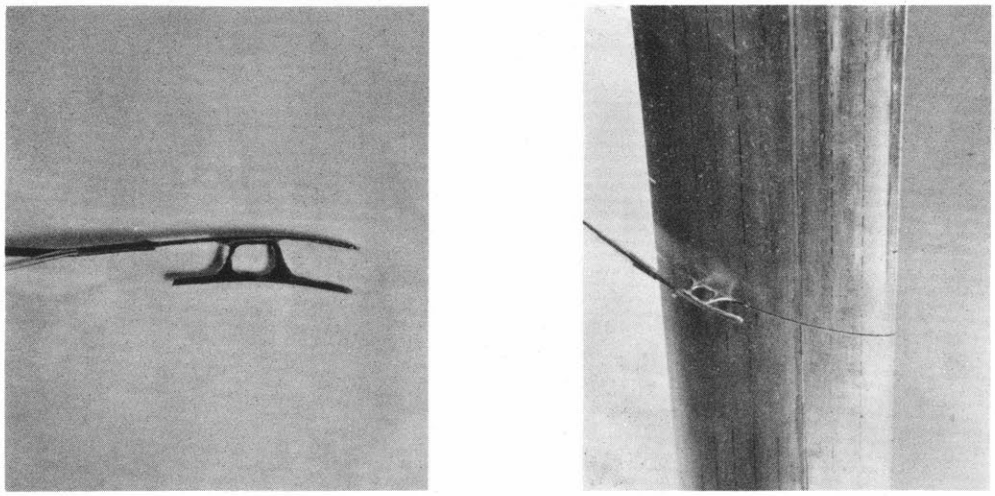

FIG. 6 THREE-HOLE FREE-STREAM COBRA-PROBE

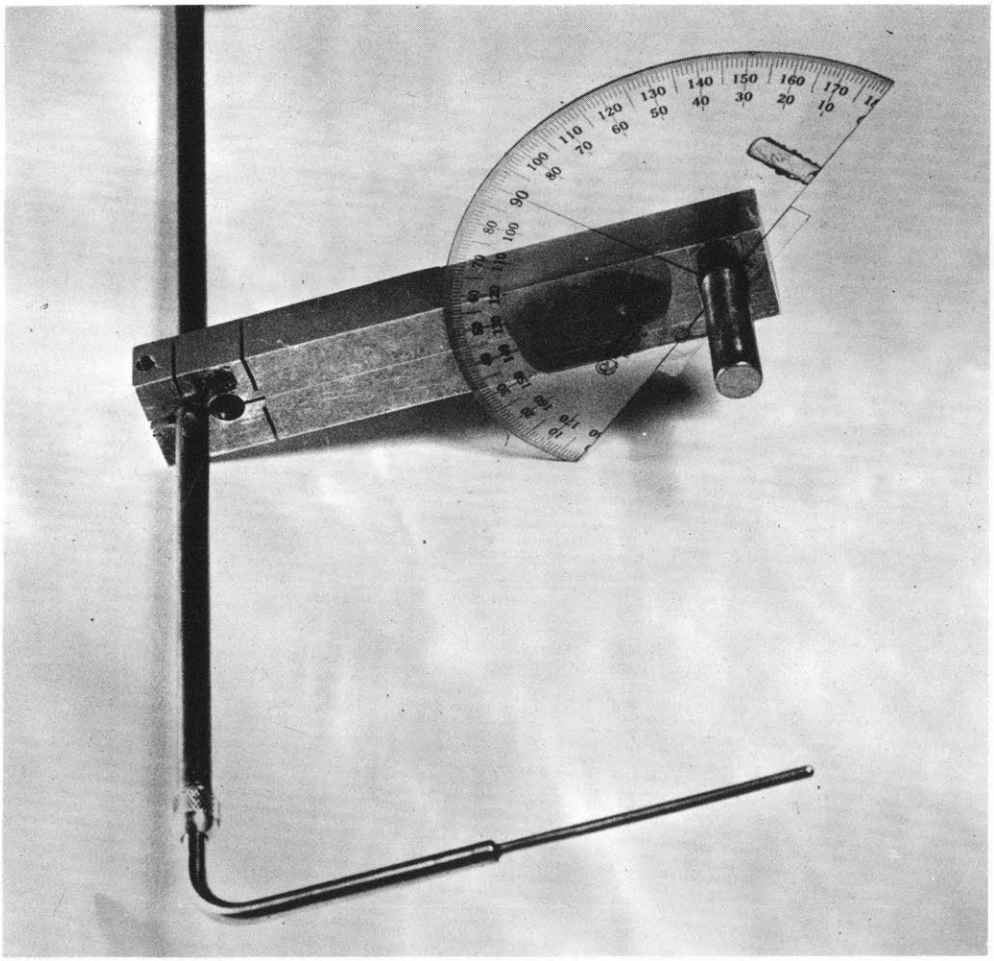

FIG. 7 FIVE-HOLE FREE-STREAM DIRECTION PROBE

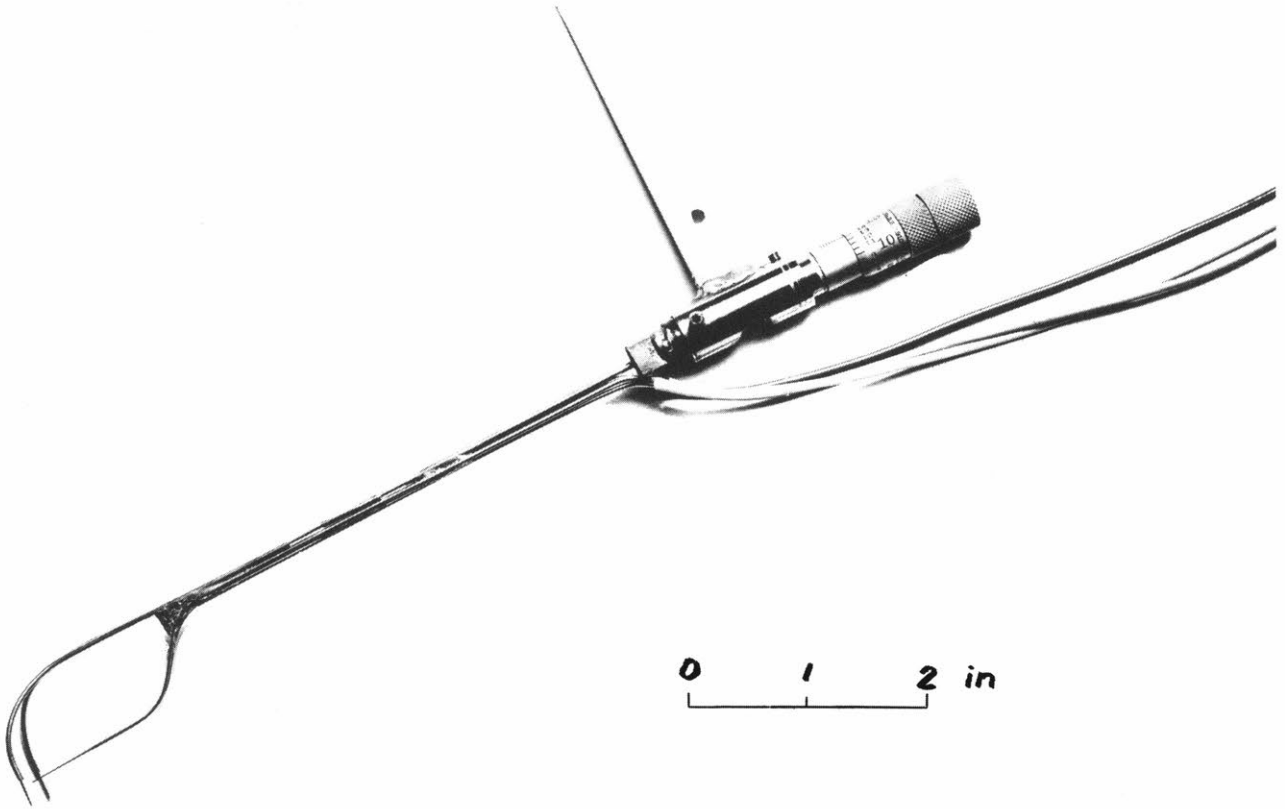

FIG. 8 BOUNDARY LAYER TRAVERSING PROBE.

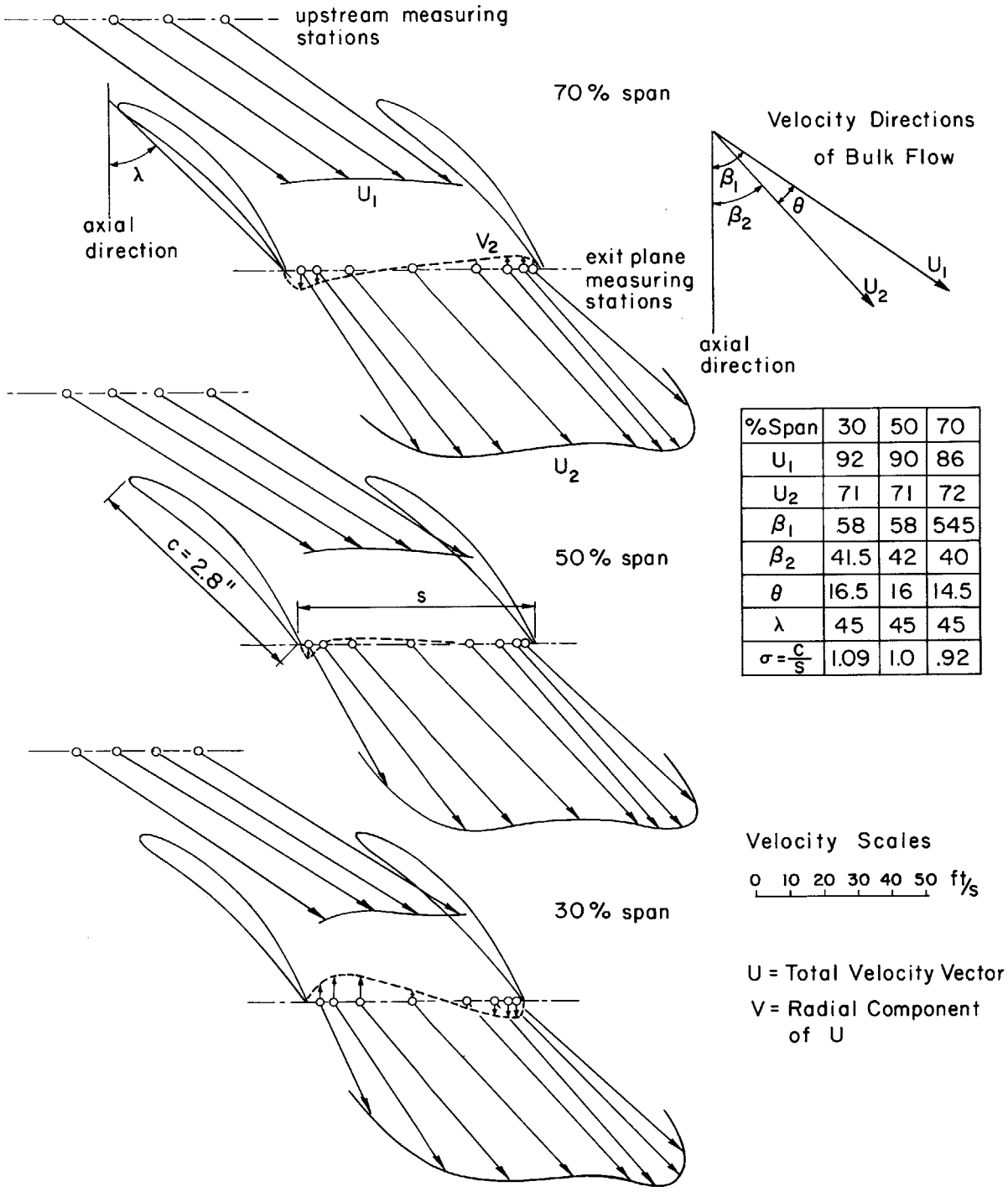

%Span	30	50	70
U_1	92	90	86
U_2	71	71	72
β_1	58	58	545
β_2	41.5	42	40
θ	16.5	16	14.5
λ	45	45	45
$\sigma = \frac{c}{s}$	1.09	1.0	.92

Fig. 9 Directions of Flow Through Cascade

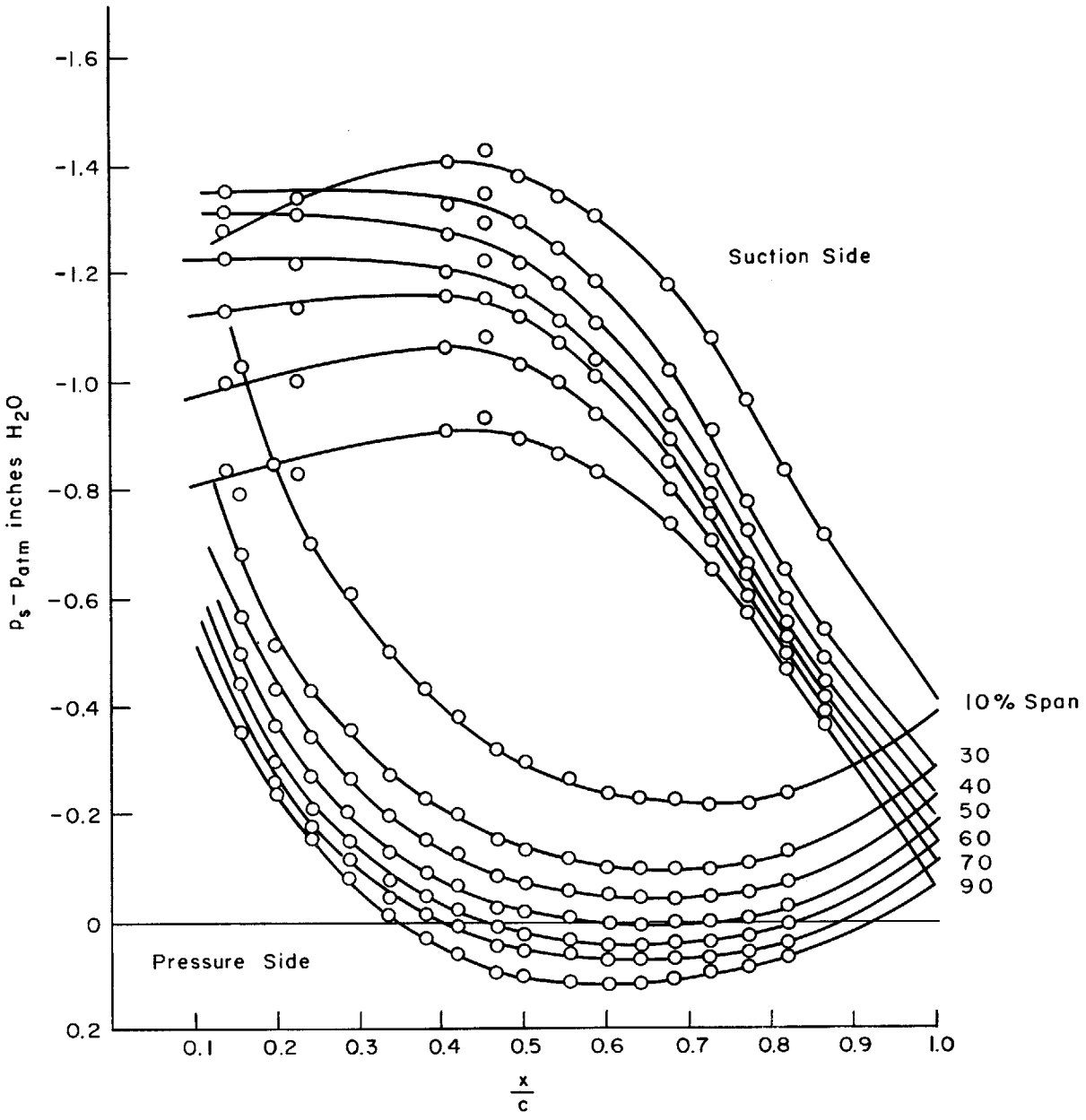

Fig. 10 Pressure Distribution on Blade

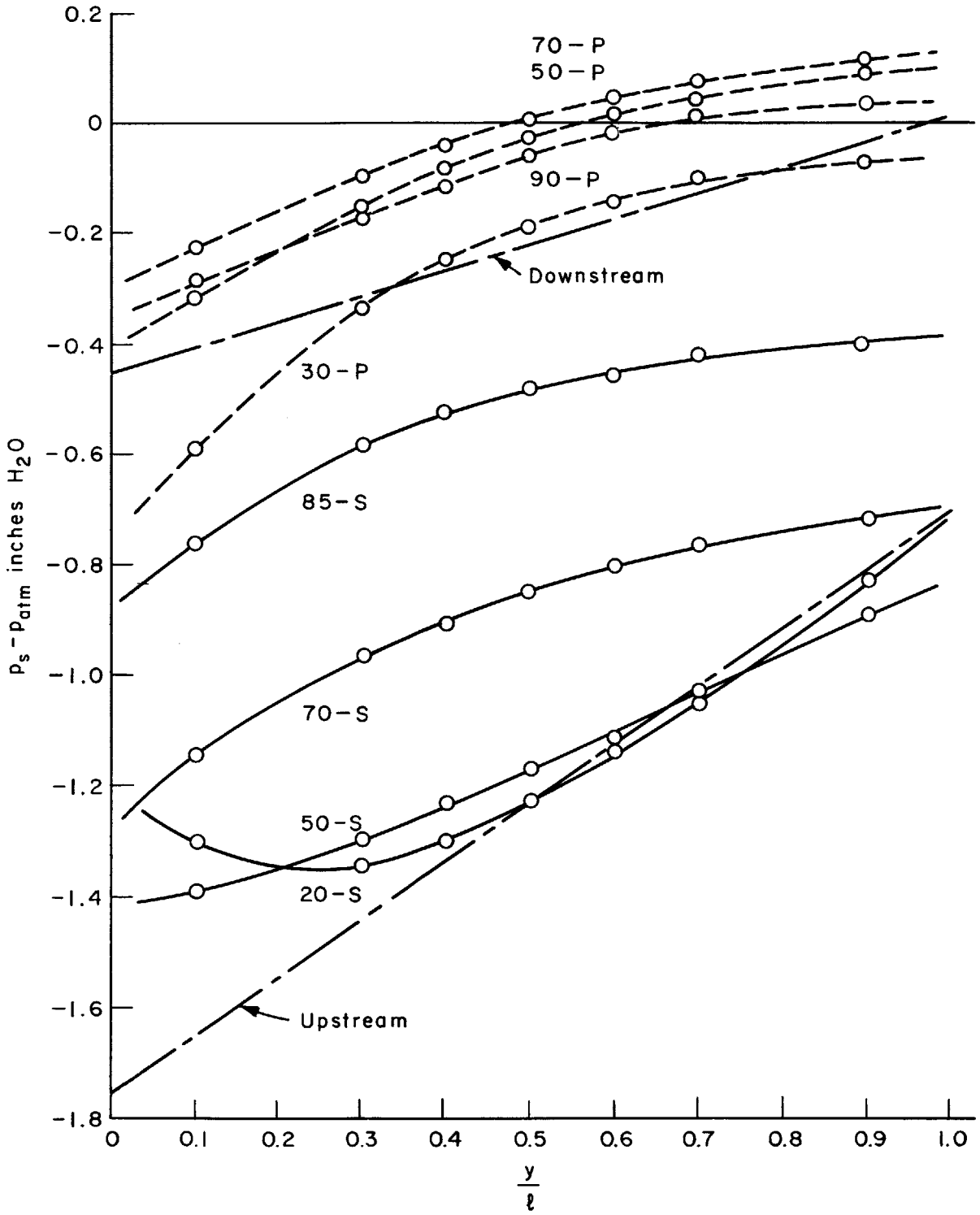

Fig. 11 Pressure Distribution in Cascade

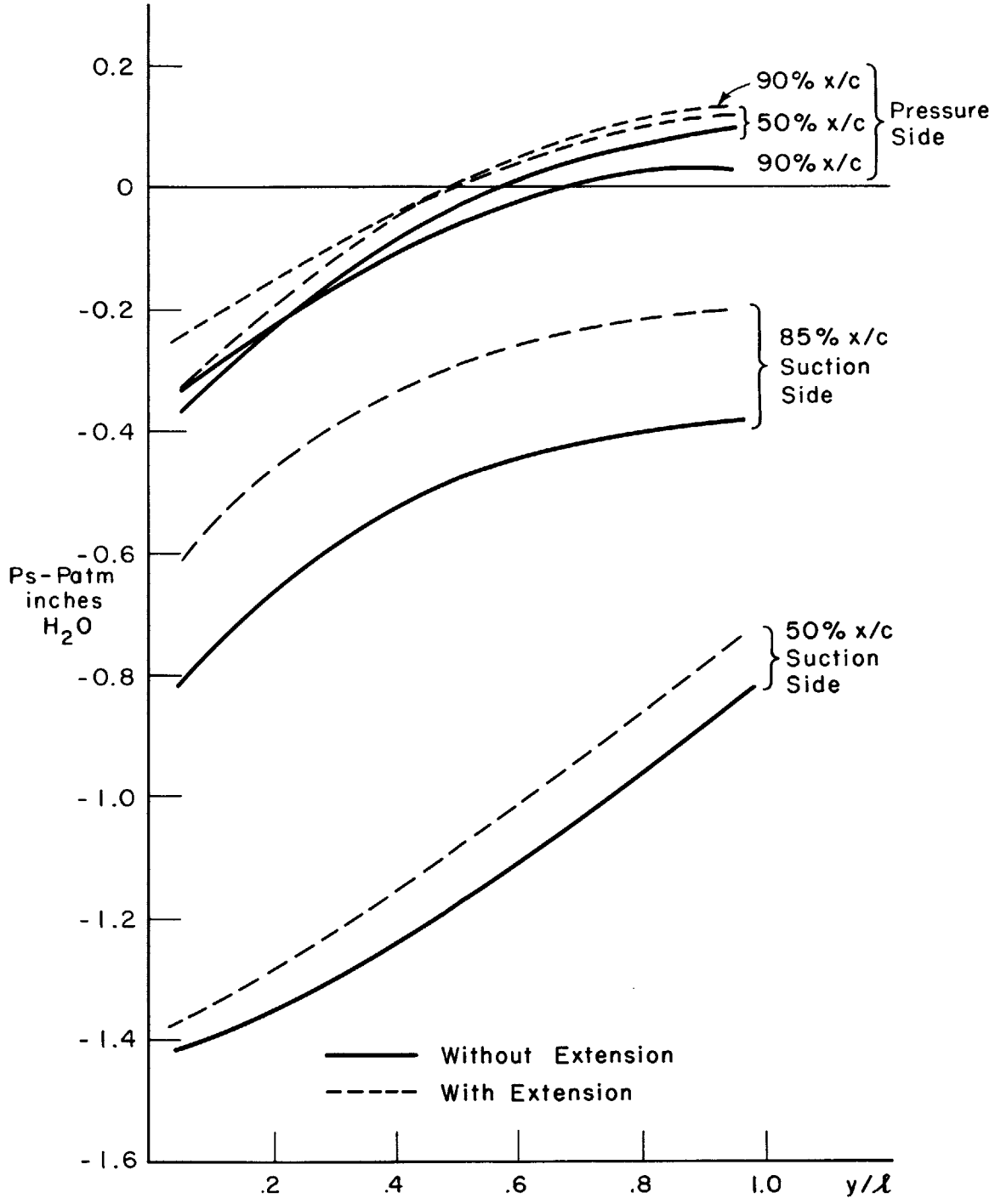

Static Pressure - Distribution as Function of Span - Position

Fig. 12

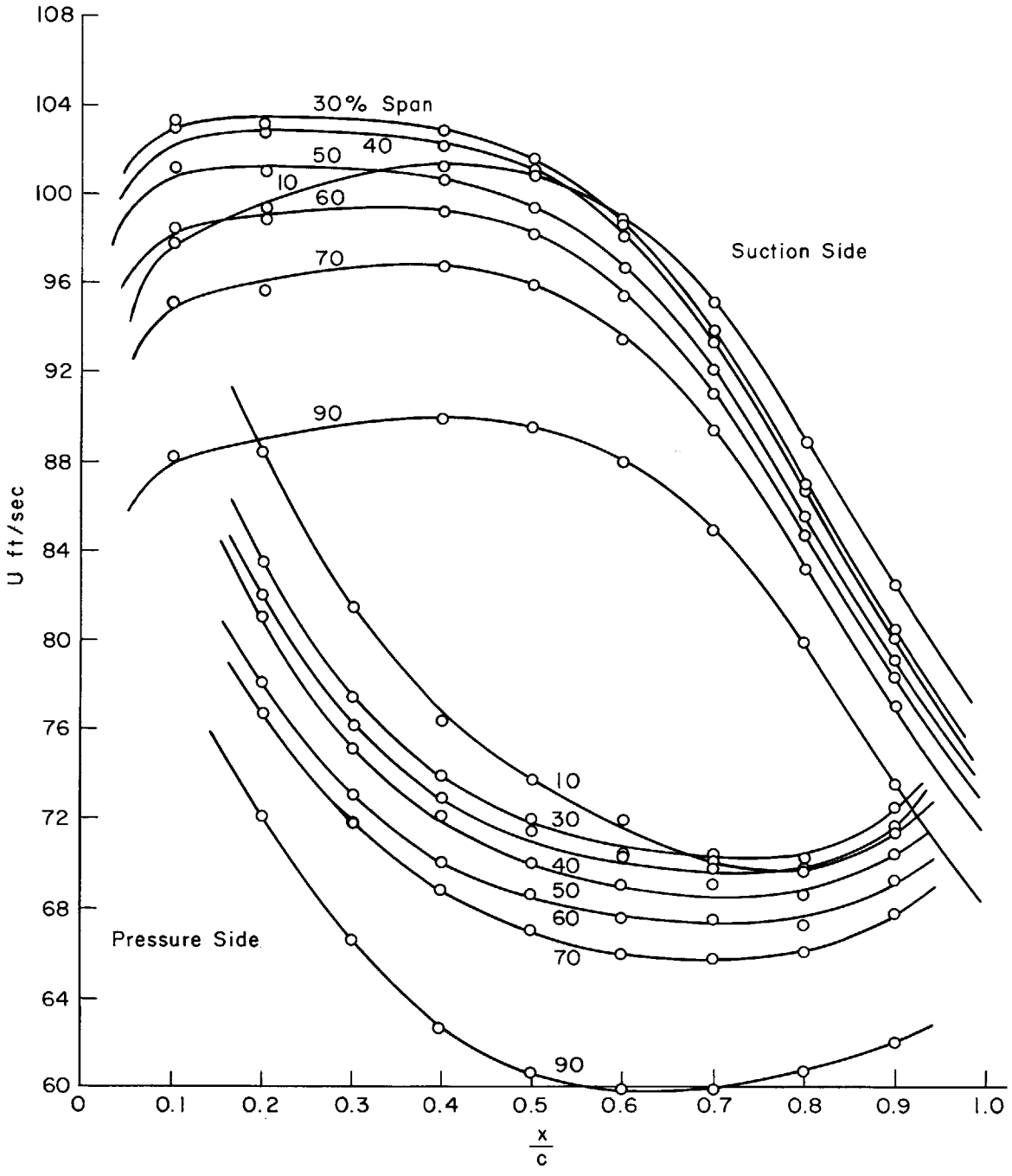

Fig. 13 Velocity Distribution on Blade

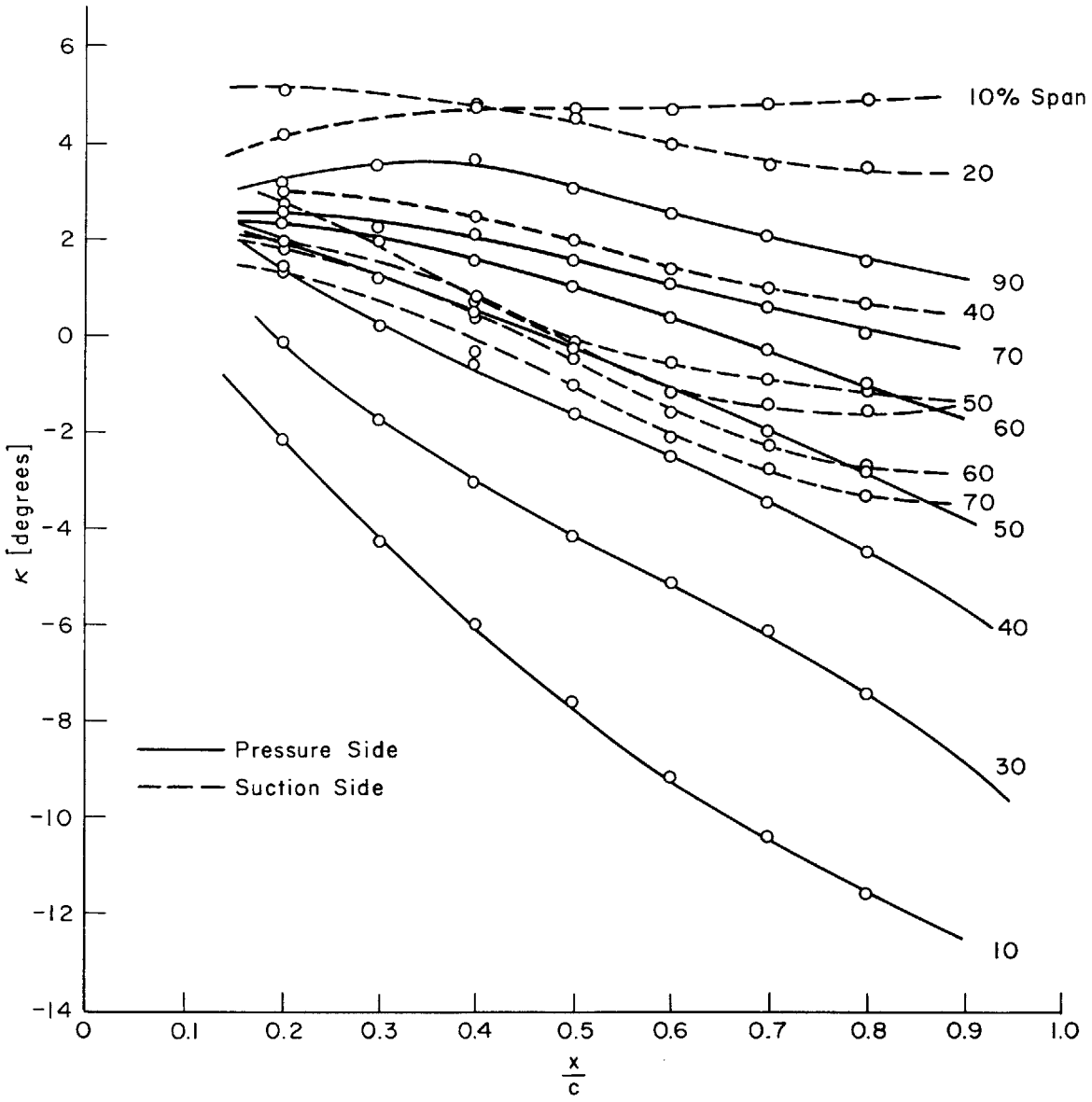

Fig. 14 Angle Between Free Streamlines and Chordline

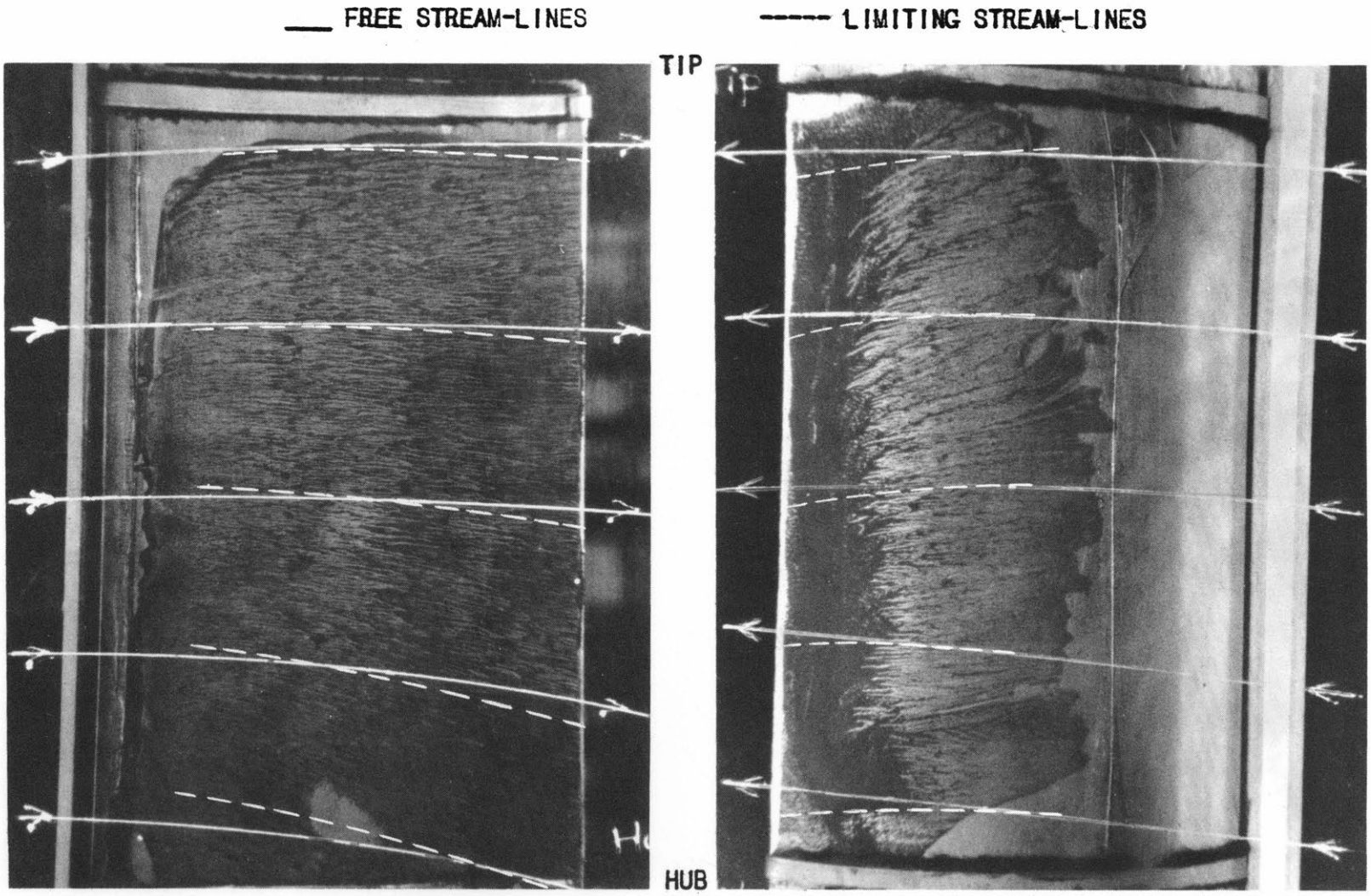

FIG. 15 BLACK-CARBON TRACES ON BLADE.

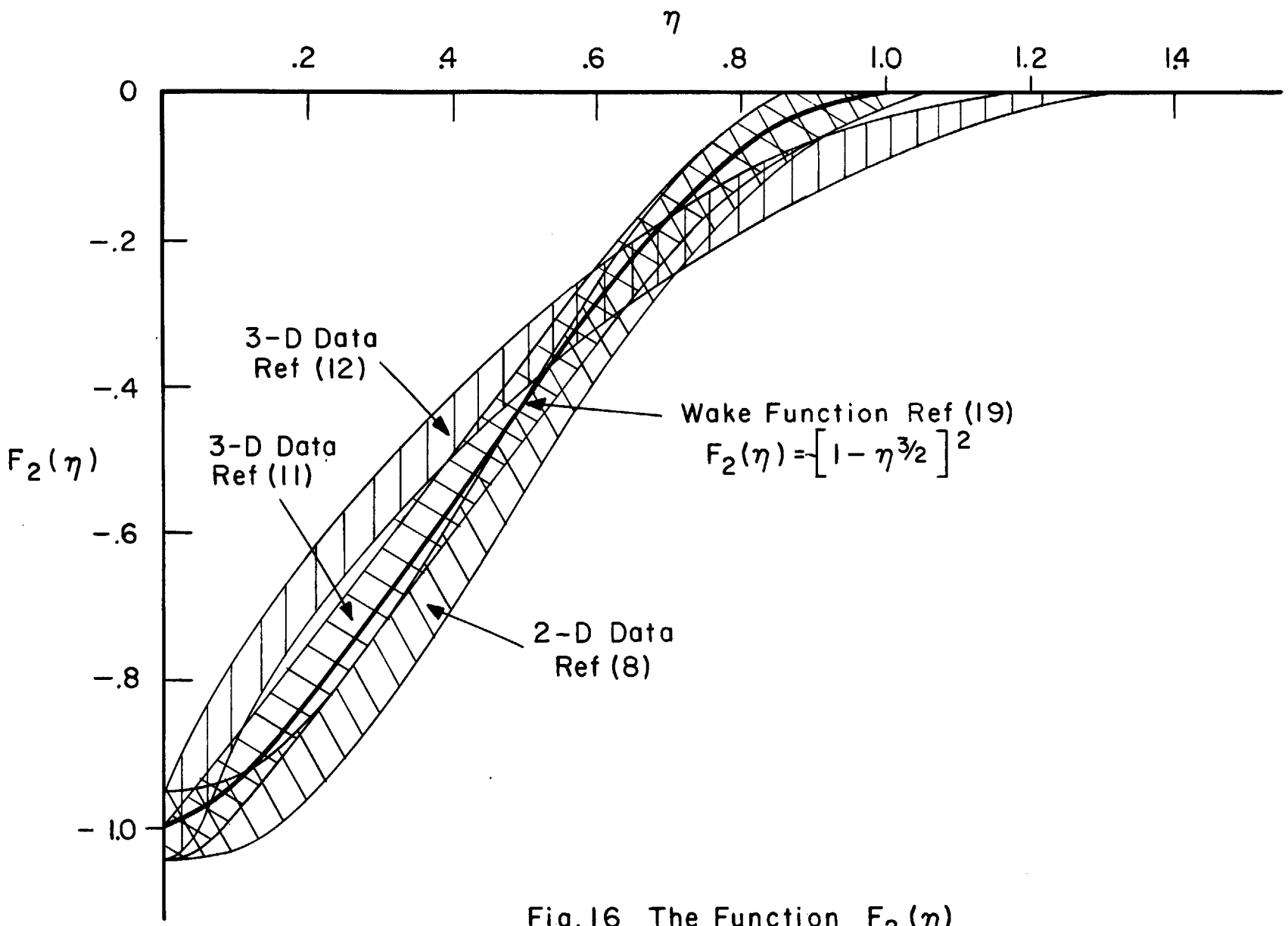

Fig. 16 The Function $F_2(\eta)$

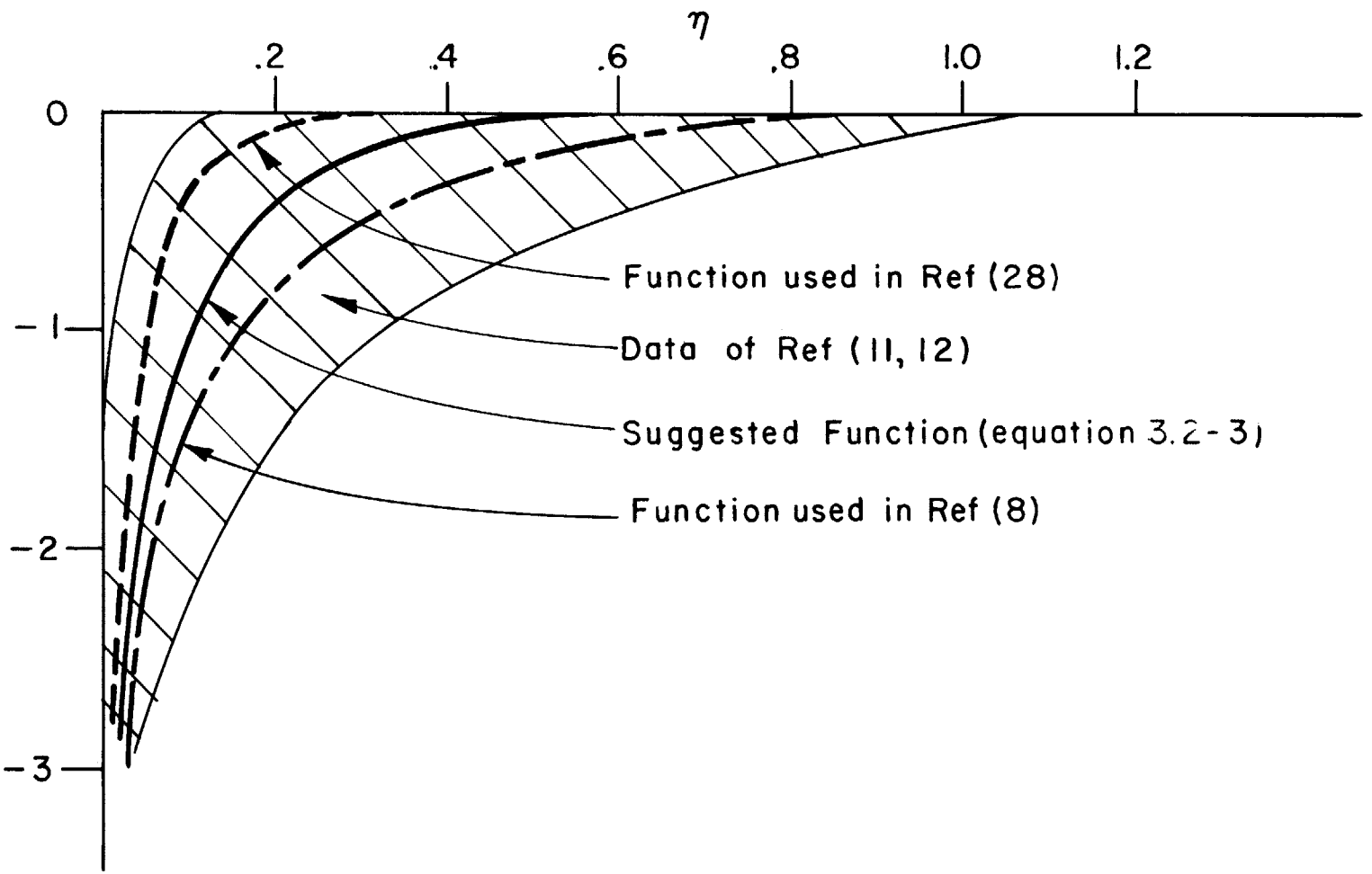

Fig. 17 The Function $F_1(\eta)$

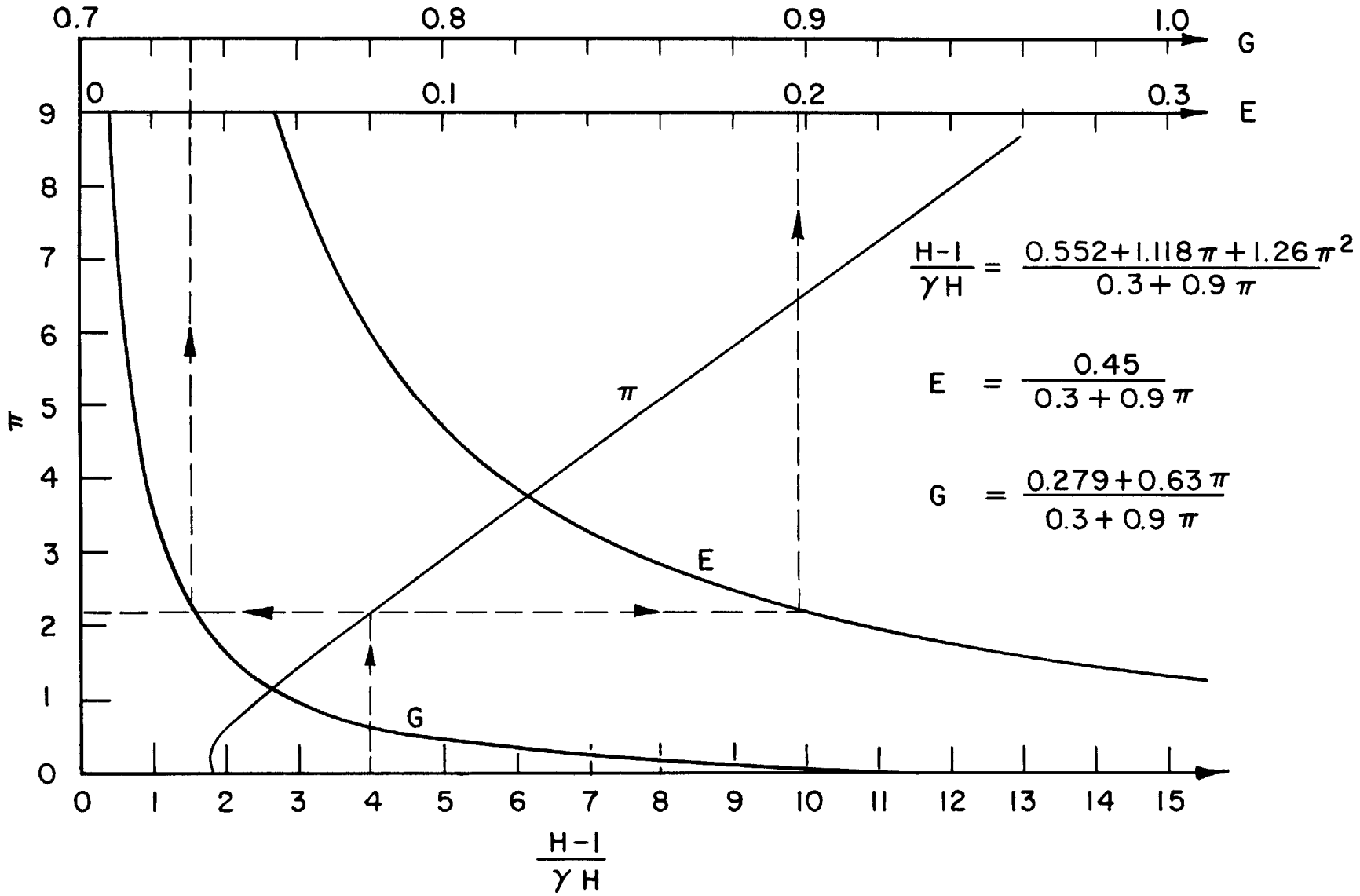

Fig. 18 Functions π, E and G

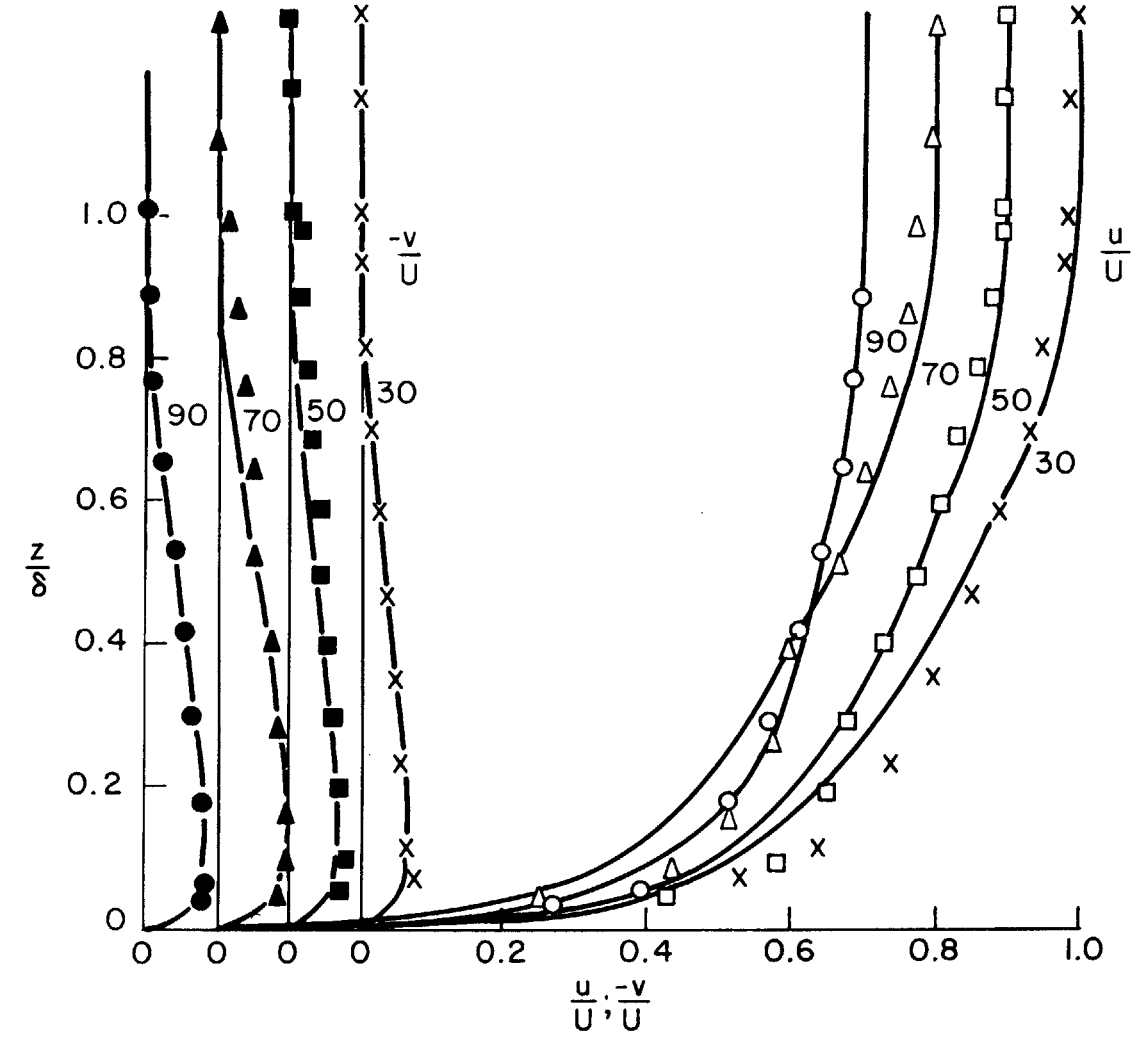

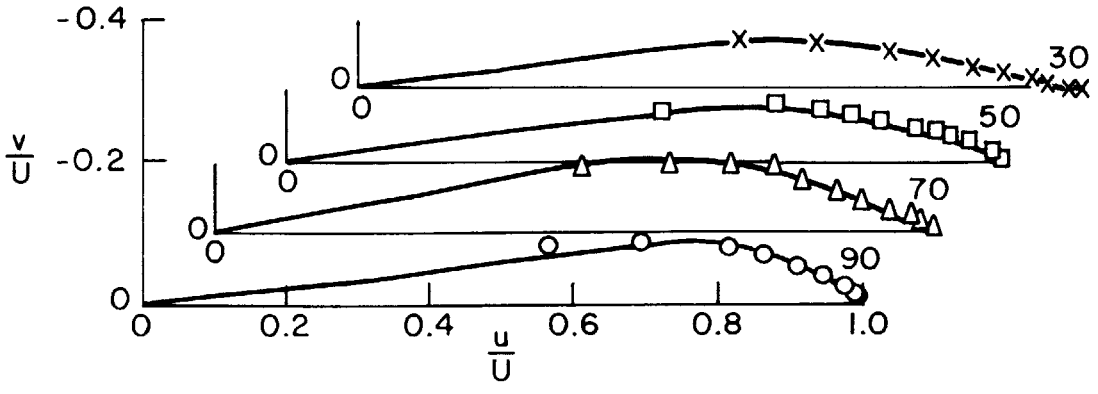

Velocity-Profiles 10% Span Pressure Side

Fig. 19

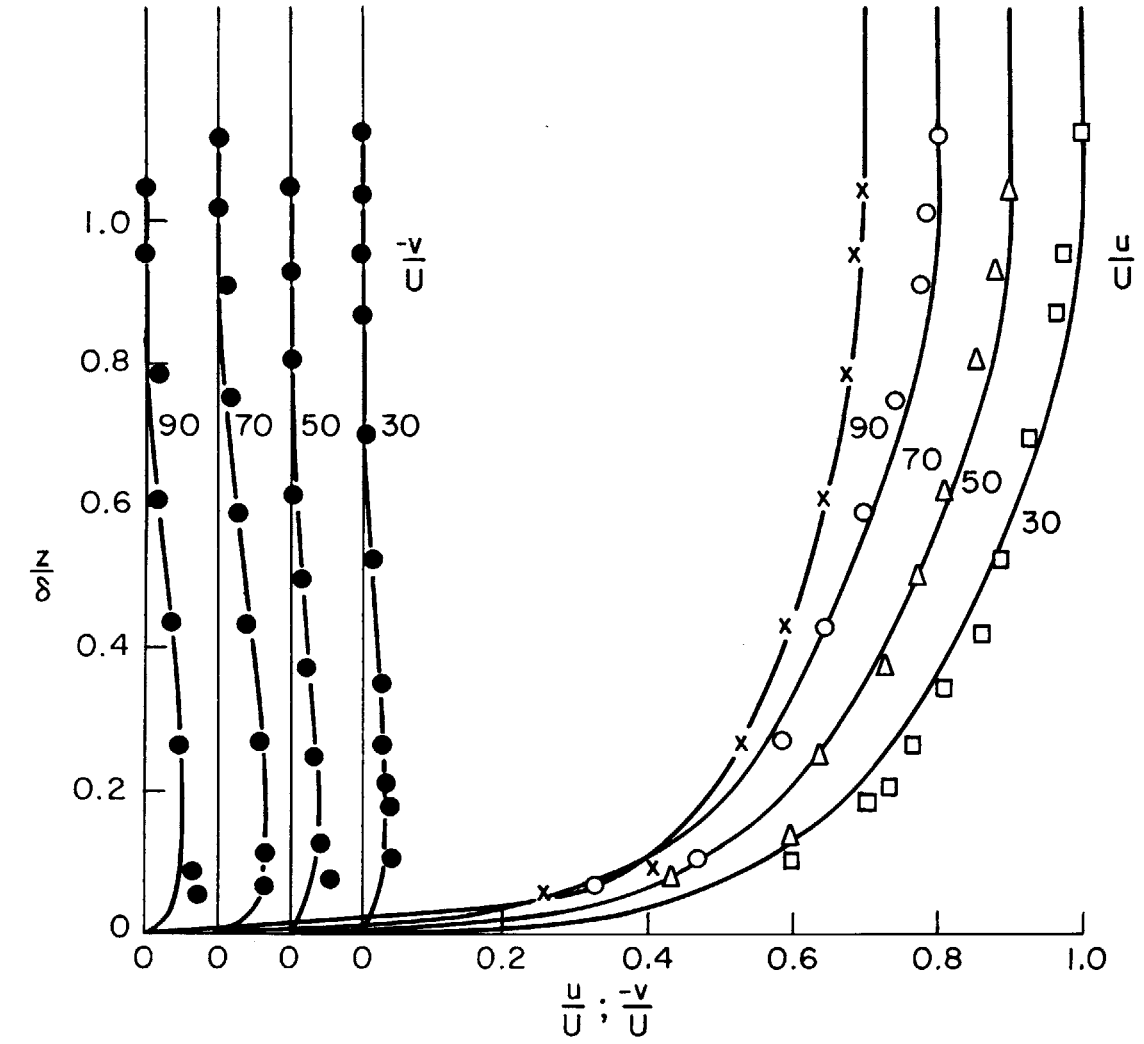

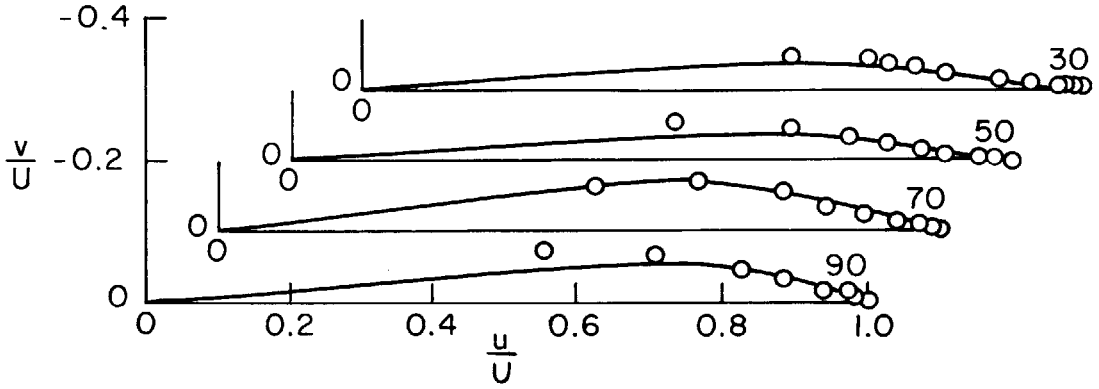

Velocity-Profiles 30% Span Pressure Side

Fig. 19 continued

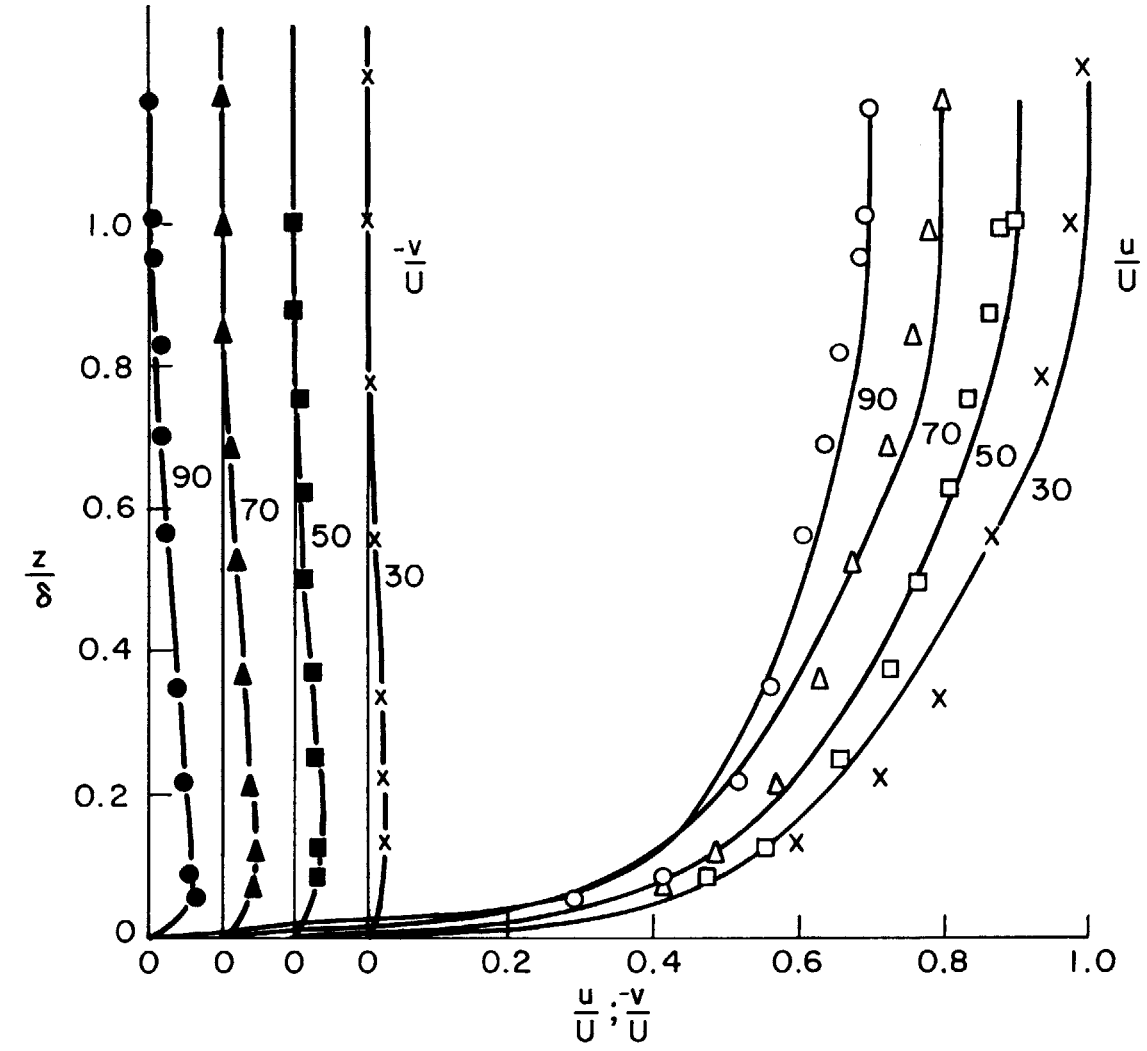

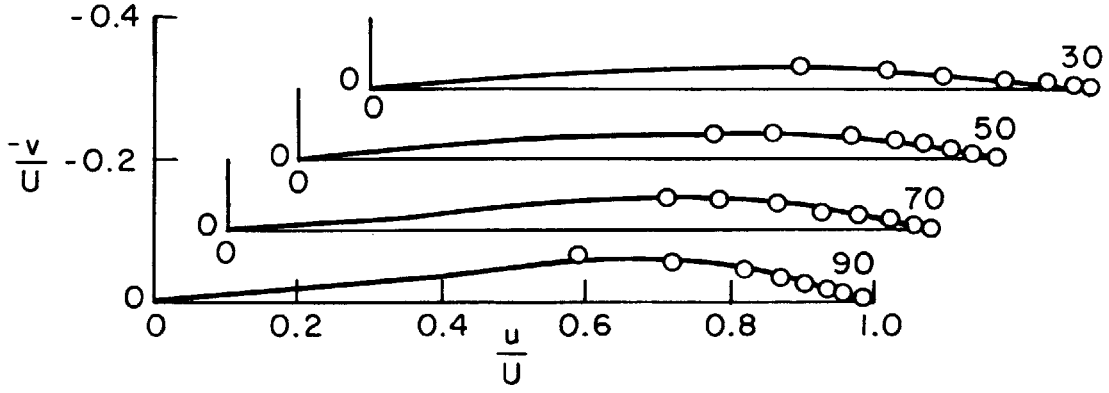

Velocity-Profiles 40% Span Pressure Side

Fig. 19 continued

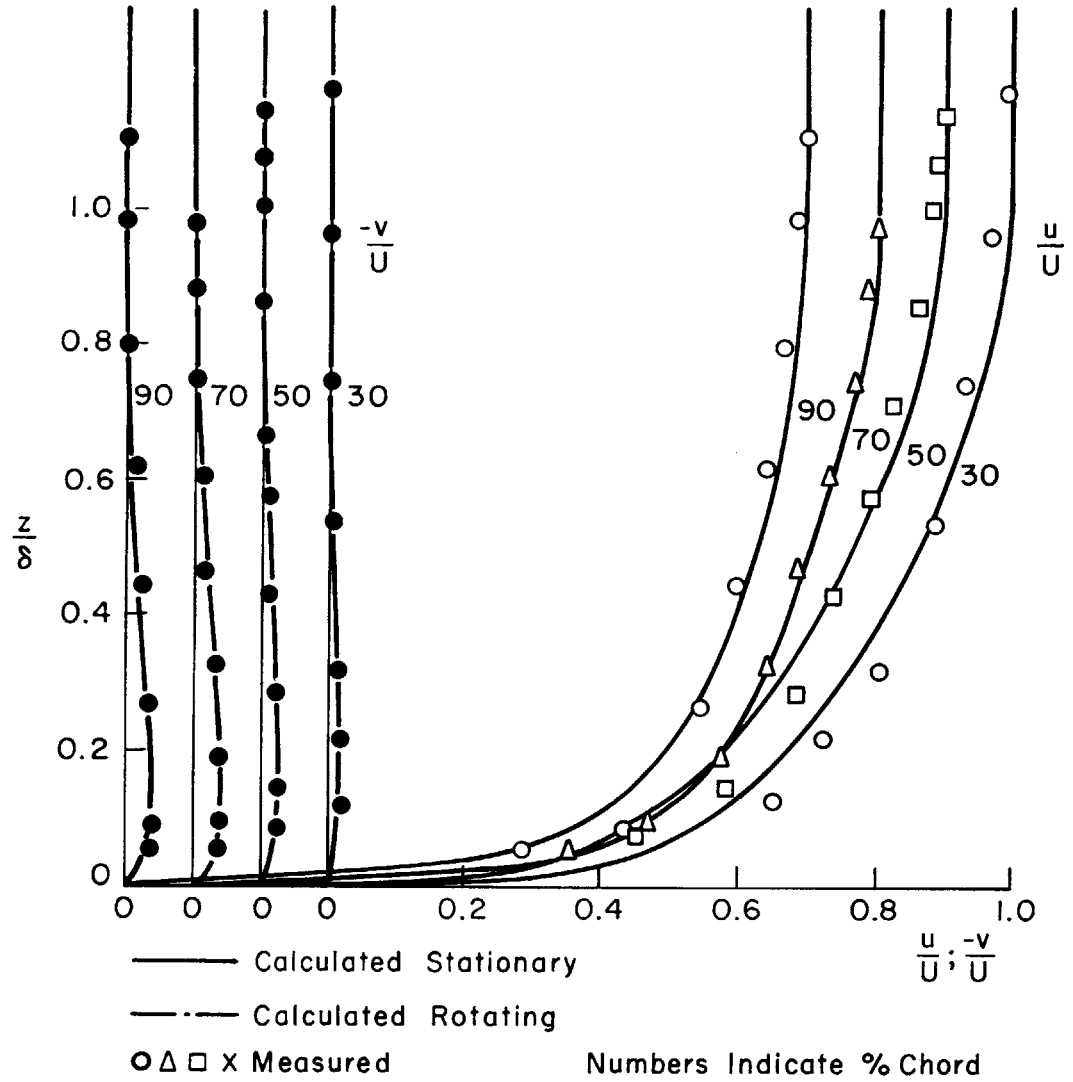

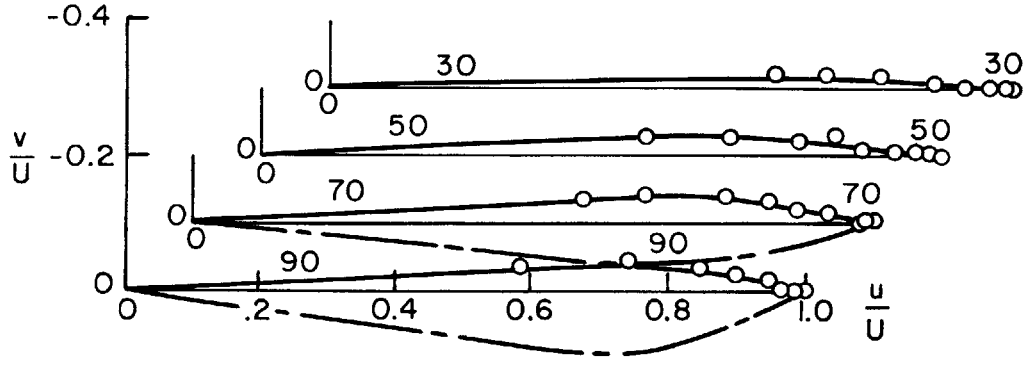

Velocity-Profiles 50% Span Pressure Side

Fig. 19 continued

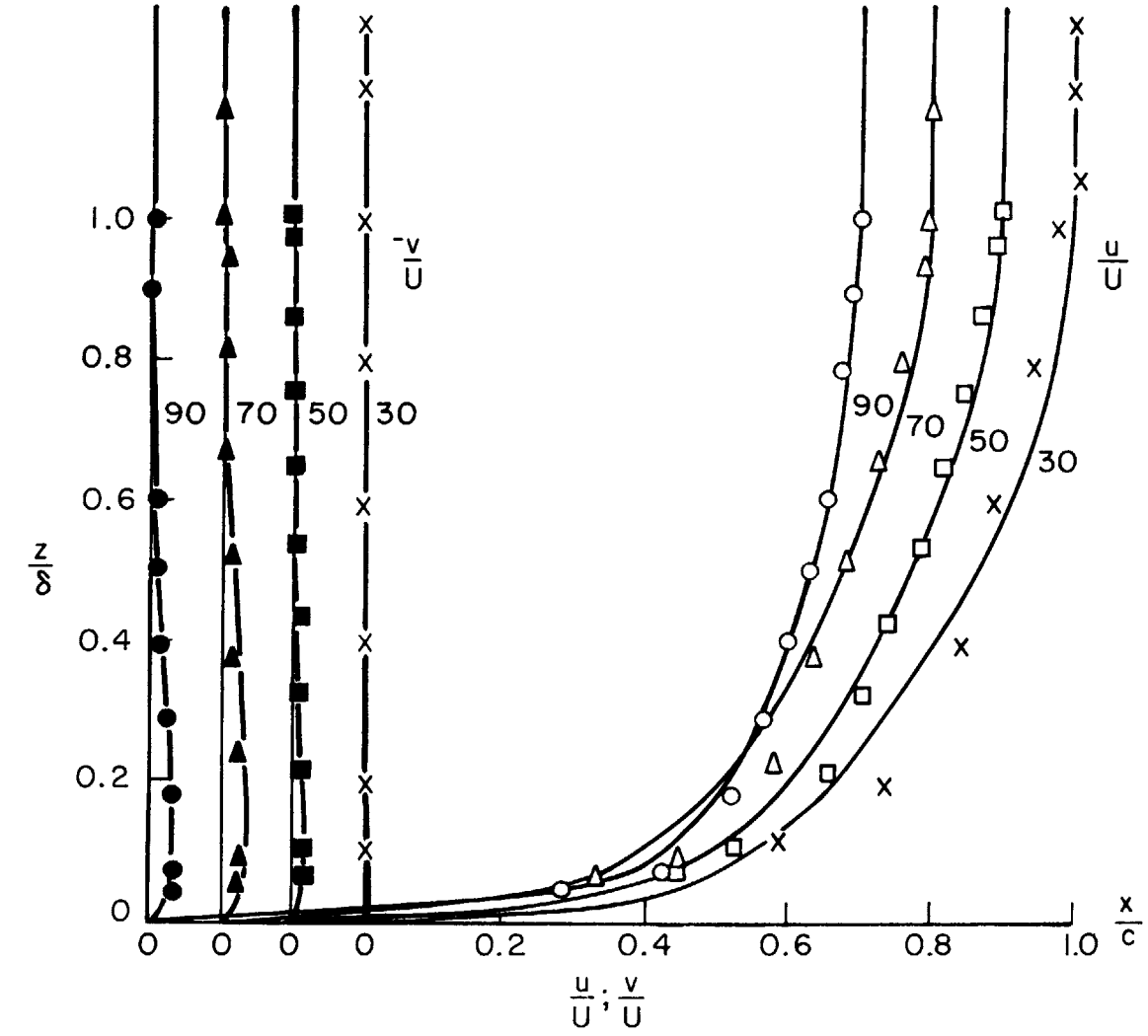

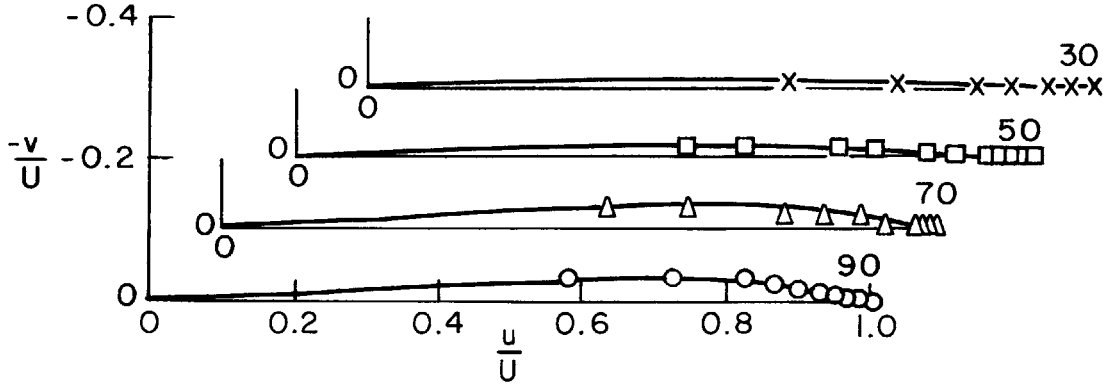

Velocity-Profiles 60% Span Pressure Side

Fig. 19 continued

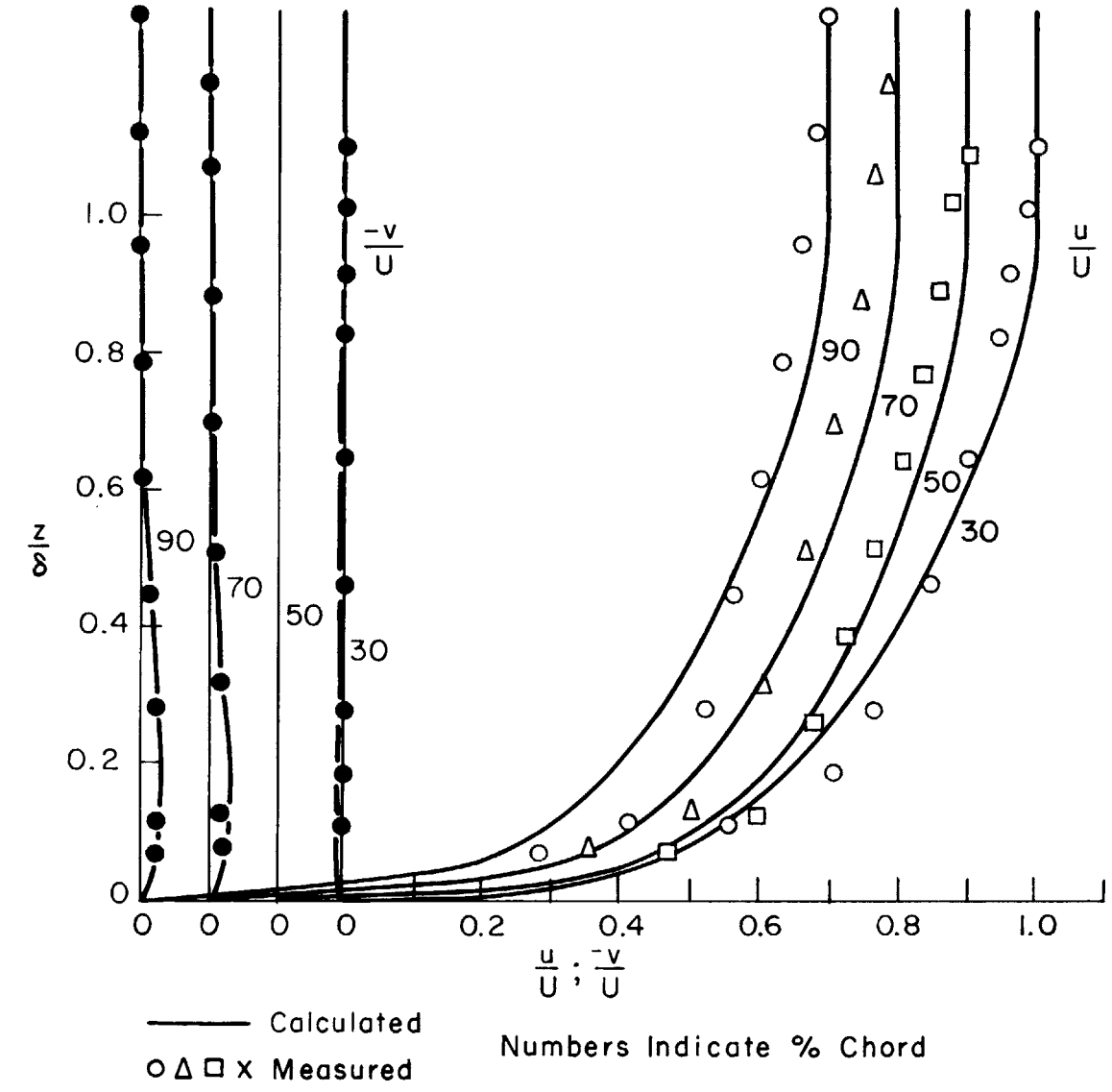

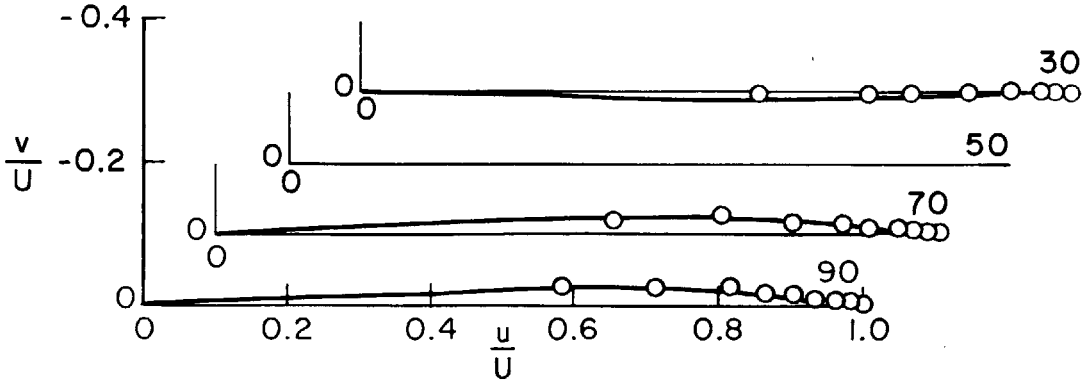

Fig. 19 continued

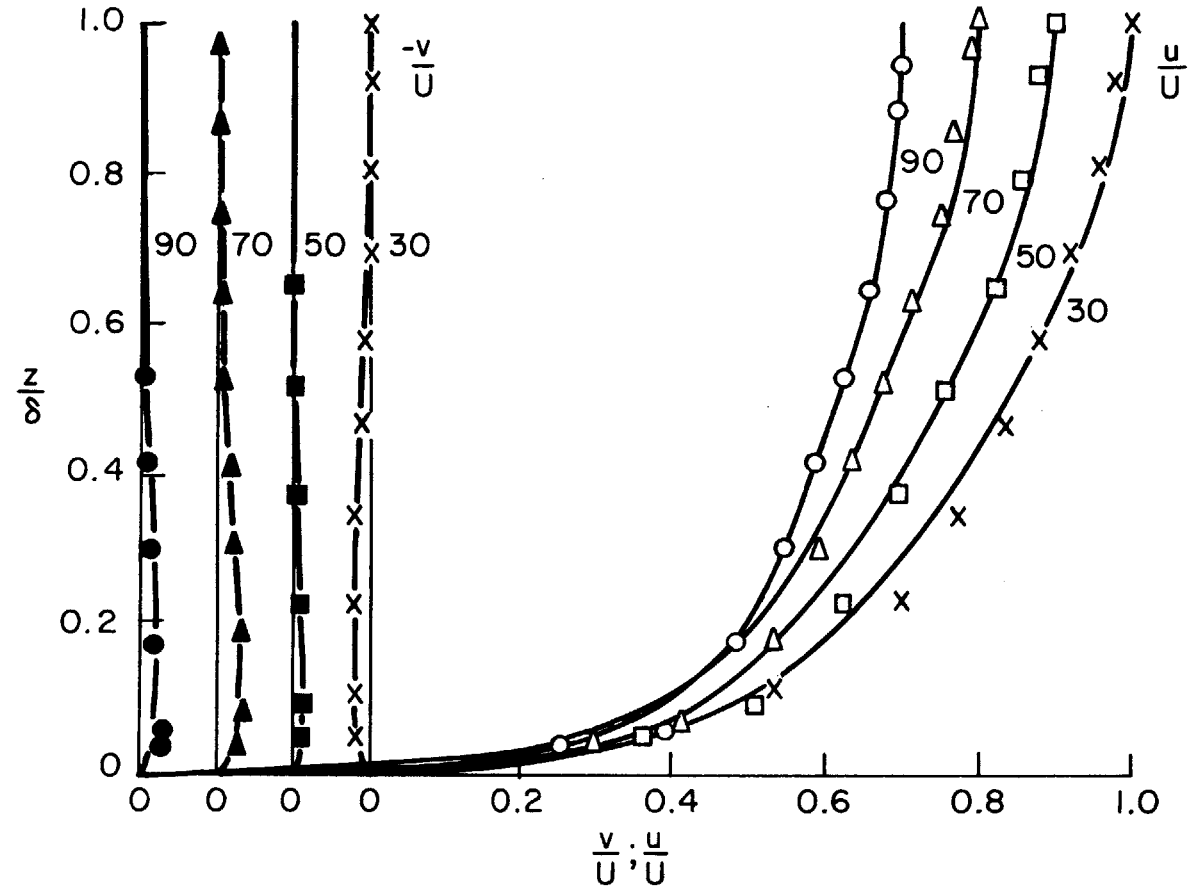

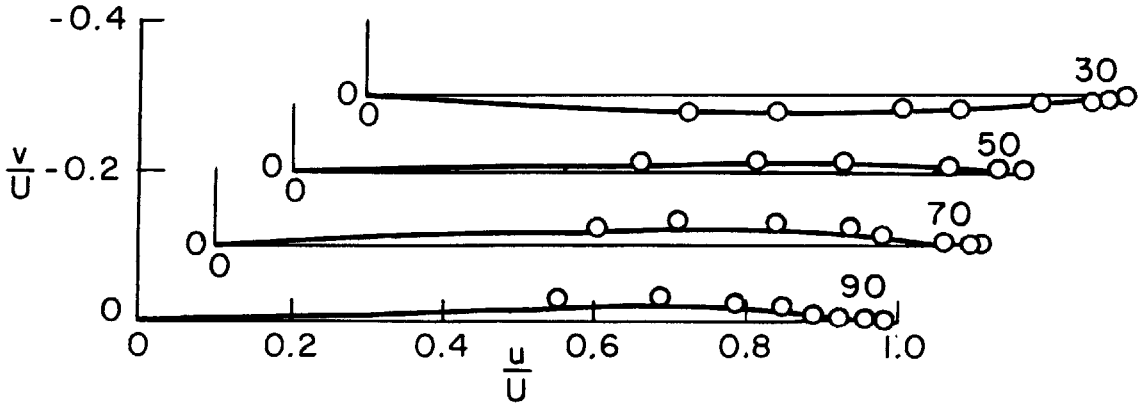

Velocity-Profiles 90% Span Pressure Side

Fig. 19 continued

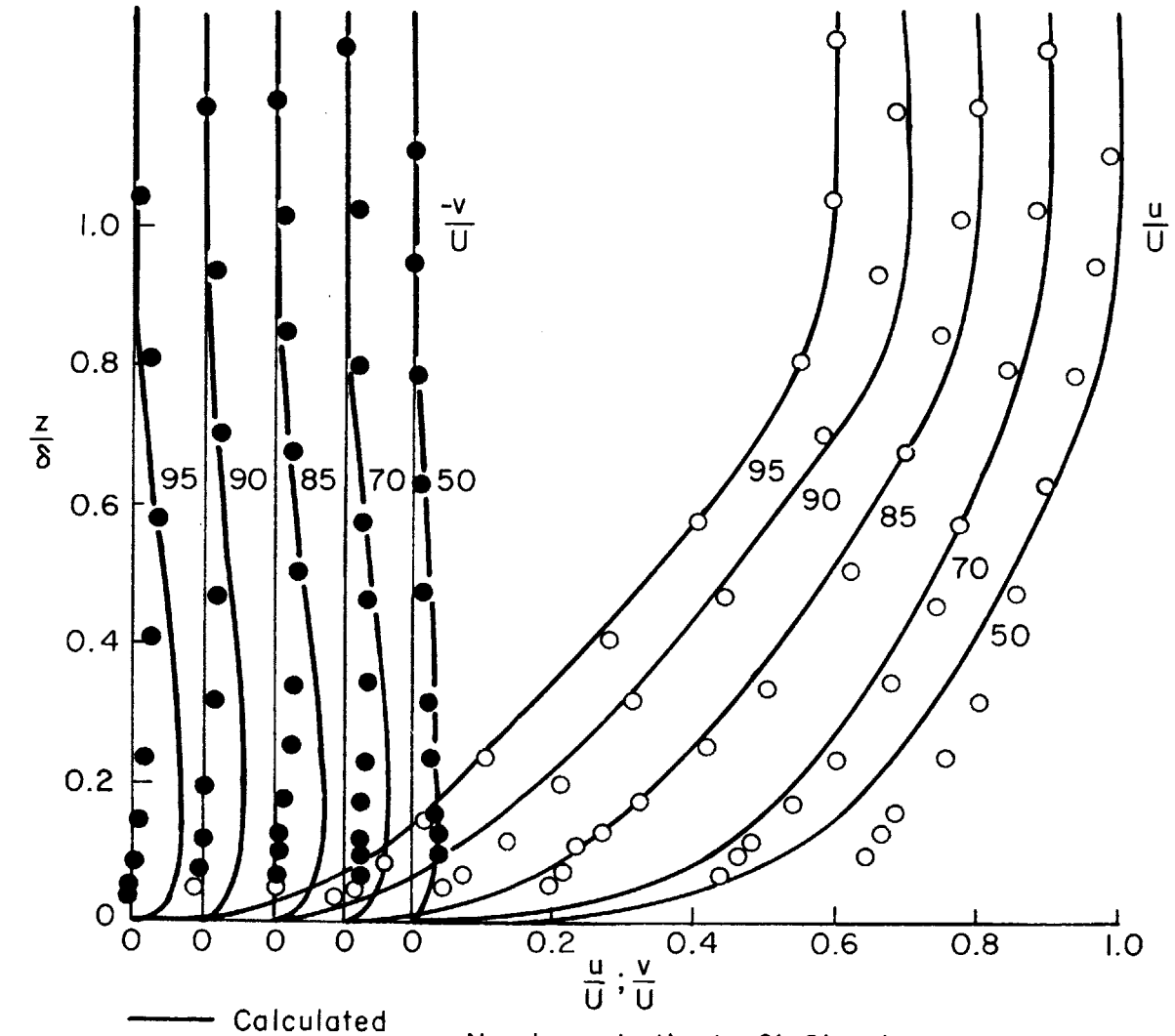

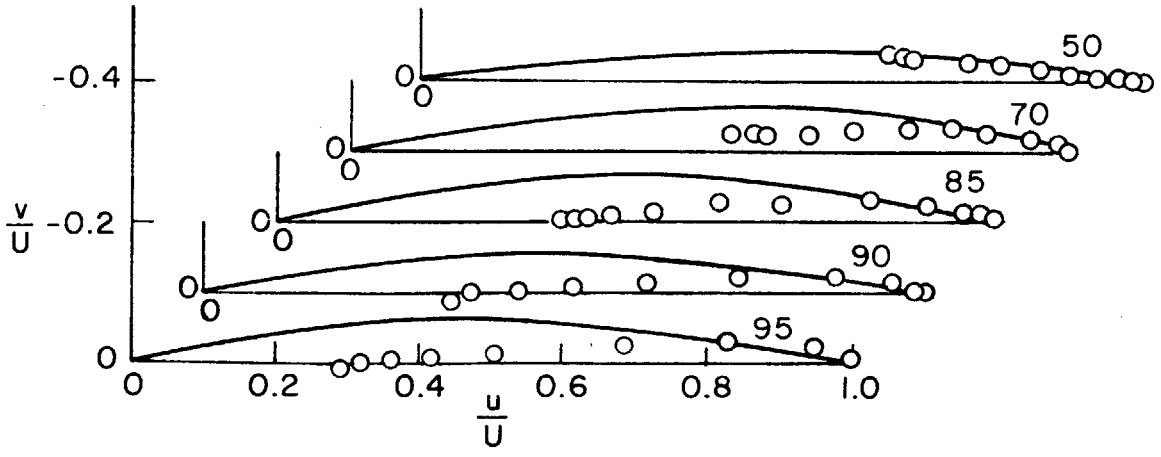

Velocity-Profiles 10% Span Suction Side

Fig. 19 continued

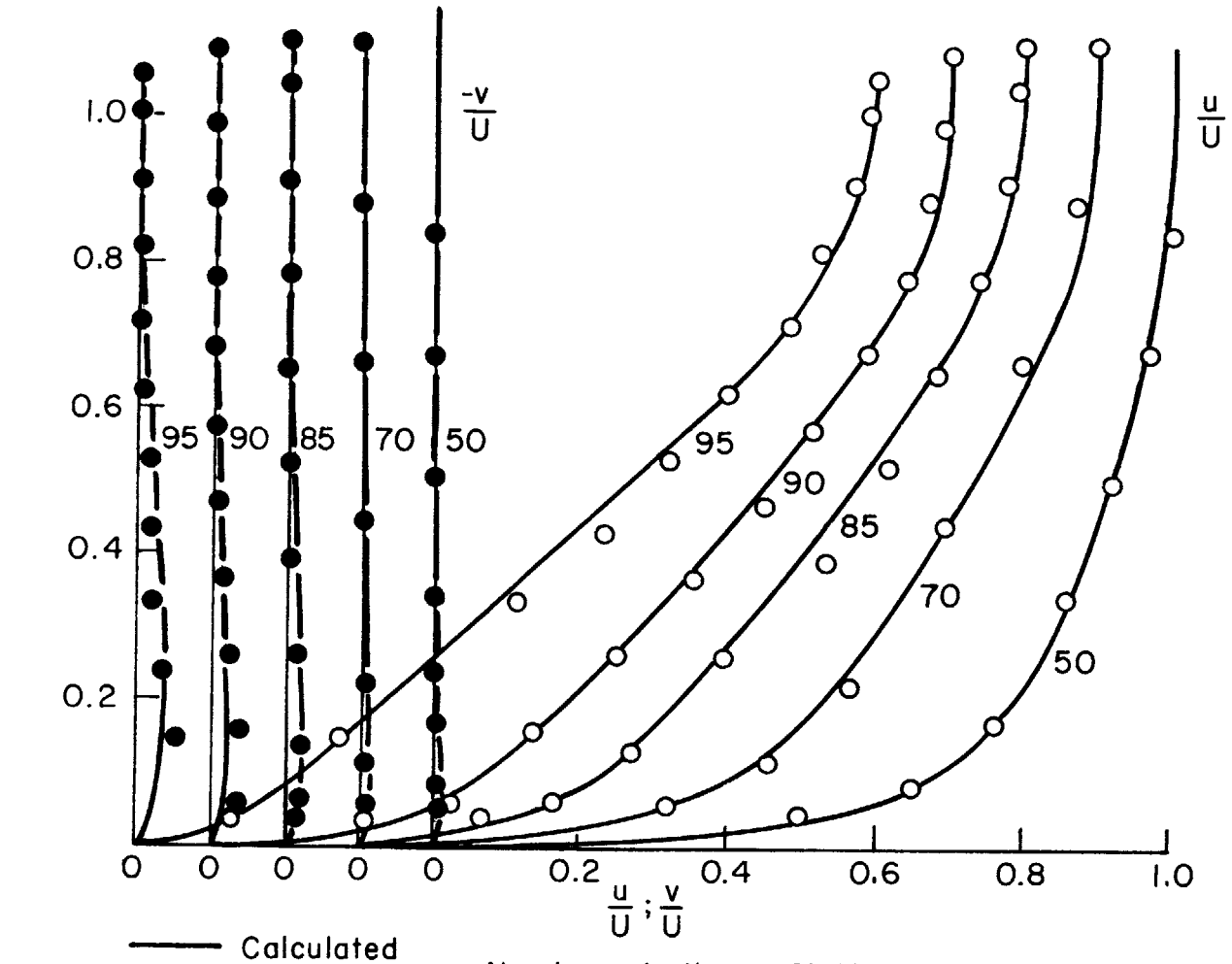

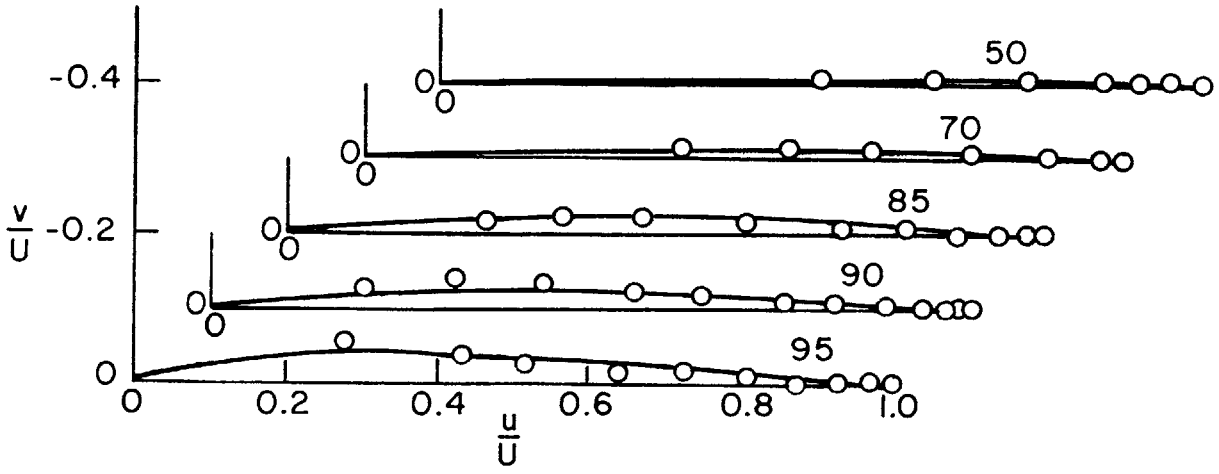

Velocity-Profiles 30% Span Suction Side

Fig. 19 continued

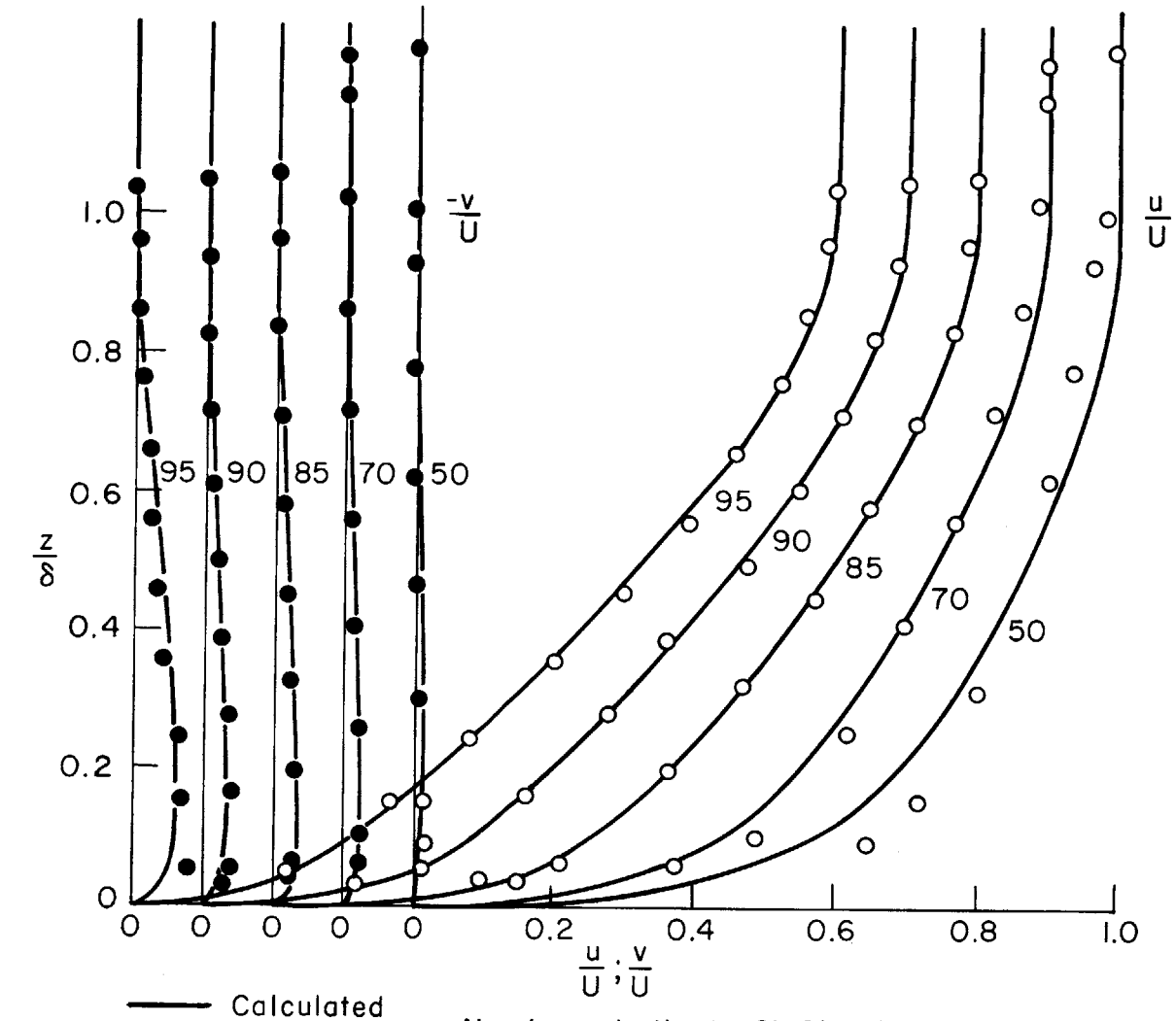

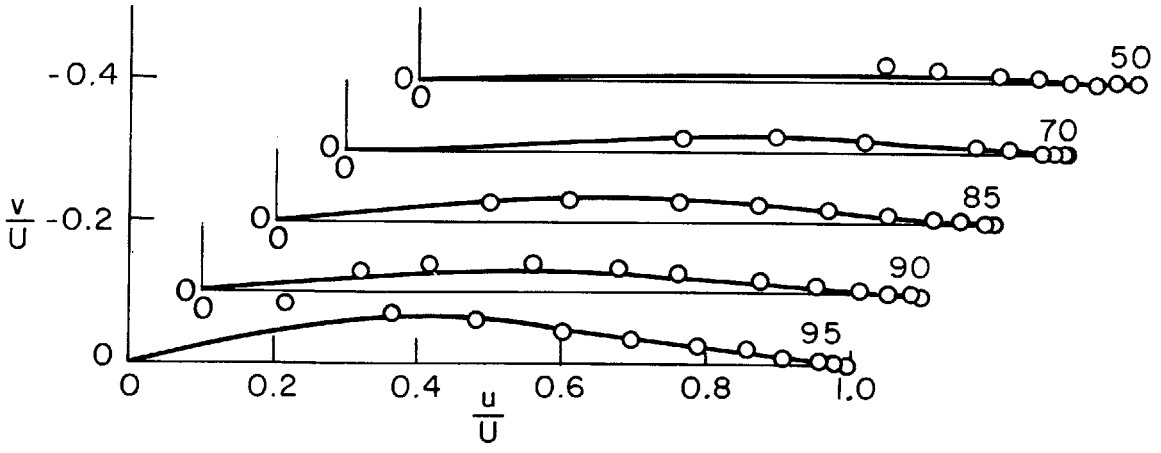

Velocity-Profiles 40% Span Suction Side

Fig. 19 continued

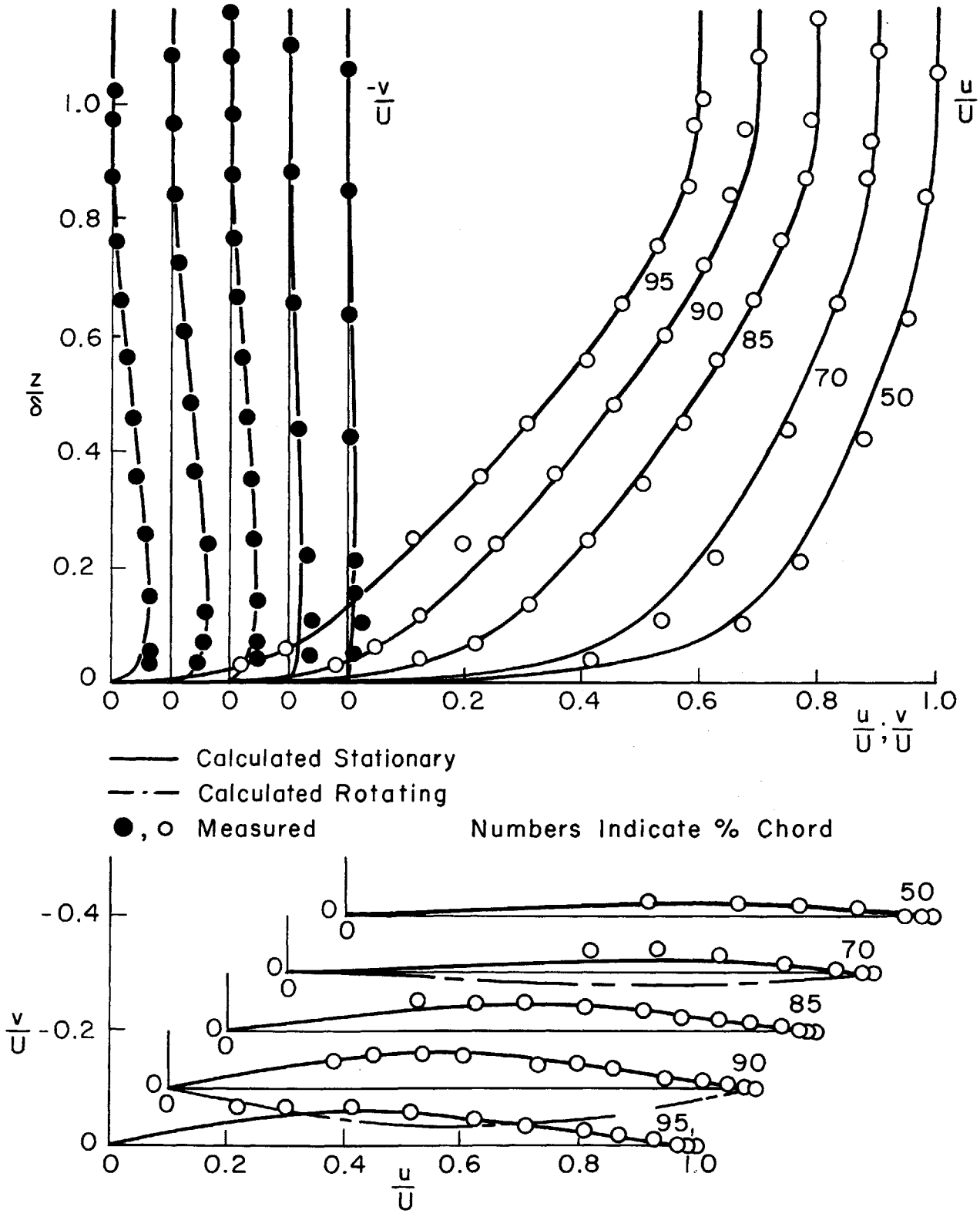

Velocity-Profiles 50% Span Suction Side

Fig. 19 continued

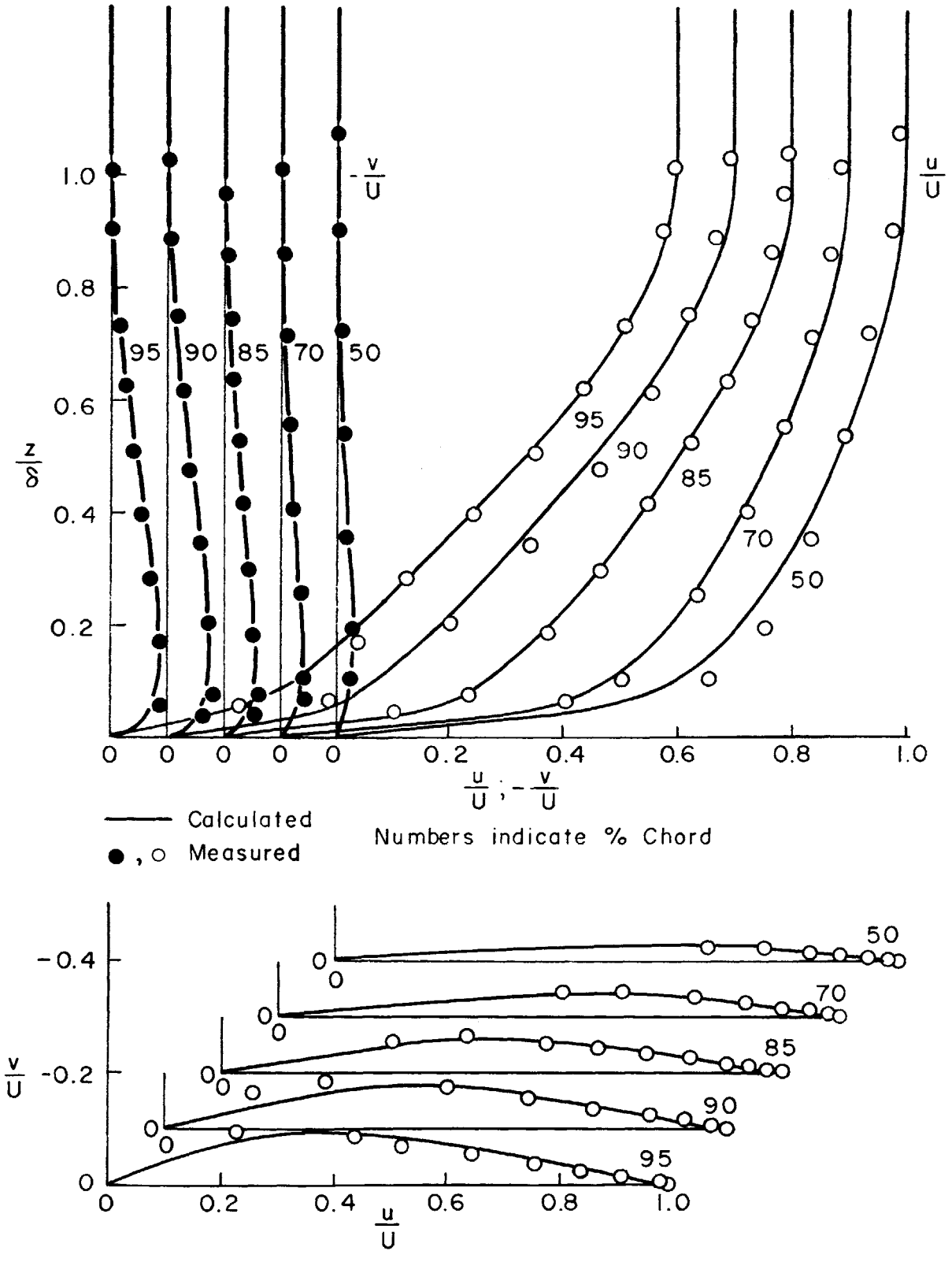

Velocity-Profiles 60% Span Suction Side

Fig. 19 continued

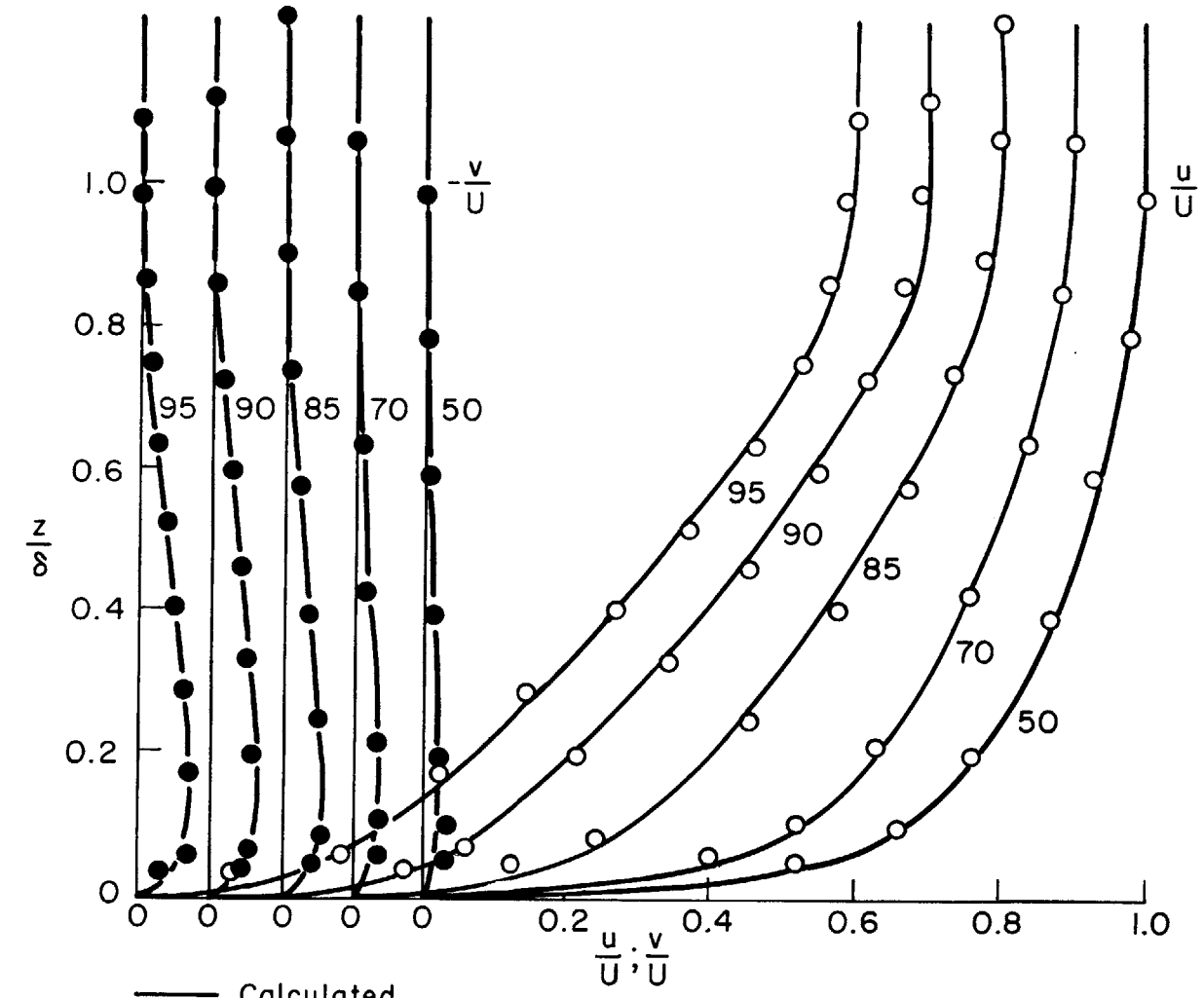

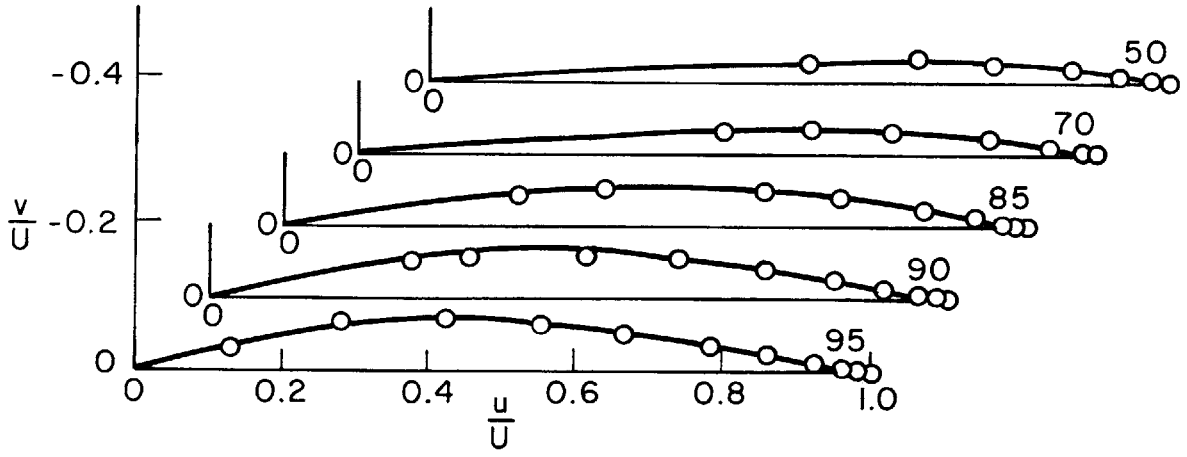

Velocity-Profiles 70% Span Suction Side

Fig. 19 continued

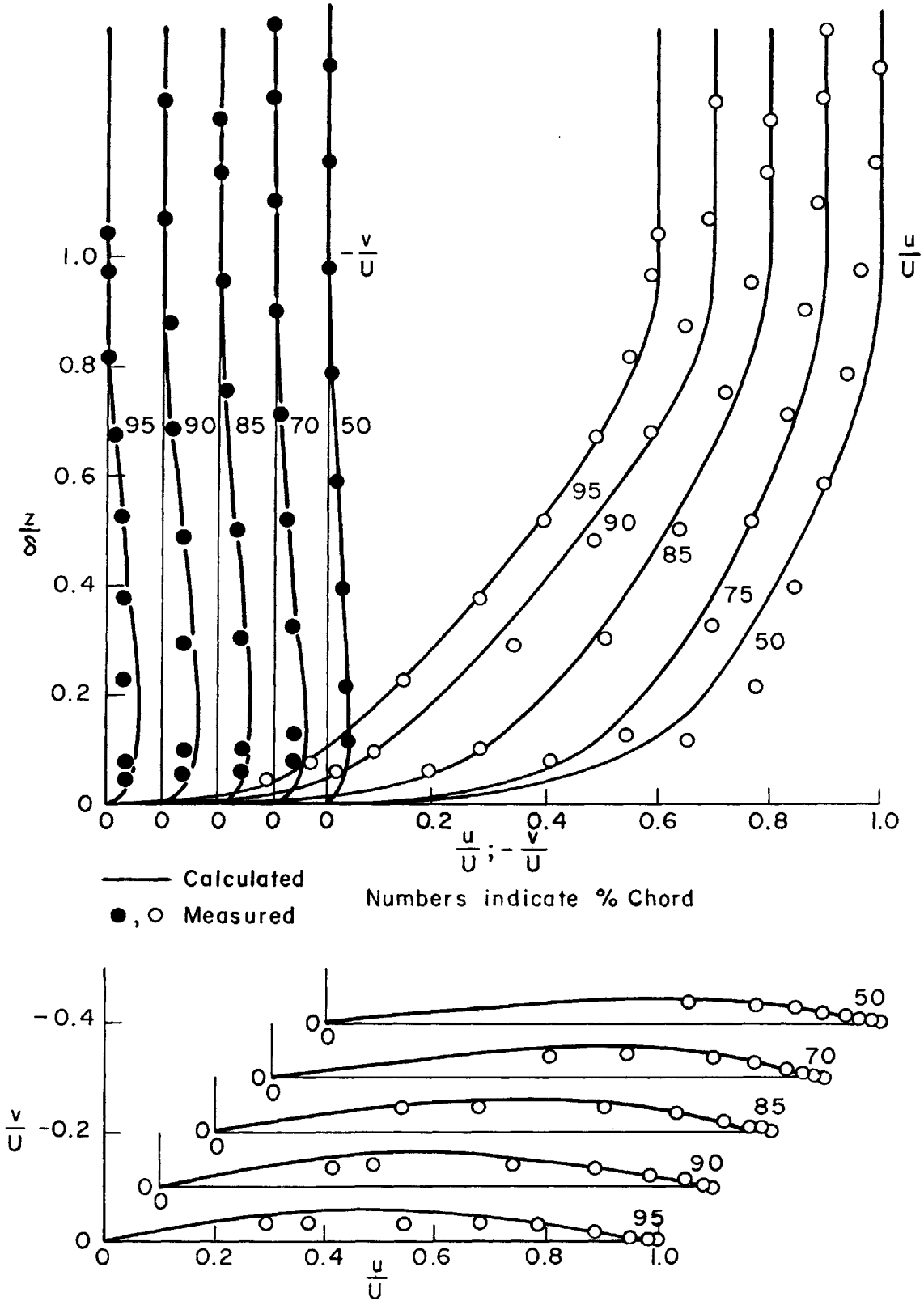

Velocity-Profiles 90% Span Suction Side

Fig. 19 continued

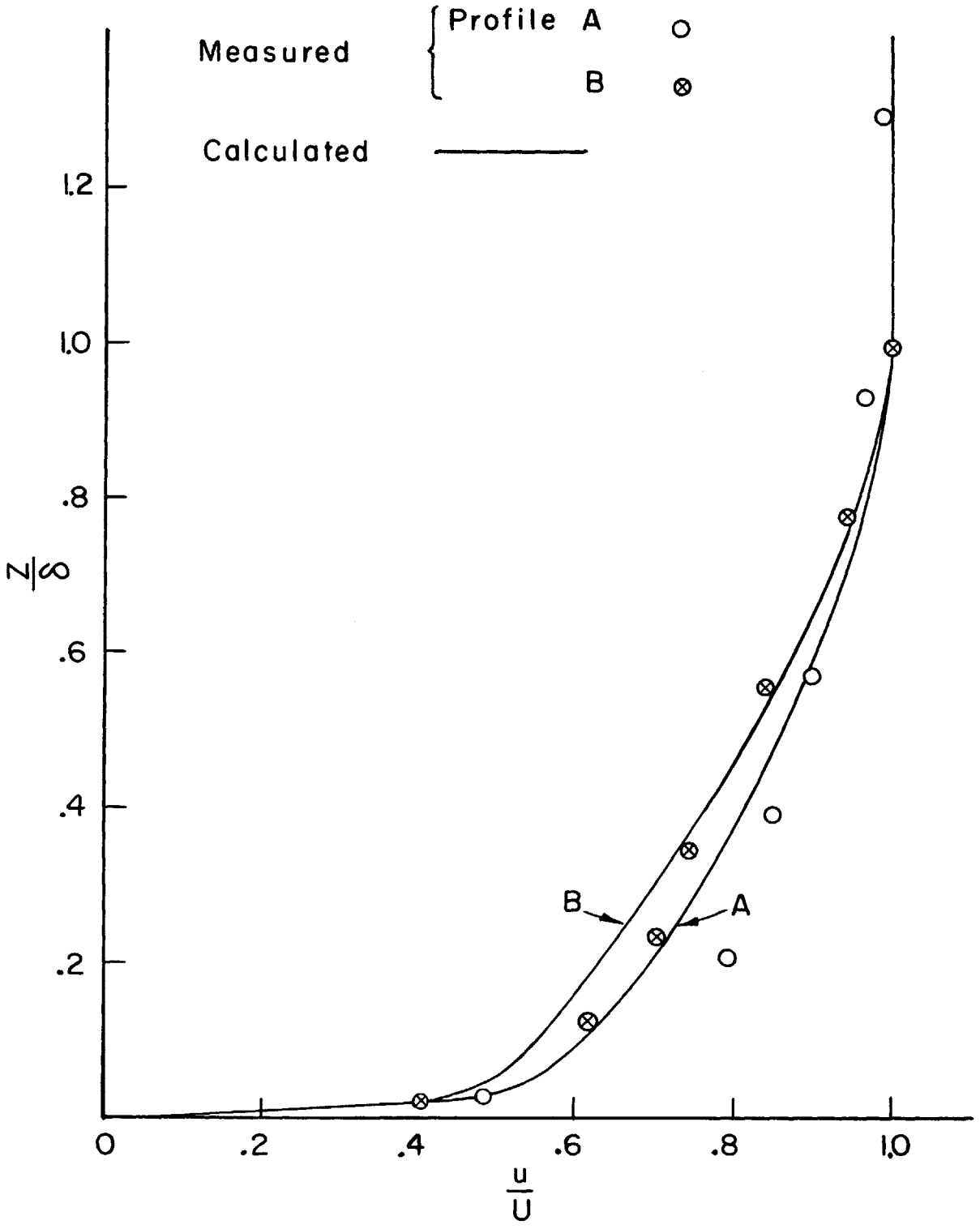

Velocity Profiles in Rotating Duct

Fig. 20

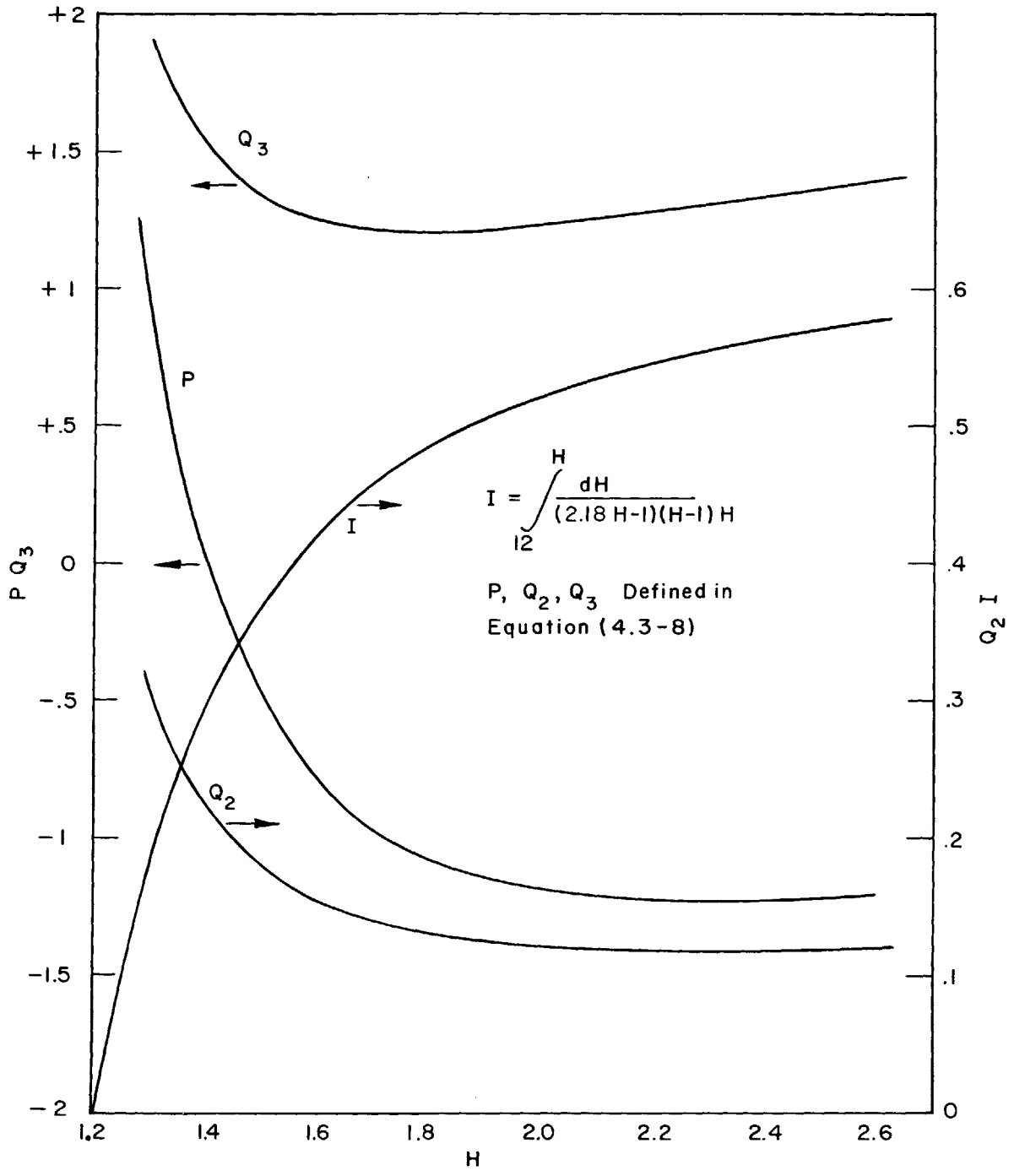

Fig. 21 Functions I, P, Q_2 and Q_3

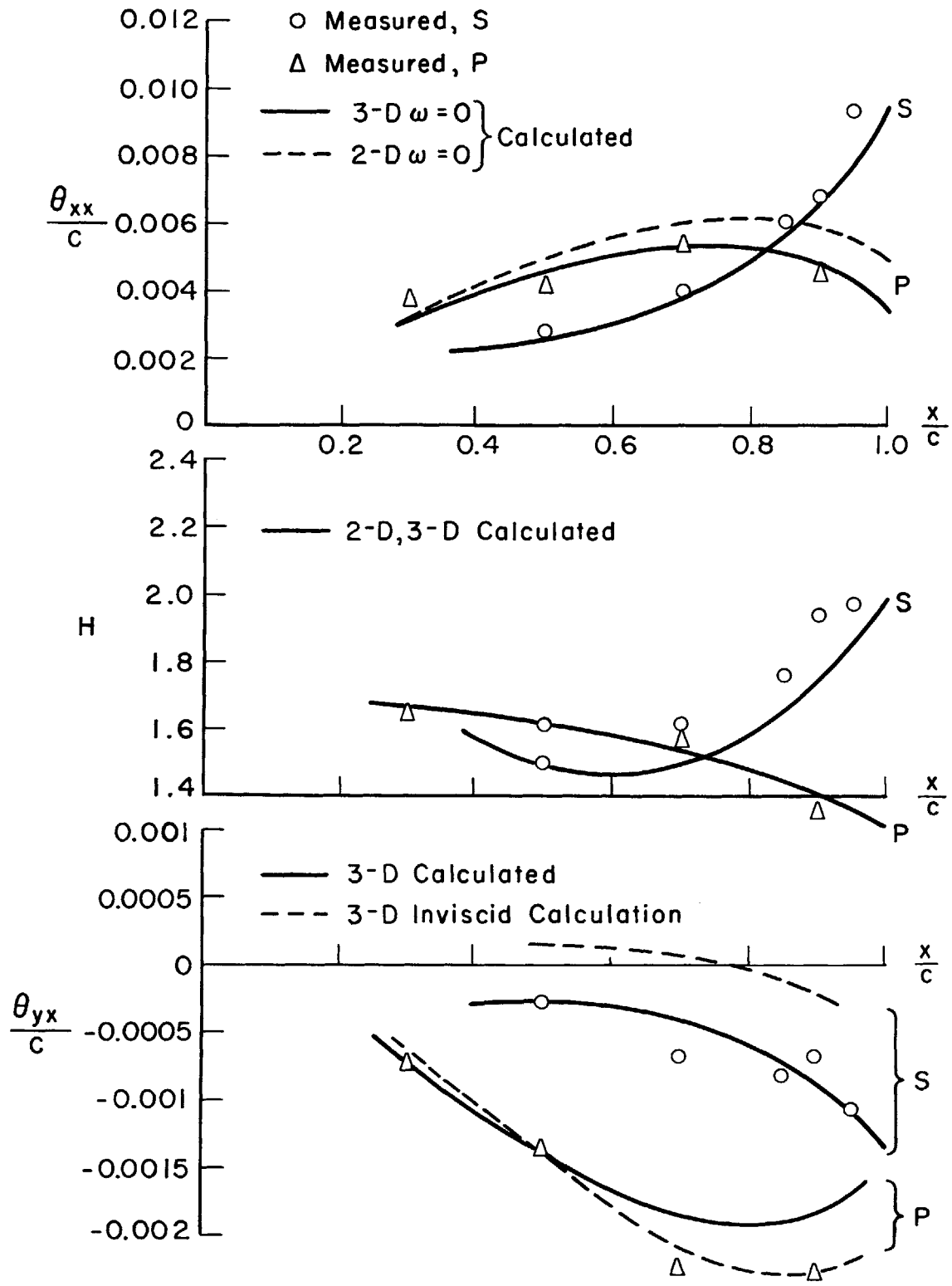

Comparison of Calculated and Measured Quantities 10% Span

Fig. 22

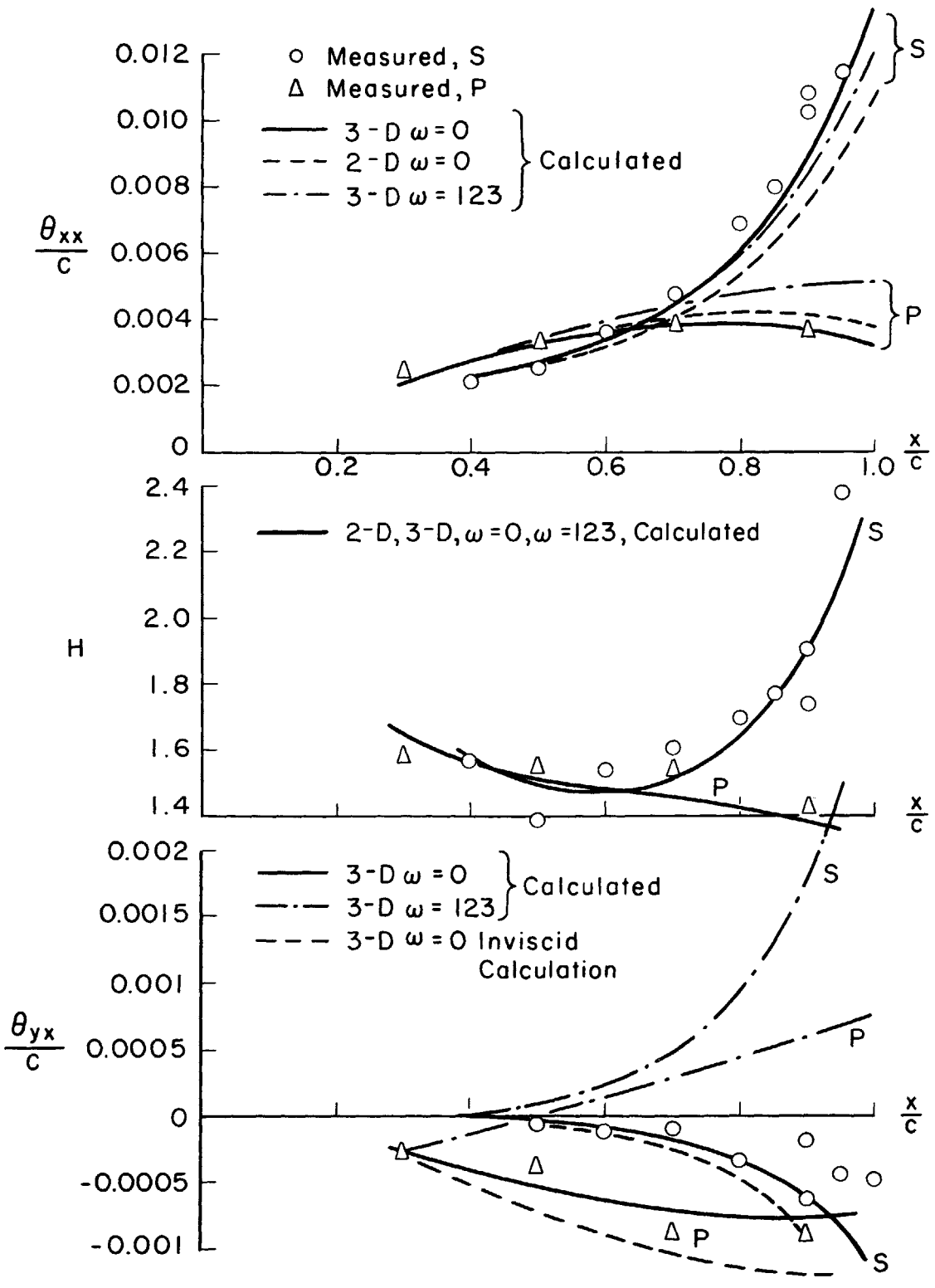

Comparison of Calculated and Measured Quantities 30% Span

Fig. 22 continued

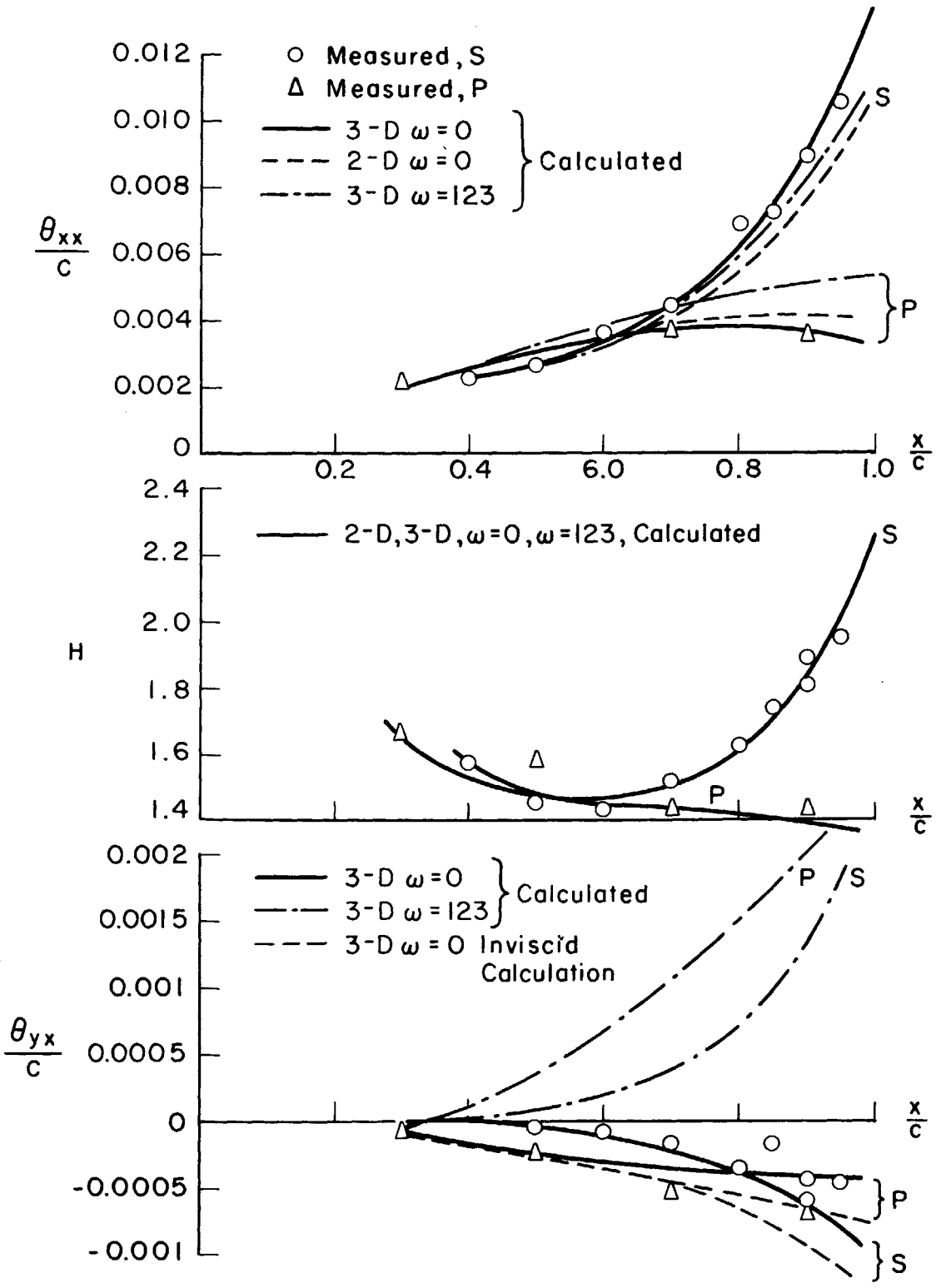

Comparison of Calculated and Measured Quantities 50% Span

Fig. 22 continued

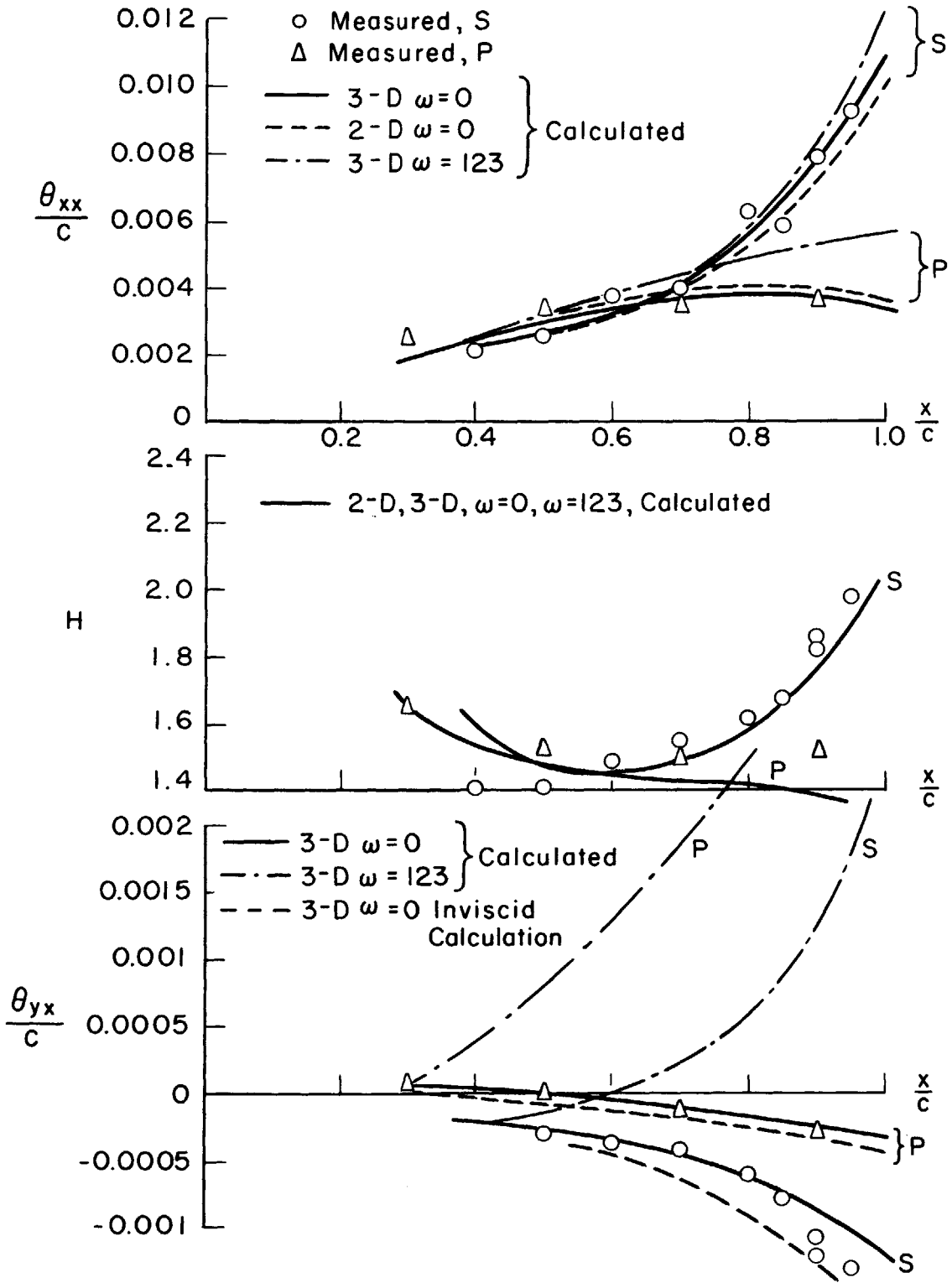

Comparison of Calculated and Measured Quantities 70% Span

Fig. 22 continued

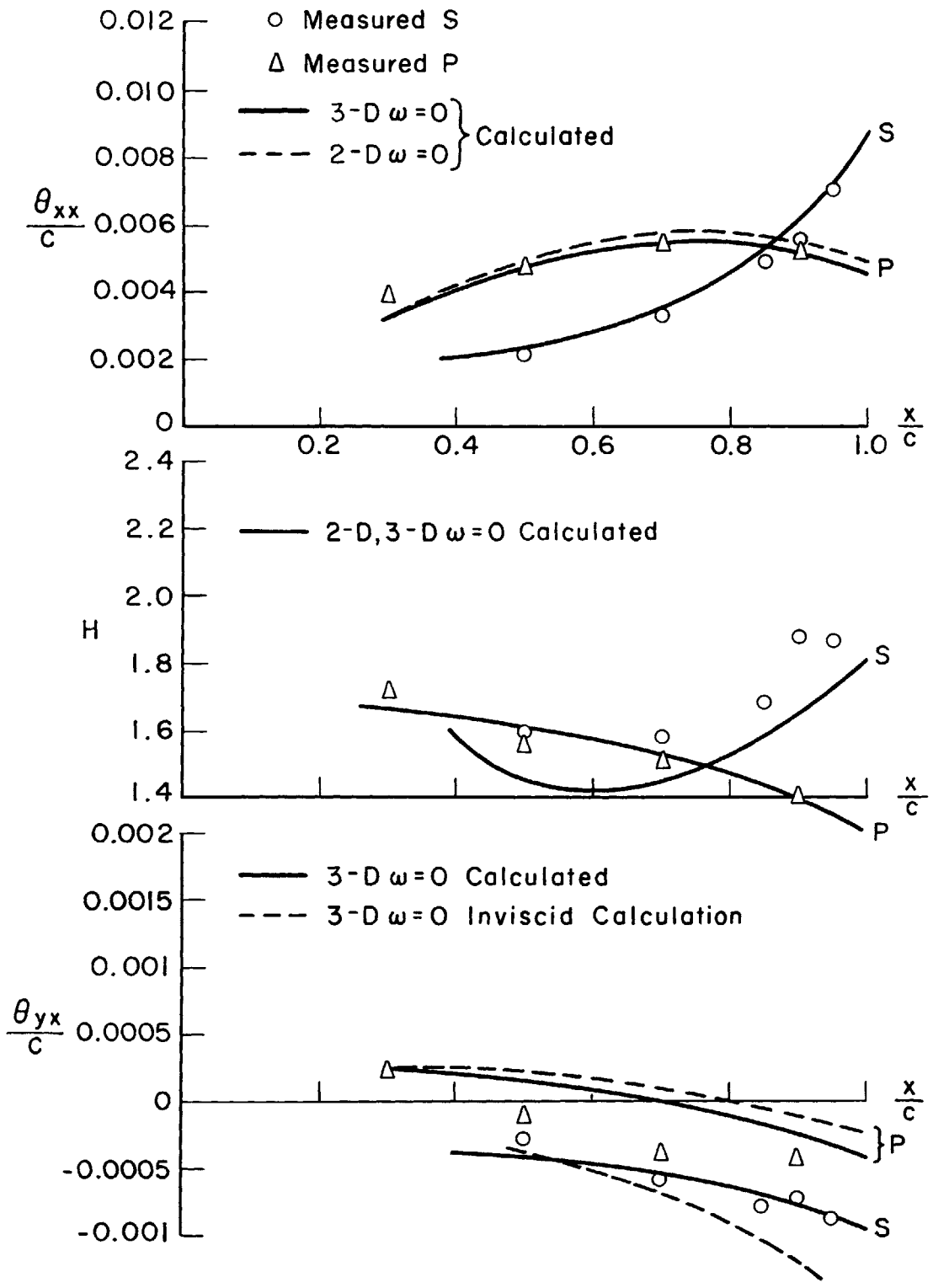

Comparison of Calculated and Measured Quantities 90% Span

Fig. 22 continued

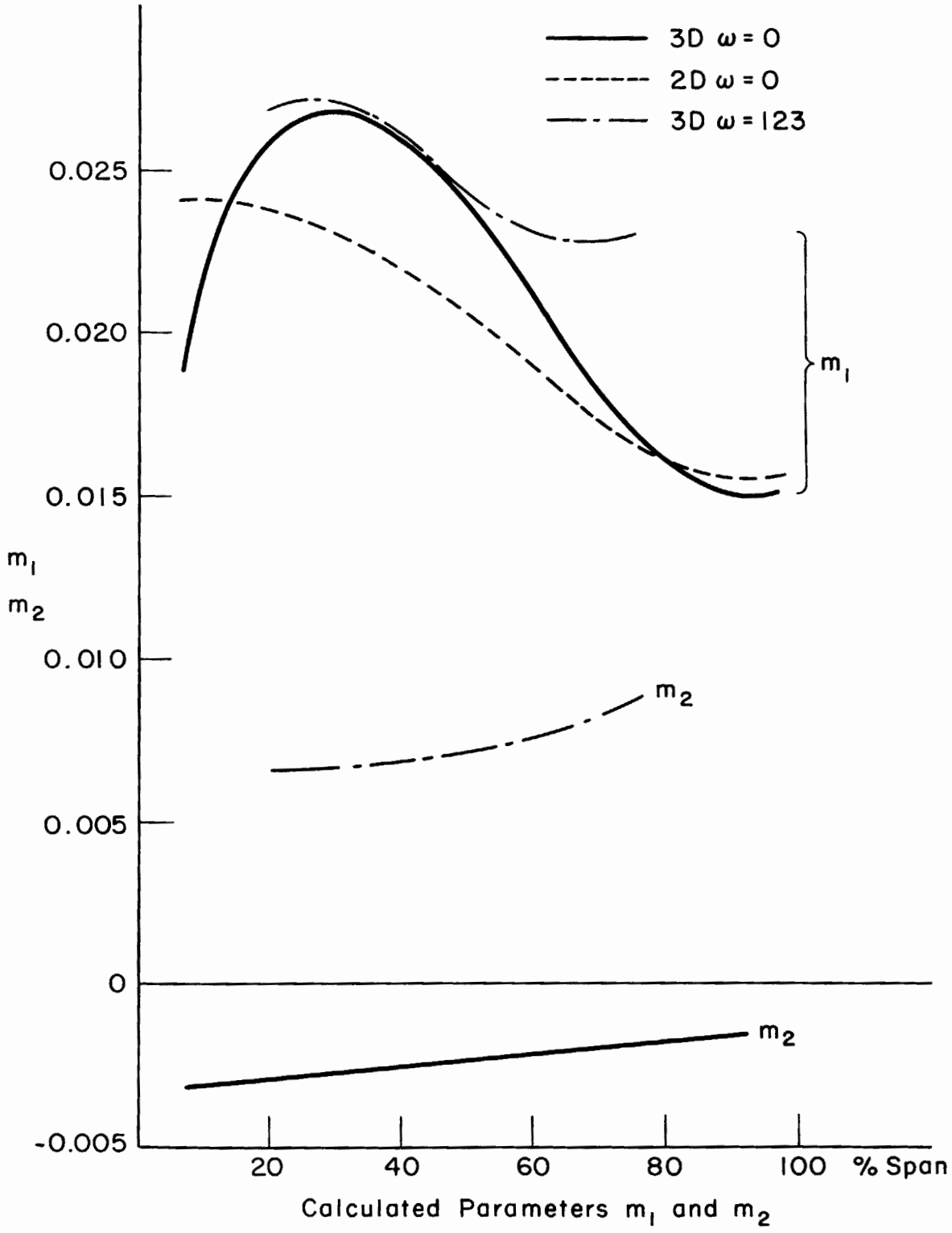
3D ω = 0
2D ω = 0
3D ω = 123
0.025
0.020
0.015
0.010
0.005
0
-0.005
m1
m2
m1
m2
m2
20
40
60
80
100
% Span
Calculated Parameters m1 and m2

Fig. 23

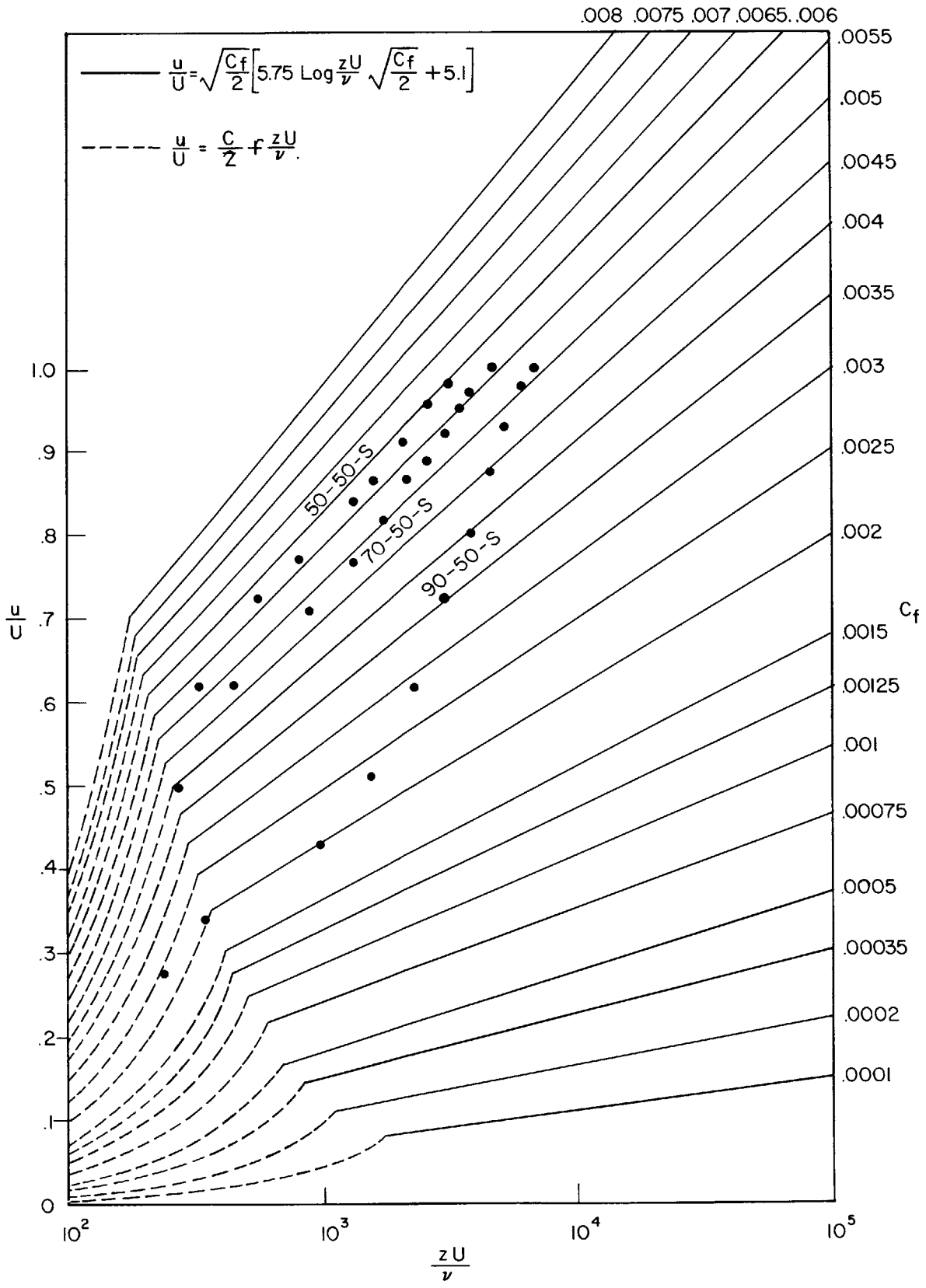

Fig. 24 "Law of the wall" plot

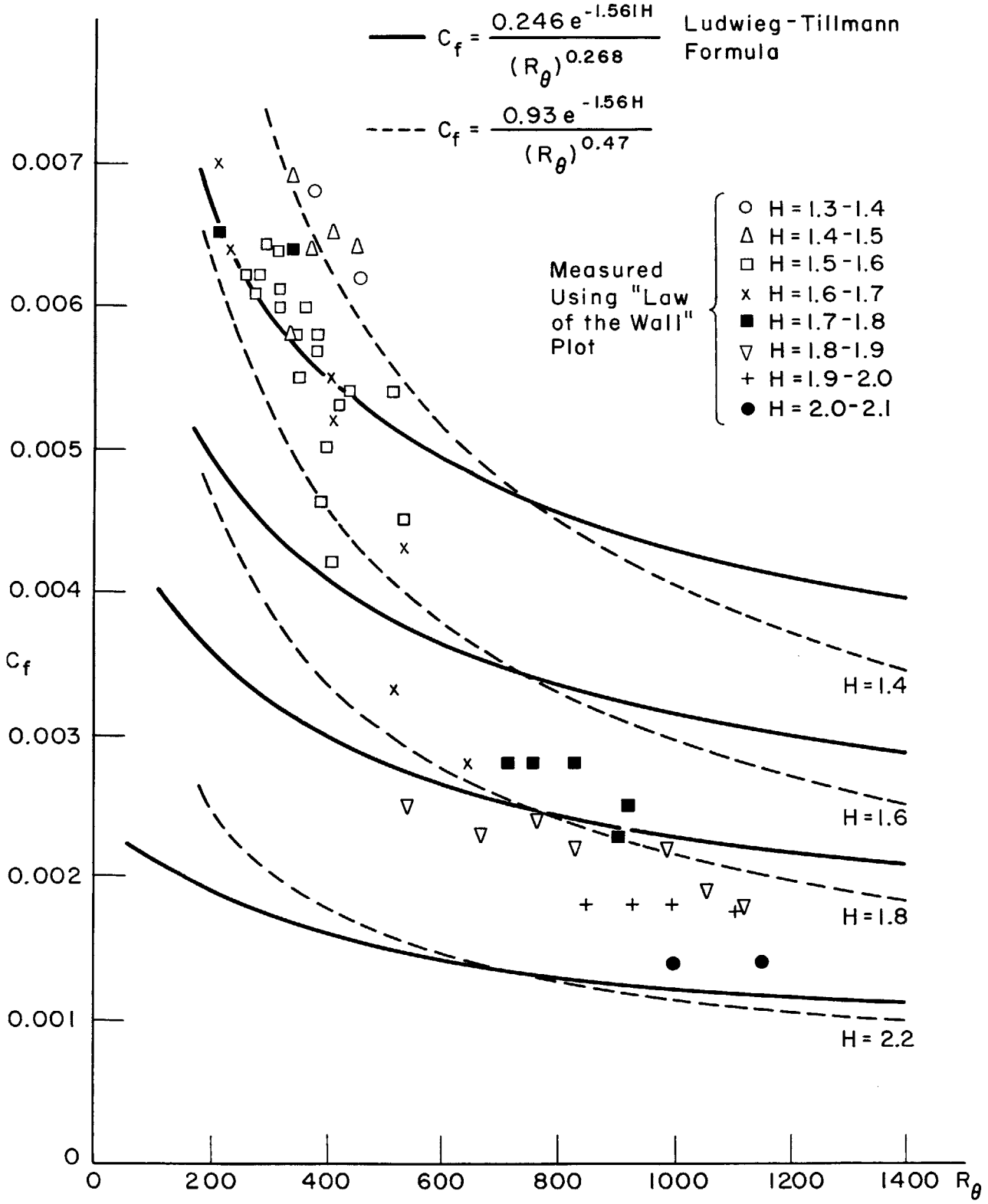

Comparison of Calculated and Measured Skin-Friction Coefficient

Fig. 25

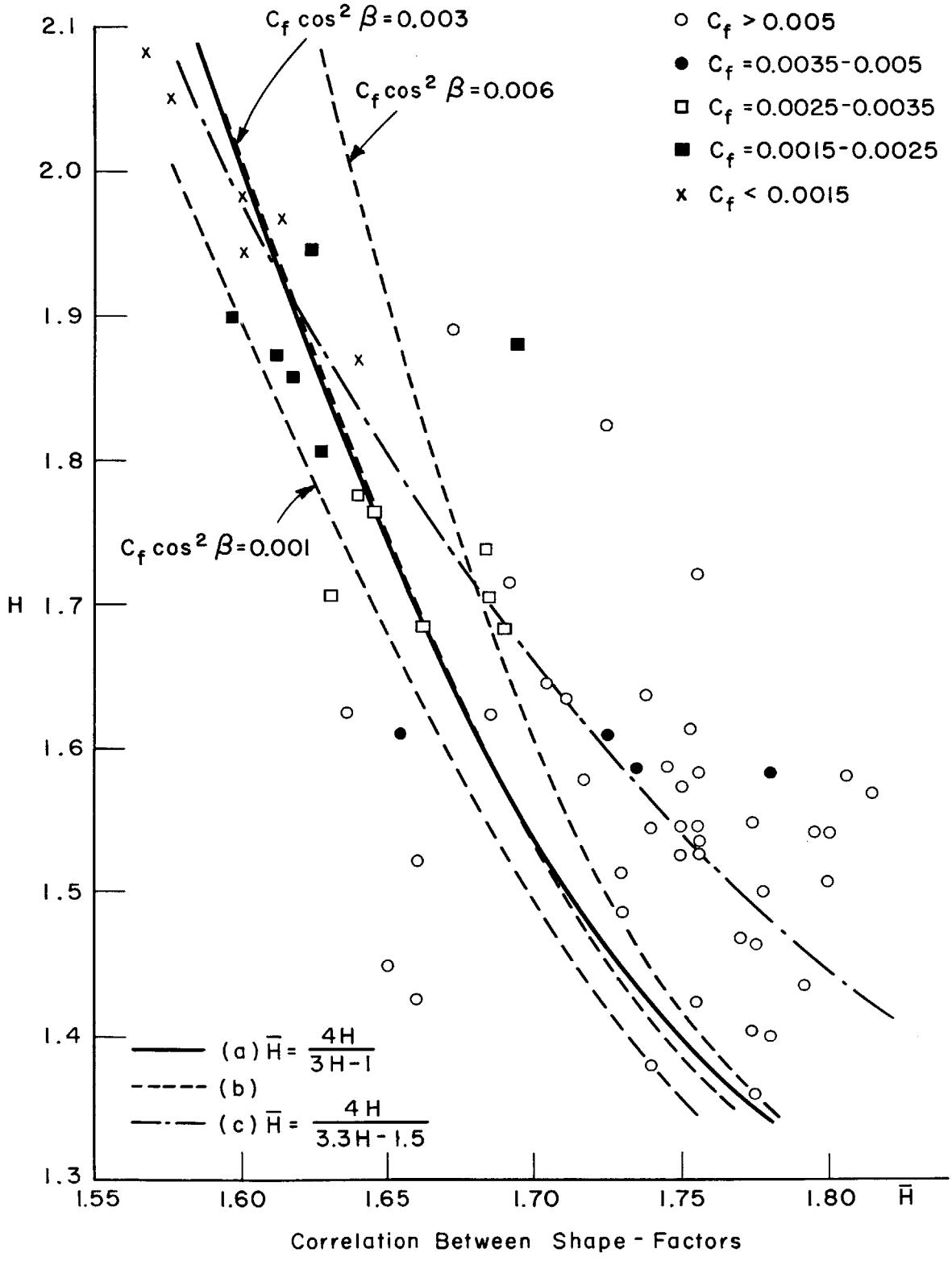
$C_f \cos^2 \beta = 0.003$
$C_f \cos^2 \beta = 0.006$
$C_f \cos^2 \beta = 0.001$
$C_f > 0.005$
$C_f = 0.0035 - 0.005$
$C_f = 0.0025 - 0.0035$
$C_f = 0.0015 - 0.0025$
$C_f < 0.0015$
(a) $\bar{H} = \frac{4H}{3H-1}$
(b)
(c) $\bar{H} = \frac{4H}{3.3H-1.5}$
H
$\bar{H}$
2.1
2.0
1.9
1.8
1.7
1.6
1.5
1.4
1.3
1.55
1.60
1.65
1.70
1.75
1.80
Correlation Between Shape - Factors

Fig. 26